



UNIVERSITÀ DEGLI STUDI ROMA TRE

Department of Mathematics and Physics
Doctoral Program in Physics - XXXIV Cycle

A thesis submitted for the degree of
Doctor of Philosophy in Physics

Imaging oceanic basins with radiative transfer and wave equation models

Supervisors:
Prof. **Elisabetta Mattei**
Prof. **Fabio Cammarano**

Author:
Chiara Nardoni

Co-Supervisor:
Prof. **Luca De Siena**

January 2022

*There is a tide in the affairs of men,
Which, taken at the flood, leads on to fortune;
Omitted, all the voyage of their life
Is bound in shallows and in miseries.
On such a full sea are we now afloat;
And we must take the current when it serves,
Or lose our ventures.*

Julius Caesar, William Shakespeare

Abstract

Coda wave attenuation tomography images efficiently highly-heterogeneous regions such as volcanic areas or areas characterized by fluid/melts and temperature gradients. However, as the large-scale structure variations hinder the separation of stochastic effects from complex coherent propagation, imaging heterogeneities across oceanic basins with this method at the regional scale and for low frequencies presents challenges. This thesis focuses on the physics behind stochastic and coherent wave propagation in mixed continental-oceanic settings, benchmarking results with a combination of radiative-transfer and wave-equation forward modelling approaches and codes, and inversion tools specifically designed for coda-attenuation imaging.

Coda-wave attenuation imaging is applied across Italy and the Tyrrhenian basin, a mixed continental-oceanic crust, in the frequency band 0.5-1.5Hz using regional seismograms and diffusive sensitivity kernels. The attenuation maps show the sensitivity of the late-time coda waves to the shallow oceanic Moho discontinuity that produces coherent reverberations. They suggest the potential of regional-scale data to provide higher resolution maps of Moho, velocity variations and heterogeneities than what is currently available.

The radiative transfer and wave-equation forward modelling evaluate the effects of sharp structural variations on wave propagation. Radiative-transfer-based simulations allow exploring the response of seismic wavefield to structural and heterogeneity spectrum variations by combining ray and scattering theories. The provided modelling of both the coherent and the stochastic wavefields is able to constrain both heterogeneity spectrum and crustal interfaces across the Tyrrhenian basin. The seismic scattering mechanism turns out to be predominantly resonant in the ~ 1 Hz frequency band. As a consequence, crustal reverberations are the dominant physical mechanism generating coda: these waves can propagate and reverberate in the crustal waveguides induced by sharp changes in continental and oceanic crust.

The full-waveform modelling based on the finite difference method improves the Radiative Transfer forward model by exploring the full 3D propagation, including realistic topography, bathymetry and laterally-varying interfaces. The wavefield simulation in different crustal models highlights the presence of a crustal waveguide with a later-

ally varying thickness in the Southern Tyrrhenian basin. Synthetic tests were performed by correlating the recorded data with wavefield simulations in crustal models with and without a crustal pinch. This quantitative comparison discriminates the phases arrival and amplitude influenced primarily by the continental Moho and the thin waveguide across oceans.

The combined results of imaging and radiative transfer results with wave equation forward modelling across the Southern Tyrrhenian Sea show that regional waveforms from a single earthquake can be fully exploited thus resolving Moho depths and variations in sediment thickness across the basin. The joint radiative transfer and wave equation approach is ideally suited to become the benchmark forward-modelling approach for full-waveform inversions in oceanic settings and regions of crustal reverberations.

Acknowledgements

At the end of this chapter, I would like to express my endless gratitude to the people who stood by me.

I am very grateful to my supervisor Prof. *Elisabetta Mattei* for always supporting and encouraging me before and during the PhD. She has been and will be much more than just a professor for me. I sincerely thank Prof. *Luca De Siena* for everything he taught me, for his feedback and for helping me to broaden my knowledge. I cannot thank them enough for their constant guidance and for helping me become a better researcher and person.

I also thank Prof Fabio Cammarano and Fabrizio for their feedback and important suggestions.

A special thanks also goes to Barbara, Sebastian and Prof. Elena Pettinelli for always being there to help and teach me at all times since I met them.

I would like to thank Prof. Cormier, Prof. Maeda and Dr Sanborn for developing the open-access codes and for giving me suggestions in the implementation of the modelling presented in this thesis.

This journey would not have been the same without my colleagues of the 'Aquarium'. We have shared the joys and difficulties of this work and learnt the beauty of walking together. We are not only colleagues but also friends. I wish them the best in research and life. Thanks, also, to my colleague and friend Ina for the best video calls ever and for encouraging me to explore the world.

Thanks to Simona for being a fantastic colleague and friend. I'm grateful to share with her everything that happens, not only at work. Thanks for her support and for the best time spent together.

I am very grateful to my friends, Luisa, Lucia, Camilla, Elena, Lorenzo and Daniele. They are part of my family. They have always been by my side, understanding me even without speaking. I would like to thanks to them for making everything and every moment better with just a smile.

Finally, I would like to express my deepest gratitude to my parents and brother for their incomparable love, help and support in the most challenging and joyful times. I thank them for always encouraging me to explore and seek my way.

Publications and proceedings

Nardoni C., De Siena L., Cammarano F., Magrini F., Mattei E., Sensitivity of the full-wavefield to crust-mantle discontinuity variations - *In preparation*

Nardoni C., De Siena L., Cammarano F., Magrini F., Mattei E., Modelling seismic wavefield across the Tyrrhenian basin, selected for publication in *Il Nuovo Cimento*

Nardoni C., De Siena L., Cammarano F., Magrini F., Mattei E., Modelling regional-scale attenuation across Italy and the Tyrrhenian Sea, *Physics of the Earth and Planetary interior*, 2021

Nardoni C., Cammarano F., De Siena L., Mattei E., Seismic attenuation in the Tyrrhenian Sea: estimation of coda quality factor Q_c , GNGTS Gruppo Nazionale di Geofisica della Terra Solida, Atti del 38° Convegno Nazionale, 2019

Contents

| | |
|---|-----------|
| Introduction | 1 |
| 1 Seismic Wave Attenuation | 4 |
| 1.1 Attenuation Processes | 5 |
| 1.2 Heterogeneity in the lithosphere | 6 |
| 1.3 Imaging by deterministic observations | 7 |
| 1.4 Stochastic approach: Coda Waves | 10 |
| 1.4.1 Coda Attenuation Parameters | 11 |
| 1.4.1.1 Scattering characteristics | 13 |
| 1.4.1.2 Single scattering approximation | 14 |
| 1.4.1.3 Diffusive approximation | 15 |
| 1.5 Q_c^{-1} Measurements | 16 |
| 2 Seismic tomography | 19 |
| 2.1 Inverse problem and regularization | 19 |
| 2.2 Imaging of Q_c spatial variations | 21 |
| 2.3 From rock samples to regional scale | 24 |
| 2.4 MuRAT | 26 |
| 3 Modelling by Radiative Transfer | 29 |
| 3.1 Radiative Transfer Theory (RTT) | 29 |
| 3.2 Mathematical formulation of RTT | 31 |
| 3.3 Random Media | 33 |
| 3.4 Radiative3D | 36 |
| 3.4.1 Deterministic propagation | 37 |
| 3.4.2 Stochastic propagation | 38 |
| 3.4.3 Simulation parameters and set up | 39 |

| | | |
|----------|---|-----------|
| 4 | Seismic attenuation modelling | 41 |
| 4.1 | Introduction to regional scale attenuation | 41 |
| 4.2 | Data and Methods | 44 |
| 4.2.1 | Data selection and processing | 44 |
| 4.2.2 | Coda attenuation measurements | 45 |
| 4.2.2.1 | Q_c Lapse Time Dependence | 46 |
| 4.2.3 | Inversion for coda attenuation | 48 |
| 4.3 | Results | 50 |
| 4.3.1 | Coda-attenuation mapping | 50 |
| 4.3.2 | Modeling with Radiative3D | 53 |
| 4.3.2.1 | Selected earthquakes for comparison | 55 |
| 4.3.2.2 | Parametric study | 55 |
| 4.3.2.3 | Comparison between data and synthetic Q_c^{-1} | 58 |
| 4.4 | Discussion | 61 |
| 4.4.1 | Southern Tyrrhenian basin | 61 |
| 4.4.2 | The Apennines and the Northern Tyrrhenian basin | 65 |
| 4.5 | Concluding remarks | 66 |
| 5 | Wave equation modelling | 68 |
| 5.1 | The seismic wave equation | 68 |
| 5.2 | Seismic anisotropy | 71 |
| 5.3 | Rheology | 72 |
| 5.4 | Source | 76 |
| 5.5 | Numerical methods | 79 |
| 5.5.1 | Finite Differences | 80 |
| 5.5.2 | Continuity condition across interfaces | 82 |
| 6 | OpenSWPC | 84 |
| 6.1 | Wave equation and viscoelastic model | 84 |
| 6.2 | Staggered-grid and stability conditions | 87 |
| 6.3 | Boundary condition | 90 |
| 6.4 | Source implementation | 91 |
| 6.5 | Velocity model and small-scale random inhomogeneity | 93 |

| | |
|---|------------|
| 7 Earthquake characteristics and structural properties | |
| from full seismic wave simulations | 94 |
| 7.1 Methods for retrieving Moho depth | 97 |
| 7.2 Simulation Method | 99 |
| 7.2.1 Set up | 100 |
| 7.2.2 Source Implementation and Starting Models | 101 |
| 7.2.3 Starting velocity and sediments models | 104 |
| 7.3 Results | 104 |
| 7.3.1 Sensitivity of the coda to sediments and adjustment of rise-time variations | 106 |
| 7.3.2 Sensitivity to the Moho | 109 |
| 7.3.3 Comparison between flat and realistic interfaces: topography and correlation analysis. | 113 |
| 7.4 Discussion | 116 |
| 7.5 Concluding remarks | 121 |
| Conclusions | 123 |

List of Figures

| | | |
|------|---|----|
| 1.1 | Seismograms from INGV stations | 6 |
| 1.2 | Crust of Southern Apennines (Italy) from seismic refraction study | 9 |
| 1.3 | Moho depth from receiver function | 10 |
| 1.4 | Random heterogeneities | 12 |
| 1.5 | Scattering cross-section | 14 |
| 1.6 | Vertical component seismogram | 17 |
| 2.1 | Example of Checkerboard Test | 22 |
| 2.2 | Sensitivity kernels | 25 |
| 2.3 | 3D weighting function | 25 |
| 2.4 | Coda attenuation tomography Central Italy | 27 |
| 3.1 | Multiple scattering | 33 |
| 3.2 | Heterogeneities spectrum | 35 |
| 3.3 | Radiative3D phonon's trajectory | 37 |
| 3.4 | Implemented energy propagation | 39 |
| 3.5 | Examples of crustal models | 40 |
| 4.1 | Data coverage | 45 |
| 4.2 | Seismogram spectrum | 46 |
| 4.3 | Filtered Seismogram and envelope showing Q_c^{-1} linear regression | 47 |
| 4.4 | Lapse-time dependence of Q_c | 48 |
| 4.5 | Comparison between computational and analytic kernels | 49 |
| 4.6 | L-curve | 50 |
| 4.7 | Checkerboard test | 51 |
| 4.8 | Computational kernels | 52 |
| 4.9 | Q_c^{-1} imaging using analytic kernels | 53 |
| 4.10 | Focal mechanisms of the earthquakes modelled via Radiative3D | 55 |

| | | |
|------|---|-----|
| 4.11 | Envelope modelling: thinner crust | 57 |
| 4.12 | Envelope modelling: thinner crust - event B | 58 |
| 4.13 | Envelope modelling: thicker crust | 59 |
| 4.14 | Envelope for low and high scattering | 60 |
| 4.15 | ε and a trade-off | 60 |
| 4.16 | Q_c estimated from synthetic traces | 61 |
| 4.17 | Synthetic envelopes | 62 |
| 4.18 | Q_c estimated in three coda time windows on the synthetic envelopes | 62 |
| | | |
| 5.1 | Elastic and viscous mechanical behaviour | 74 |
| 5.2 | Maxwell and Kelvin-Voigt body | 75 |
| 5.3 | Standard Linear Solid | 76 |
| 5.4 | Double-coupe forces | 77 |
| 5.5 | Shear dislocation in spherical coordinates | 79 |
| 5.6 | Grid staggering | 82 |
| 5.7 | Continuity condition | 83 |
| | | |
| 6.1 | Generalized Zener body | 86 |
| 6.2 | Staggered grid layout in 3D space. | 90 |
| | | |
| 7.1 | Simulation grid covering the Southern Tyrrhenian basin and the Italian peninsula | 101 |
| 7.2 | Boxcar and triangle moment rate functions used to describe the seismic source and to compare the synthetic wavefields. | 104 |
| 7.3 | Results obtained varying the focal depth | 105 |
| 7.4 | Results obtained varying the strike, dip and rake | 106 |
| 7.5 | Rise time variation of a boxcar MRF. | 107 |
| 7.6 | Rise time variation of a triangle MRF. | 108 |
| 7.7 | Velocity Model 1.3 - Sediments thickness | 110 |
| 7.8 | Velocity models comparison for wavefield modelling | 111 |
| 7.9 | Sediments thickness and quality factor variations | 112 |
| 7.10 | Rise times comparison using velocity model 1.3 | 113 |
| 7.11 | Crustal sections | 114 |
| 7.12 | Synthetic waveforms obtained using MohoEP18 Model. Comparison between the synthetic seismograms obtained for a crustal model with/without the pinch and the recordings. | 115 |

| | |
|--|-----|
| 7.13 Comparison between the different Moho models. | 116 |
| 7.14 Maps of correlation coefficients estimated between synthetic waveforms and recordings. | 117 |
| 7.15 Sensitivity to topography and flat free surface. | 118 |
| 7.16 Snapshots of the wavefront evolution obtained via wave-modelling. . . | 119 |

List of Tables

| | | |
|-----|--|-----|
| 4.1 | Radiative-transfer simulations - Model setup: layers thickness. | 56 |
| 4.2 | Radiative-transfer simulations - Model setup: P and S waves velocity and density. | 56 |
| 4.3 | Radiative-transfer simulations - Model setup: scattering parameters. . . | 57 |
| 7.1 | Wave equation modelling - Model setup: Earth and source initial models. | 102 |
| 7.2 | Wave equation modelling - Model setup: P and S waves velocity models and final Earth model. | 109 |

Introduction

Knowing the structure and composition of the Solid Earth is fundamental for all fields of Earth Science research, from the academic-led investigation of the Earth core, mantle, and crust to the detection of mineral-, water- and oil & gas resources. Seismology is the leading discipline when targeting the Earth interior from shallower to deeper structures. It provides valid answers by studying the waves propagation from passive and active seismic surveys. The seismic stations distributed on the Earth's surface detect the waves recording the travel times and the amplitude. Different analyses in terms of seismic velocity and attenuation can be performed using the station recordings to characterize the propagation medium. The joint application of velocity and attenuation tomography improves the reconstruction of structural features of the Earth at local, regional, and global scales. In this framework, measurements of direct- and coda-wave seismic attenuation show high sensitivity to crustal and upper-mantle heterogeneities (Romanowicz and Mitchell, 2007). This information can be mapped in space depending on the characteristics of the studied phases (e.g., direct or refracted waves), their sensitivity to space and their dominant frequency content (Dahlen and Baig, 2002).

When the seismic information is used to map the Earth structure, sharp lateral variations of the medium properties strongly affect the seismic wavefield and the redistribution of energy in space and time. Studying how waves propagate and respond to these variations allows the retrieval of information about the media. Two structural settings where these variations produce important trade-offs in modelling are oceanic basins characterized by mixed continental-oceanic crust and highly scattering and absorption media (i.e., magmatic systems). The contributions from the random small-scale heterogeneities and the large-scale (deterministic) discontinuities are difficult to separate. The discrimination between the stochastic signature and the coherent wave propagation is fundamental for improving imaging techniques of oceanic basins, submerged continental crust and extended magmatism.

My PhD project tackles this problem from a tomographic and modelling perspec-

tive by simulating heterogeneous seismic wavefields with Radiative Transfer and wave-equation methods. The final scope is to provide novel tomographic images of these challenging environments when the scale of the heterogeneity and the wavelengths forbid a standard description in terms of single scattering or diffusive processes. My PhD focuses on the importance of modelling both the coherent and the stochastic wavefields to reconcile regional-scale imaging of continental, magmatic and oceanic lithosphere with the geodynamic interpretation of the evolution process (Nardoni et al., 2021, Nardoni et al. in preparation). The project combines seismic attenuation tomography with radiative transfer and wave-equation modelling of the seismic wavefield to improve the imaging of oceanic crust, including realistic topography and rheologically-driven seismic parameters.

The joint application of forward modelling and seismic coda attenuation tomography has improved our ability to discriminate between coherent reflections and reverberations produced by structural interfaces, such as the Moho, and the random heterogeneity that characterizes both crust and mantle. The Italian peninsula and the Tyrrhenian basin are the ideal environments to test the potential of seismic tomography and modelling in the presence of crustal reverberations, crustal pinches, and volcanic materials. This study has provided the first crustal attenuation model of the Italian peninsula, showing that coda attenuation at low frequencies can detect variations in Moho depths: in theory, this provides a way to map the Moho with regional seismicity, without using teleseisms. In the first part of my research, I have modelled the effects of lateral variations of crustal structures and properties on seismic energy propagation across these areas and obtained the first diffusion-based coda attenuation model of the Italian peninsula and Tyrrhenian basins. I have used novel forward modelling (Sanborn et al., 2017) and inversion (De Siena et al., 2017) open-access codes based on both eikonal approximation and Radiative Transfer theory (RTT). These models close the gap between frequencies and scales where wave-equation-based and adjoint methods encounter some of their greater challenges. Wave-equation methods and finite difference approach (OpenSWPC - Maeda et al. (2017)) are then necessary to reconcile mixed oceanic-continental models of the crust with regional-scale images obtained across the lithosphere (e.g., Blom et al., 2020).

In the second part of the project, wave-equation methods and codes based on Finite Differences (OpenSWPC - Maeda et al. (2017)) are employed to investigate the effects of the 3D propagation on the full waveforms. OpenSWPC is a code developed by the

heterogeneous Earth community (Sato et al., 2012), tailored to work in high-attenuation lithospheric media. In addition to deterministic interfaces, the wave propagation modelling includes statistical fluctuations of the velocity field that characterize seismic wave propagation at the crustal scale.

Combined imaging and modelling results can thus model crustal reverberations and can finally be used to map Moho depths with regional earthquakes. This framework thus enables the definition of a joint wave-equation and radiative-transfer-based forward modelling scheme for tomographic imaging and for mapping crustal parameters, especially across the oceanic basins.

In the following chapters, I will present the imaging and modelling methods and results by introducing first the theoretical background and, then, the data analysis.

Chapters 1 and 2 describe the theory of seismic wave attenuation and tomography in the framework of seismic tomography applications at different scales and settings.

Chapter 3 introduces the radiative transfer theory and its application to the modelling of seismic energy envelopes, then introduces the simulation tool used in this project (Radiative3D).

Chapter 4 presents the application of coda attenuation imaging and radiative transfer based simulations across Italy and the Tyrrhenian basin. It illustrates the methodology and the obtained results of my paper (Nardoni et al., 2021) published in *Physics of Earth and Planetary Interior*.

Chapters 5 and 6 describe the wave equation modelling approach and the finite-difference based simulation tool (OpenSWPC).

Chapter 7 presents the results of full-waveforms modelling and the sensitivity tests of the wavefield response to structural variations. The results described in this chapter are part of the new paper, submitted to *Surveys in Geophysics* (preprint available on ResearchSquare).

Chapter 1

Seismic Wave Attenuation

The structure of the Earth has been extensively studied using seismic waves generated by natural earthquakes and artificial sources. The basic view of the Earth consists of a series of horizontal layers having different elastic properties, which are determined from the travel times of body waves and surface waves dispersion curves. Three-dimensional structures having a spatial scale larger than the predominant seismic wavelength have been characterized using velocity tomography based on travel-time data. Forward and inverse waveform-modelling methods have been developed to model deterministic structures and the Earth's interior dynamics (Yuan and Romanowicz, 2010; French and Romanowicz, 2014). However, high-frequency (> 1 Hz) seismograms contain wave trains following the direct S-wave or crustal phases that cannot be explained by the deterministic structures, which are well described by the travel time tomography. Aki and Lee (1976) first focused on the tail portion of seismograms of local earthquakes and considered these wave trains, known as *coda waves*, as direct evidence of the random heterogeneity of the lithosphere. Coda waves (Fig. 1.1) appear as random signals having an envelope whose amplitude smoothly decreases with increasing lapse time measured from the origin time of an earthquake. Aki (1969) proposed that coda waves are the results of incoherent waves. Observations based on array analysis have confirmed that these wave-trains are incoherent waves scattered by randomly distributed heterogeneities in the lithosphere, which are characterized by random sizes and contrasts of physical properties (detailed characteristics of coda-waves are given in Sec. 1.4).

The characteristic scale of the heterogeneities that mostly influence a wave is comparable with its wavelength. Strong random fluctuations in seismic velocity and density having short wavelengths suggest a description of the Earth as a medium character-

ized by random spatial velocity fluctuations and highlight the importance of seismic wave scattering processes. In the last decades, geophysicists have been investigating the relationship between seismogram envelopes and the spectral structure of the random heterogeneity in the Earth using the radiative transfer theory (Wegler et al., 2006; Sens-Schönfelder et al., 2009; Lee et al., 2010; Sanborn and Cormier, 2018). The scattering process of seismic waves in the inhomogeneous Earth has been mathematically and physically explained to allow a characterization of the statistical properties of the inhomogeneity complementary to the standard stratified Earth view (Sato et al., 2012).

1.1 Attenuation Processes

The development of regional velocity tomography (Aki and Lee, 1976; Thurber et al., 2009; Xu and Zhao, 2009), which uses travel-time readings from seismograms of teleseismic waves, local earthquakes, or active sources, has determined the inhomogeneous velocity structure on scales from a few meters to a few tens of kilometres in many regions of the world. In addition, attenuation plays a key role in characterizing the Earth's heterogeneities: seismic waves have long been known to attenuate at a rate greater than that predicted by the geometric spreading of their wavefronts, pointing out that other mechanisms should be invoked to justify the measured attenuation values.

Scattering due to randomly-distributed small-scale heterogeneities and energy absorption by the media (elastic and anelastic attenuation, respectively) significantly affect seismic wave propagation and consequently the seismograms of local earthquakes, especially at high frequencies. Scattering excites long-lasting coda waves after the direct arrival and broadens the apparent duration of oscillations with increasing travel distance (Fig. 1.1). To model these observations and characterize the lithosphere (i.e., the region of the Earth down to about 100 km), a stochastic treatment of the wavefield is adopted to describe both heterogeneous media and wave propagation through them.

Because of its strong dependence on temperature, partial melting, and water content, mapping anelastic attenuation in the Earth has the potential to provide valuable information on Earth's three-dimensional (3D) structure and dynamics, jointly with what can be learned from mapping velocities. The attenuation parameters, which are frequency- and amplitude-dependent, allow the retrieval of information about the material properties such as pressure, temperature, fracturing and fluid content (Lees, 2007). A significant challenge is to separate the effects of anelastic (or intrinsic) attenuation from those of

elastic scattering and focusing due to propagation in 3D structures. The joint application of velocity and attenuation tomography thus improves the reconstruction of structural features of the Earth at a local, regional, and global scale. Measurements of direct- and coda-wave seismic attenuation show high sensitivity to crustal and upper-mantle heterogeneities (for a review see Romanowicz and Mitchell, 2007). This information can be mapped in space depending on the characteristics of the studied phases (e.g., direct or refracted waves) and their frequency-dependent sensitivity to space (Dahlen and Baig, 2002).

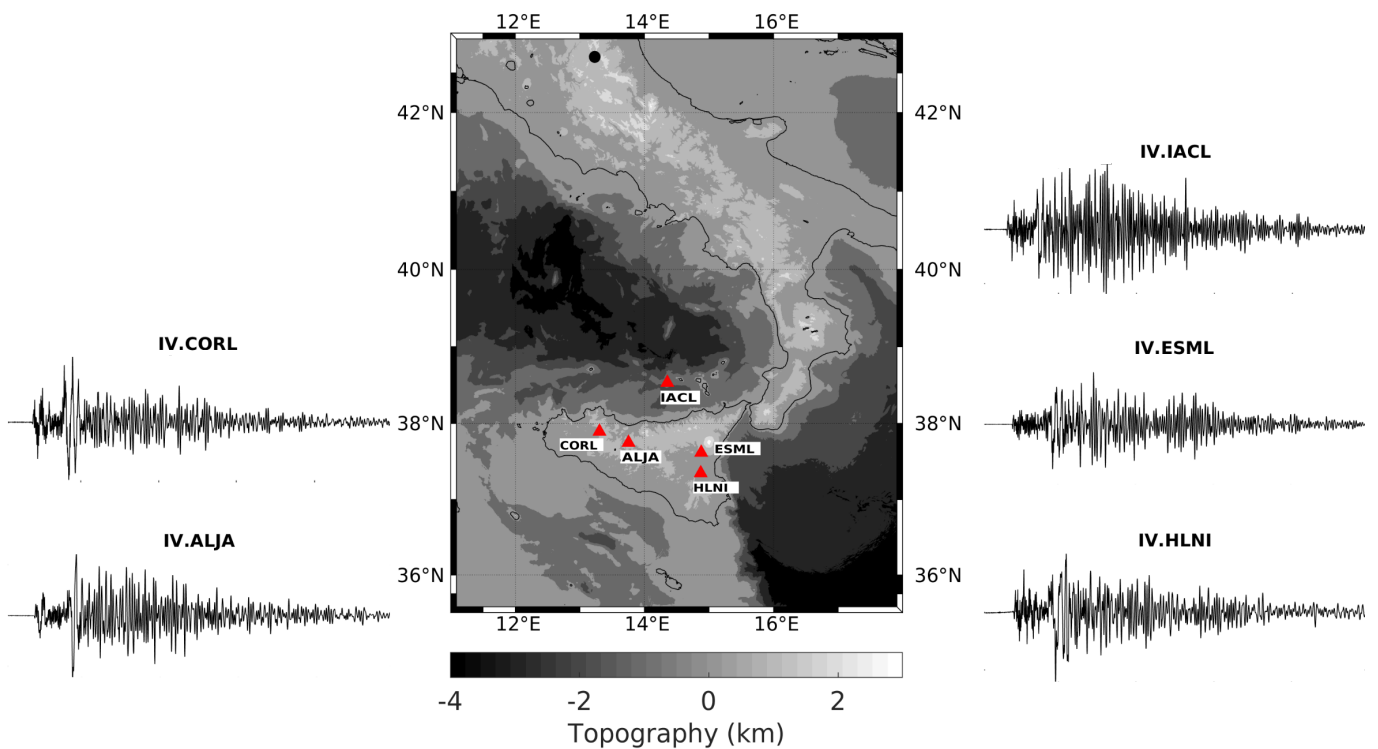


Figure 1.1: Seismograms that are recorded at different locations showing differences in attenuation and amplitude. The red triangles are the stations and the black dot is the seismic source.

1.2 Heterogeneity in the lithosphere

The characterization of the Earth is based on geophysical (e.g., seismic velocities and density of rocks) and geological (e.g., mineralogical composition and grain size

distribution, both controlled by the evolution processes of the rocks) observations of its physical properties. Tectonic processes such as faulting, subduction, and large-scale crustal movements related to plate tectonics contribute to increase the lithosphere heterogeneity. The wide variation of rocks and elastic properties within the Earth's lithosphere provides evidence of heterogeneity at different scales. The density controls the P- and S-wave velocities as stated by Birch's law (Birch, 1960). Seismic velocity increases roughly linearly with the mass density of rocks having the same mean atomic weight. Fractures (from microscopic to many tens of meters) are important factors influencing the elastic properties of crustal rocks. The fractures can lead to anisotropy of the elastic properties of the rock as they may have a preferential alignment that depends on the evolution process or the oriented variation in stress magnitude. In volcanic regions, variations in rock properties can occur on scales of a few m to a few km due to variations in the composition of magma erupted at differing stages of a volcano evolution. Another example of heterogeneity and anisotropy is the result of the layering of rocks, such as in sedimentary formations. Heterogeneities in sedimentary formations could be due to the formation processes, the variations in porosity and pore fluids, and the tectonic processes that act on the rocks after deposition. On a larger scale, movements and collisions of lithospheric plates at plate boundaries, such as subduction zones or collision zones, cause rocks of different types to merge.

Different imaging methods are used to characterize the Earth's complex structure from large to small scale. In Sections 1.3 and 1.4, the primary imaging techniques are introduced and are based on deterministic and stochastic observations, describing large- and small-scale structures, respectively.

1.3 Imaging by deterministic observations

The deterministic characterization of the spatial heterogeneity of the Earth's lithosphere is one of the main goals of seismology. Characterizing the spatial heterogeneity of the lithosphere allows a better understanding of the mechanism by which the crust has evolved, volcanic processes, and the nature of active seismic zones.

Several seismic studies use reflection and refraction methods to characterize the crust. These two mechanisms depend on impedance contrasts that characterize layers interfaces (e.g. interface between sediment and bedrock). The impedance (i.e., the product of density and seismic velocity) contrast causes reflection (back to the surface) and

refraction according to Snell's law. Refraction and reflection thus help the reconstruction of subsurface structures and are complementary to other tomographic methods.

Reflection seismology is a method of exploration geophysics that uses the principles of seismology to estimate the properties of the Earth's subsurface from reflected seismic waves (Waters and Waters, 1981; Thomsen, 1988; Warner, 1990). The method requires an active seismic source of energy and the detection of waves by an array of receivers (or geophones) at the surface. It is based on the study of travel times of reflected waves, whose propagation is governed by the contrast of impedance across the medium, and it attempts to reconstruct the pathways of the waves in order to build up an image of the subsurface layers. Reflection studies are generally used on a local scale for studies of a few to a few tens of km and to depths of up to 15 km. On a larger scale, observations of earthquake waveforms provide evidence for reflected phases generated by deep interfaces in the Earth. (Ross et al., 2004; Zhang et al., 2019).

Refraction seismology is employed for studying regional seismic structures to depths as great as the Moho. Refraction from the Moho provided the first direct evidence of the large contrast in seismic velocity between the crust and mantle. When a ray encounters an inhomogeneity in its travels (e.g., contact between two rocks with different velocities), the incident ray transforms into several new rays. If the second layer is characterized by a seismic velocity higher than the velocity of the first one, the transmitted wave is critically refracted and generates a head wave. In refraction seismology, the relevant seismic arrivals are the direct wave and the "head wave". The studied regions extend from the order of a few tens to hundreds of km. The layered velocity structures are the first information that is usually derived from refraction surveys and represent the most basic information about heterogeneity in the crust (Klemperer et al., 1986; Improtà et al., 2000).

Figure 1.2 shows the potential of seismic refraction and reflection in detecting different geological stratification. Finetti (2003) presents an extension of seismic reflection analysis to the identification of the main Earth layers discontinuities as well as sedimentary layers, crustal basement and Moho interface.

The *receiver function* method is used for deterministic imaging of the Earth heterogeneity by using the information from teleseismic earthquakes recorded at a three-component seismograph. A teleseismic P-wave will generate P-to-S conversions at boundaries, such as the Moho (crust-mantle boundary). Those P-to-S converted phases are recorded in the radial component at the receiver; however, the vertical-component P-

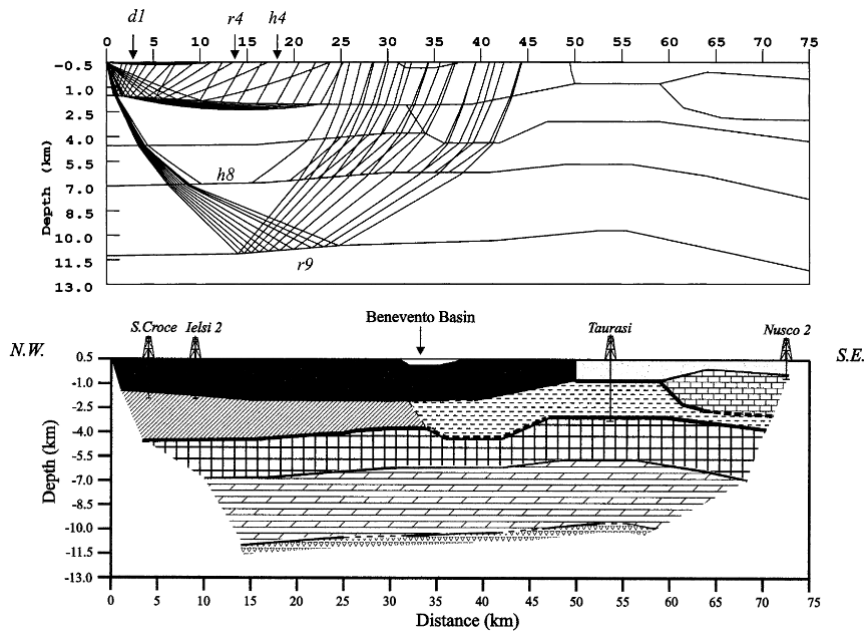


Figure 1.2: Study of reflected, refracted phases and head waves from active seismic data (after Improta et al., 2000). The velocity analysis leads to different geological characterization of each layer.

wave is almost the same as the incident P-wave for near-vertical incidence. The receiver function method (Langston, 1979) uses the deconvolution of the horizontal component S-wave trace in the radial direction by the vertical component P-wave trace for measuring the P-to-S conversion depth and the velocity contrast. The difference in travel time between the generated S-wave and P-wave contains information about the depth to the boundary and about the P- and S-wave velocities. The receiver function method has been widely used to reveal layered velocity structures.

Seismic tomography was firstly applied to waves travel times to obtain a 2D or 3D model of the Earth's structure from laboratory to global scale. This technique is used to image the subsurface of the Earth with seismic waves produced by earthquakes or explosions. The data received at seismometers are used to solve an inverse problem for creating 2D or 3D images of velocity anomalies which may be interpreted as structural, thermal or compositional variations. Further details on the theory and the application of this method are given in Chapter 2.

Figure 1.3 shows an estimation of Moho depth for the Italian peninsula obtained from Piana Agostinetti et al. (2009) using receiver functions analysis and a grid search approach.

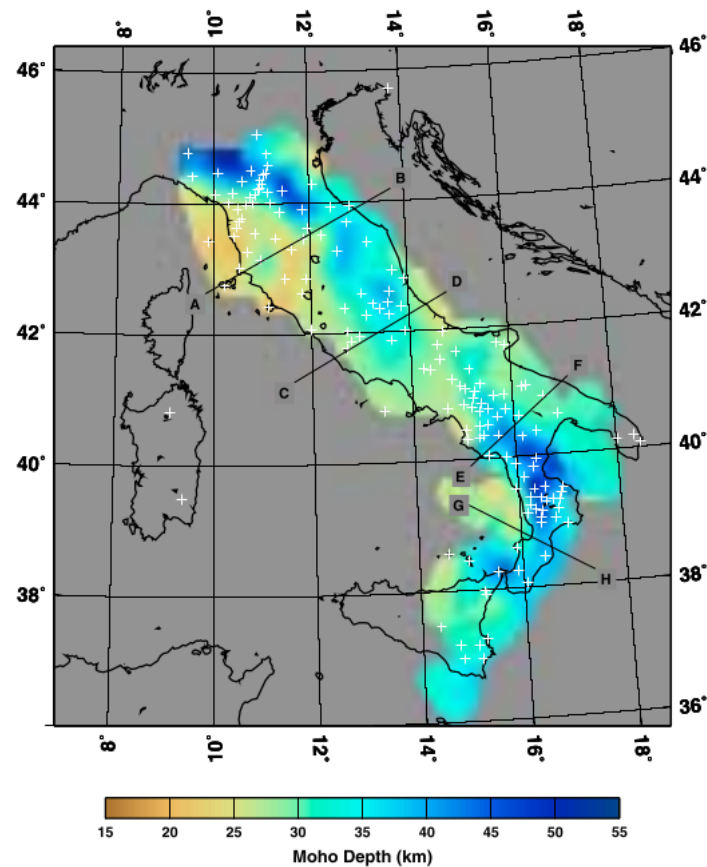


Figure 1.3: Map of Moho depth using Moho depth values obtained from receiver functions (from Piana Agostinetti et al. (2009)).

1.4 Stochastic approach: Coda Waves

Complementary to velocity, attenuation of seismic waves is a powerful observation to characterize the lithosphere heterogeneities at different frequencies. The most important evidence that the Earth is heterogeneous is the presence of an incoherent waves train after the arrival of S or crustal phases whose amplitude decreases exponentially as the lapse time increases (Fig. 1.1). As mentioned in the previous sections, this waves train is named *coda waves*. The longer the waves travel, the greater the variety of heterogeneities they encounter. The later portions of a seismogram can thus be considered as a result of some kind of averaging over many heterogeneities.

While direct wave amplitude decreases with increasing epicentral distance, the average coda amplitudes have nearly equal amplitudes with respect to the epicentral distance. Rautian and Khalturin (1978) studied amplitudes of bandpass-filtered seismo-

grams for a wide range of lapse times. The authors found that amplitudes of the early portions of seismograms are different from station to station and coda amplitudes have a common shape at all the stations after about two times the S-wave arrival suggesting that high-frequency coda waves are incoherent. To explain the observed smooth temporal decay of coda amplitude (independent of epicentral distance), Aki and Chouet (1975) proposed a model in which S-coda is composed of S-waves that have been scattered by heterogeneities distributed in a large region around the direct wave path from the source to the receiver. Reverberations in soft layers or the trapping and release of seismic energy cannot explain the observed features. Aki and Chouet (1975) first summarized the characteristics of high-frequency coda waves of local earthquakes as follows:

- The spectral contents of the early part of a local earthquake seismogram depends on travel distance and the nature of the wave path. The difference in spectrum among stations is relevant in the early part of the signal and tends to disappear in the coda.
- For a given local earthquake at an epicentral distance shorter than about 100 km the total duration of a seismogram (the length of time from the beginning of P waves to the end of coda) is nearly independent of the epicentral distance and can be used effectively as a measure of earthquake magnitude.
- The power spectra of coda waves from different local earthquakes decay as a function of time from the earthquake origin time with a trend which is independent of the distance and the nature of the path between epicenter and station.
- The above time dependence is also independent of the earthquake magnitude at least for small earthquakes with $M_L < 6$.
- The S-coda amplitude depends on the local geology of the recording site.
- S-coda waves have the same site amplification factor as that of direct S-waves confirming that coda waves are composed primarily of S-waves

1.4.1 Coda Attenuation Parameters

Coda wave generation models have been based on the Earth's lithosphere as composed of a random and uniform distribution of point-like scatterers embedded in a homogeneous background medium having a constant propagation velocity (Fig. 1.4).

Diffraction effects caused by gradual changes in velocity are neglected. Energy propagation modelling in a medium having distributed point-like scatterers is easier than wave propagation modelling in a random media. As phases in coda waves look random and incoherent, these models focus on the distribution of energy in space and analyze the waveform envelopes. Sato et al. (2012) review the proposed models and mathematical description for coda attenuation. The parameters for controlling the shape and amplitude of coda waves are the *total scattering coefficient* g_0 and the *coda quality factor* Q_c estimated from the observed seismogram envelope (Fig. 1.6).

The relation between Q_c and coda physical interpretation has been discussed for a long time. The two main causes for attenuation (as mentioned in Sec. 1.1) are scattering caused by small-scale heterogeneities of the lithosphere and absorption of seismic energy by inelastic processes, which depend on temperature, mineralogy and fluids. Q_c is thus given by these two contributions as follows

$$Q_c^{-1} = Q_{sc}^{-1} + Q_i^{-1} \quad (1.1)$$

where sc and i stand for scattering and inelasticity, respectively. Sec. 1.4.1.1 shows the mathematical formulation of the scattering contribution Q_{sc} based on the total scattering coefficient g_0 . However, the scattering and absorption processes cannot be easily separated when we estimate Q_c from the data. Aki and Chouet (1975) thus proposed two different models to interpret coda waves, and then Q_c , and to finally isolate Q_i : single-scattering (Sec. 1.4.1.2) and multiple scattering (Sec. 1.4.1.3) models.

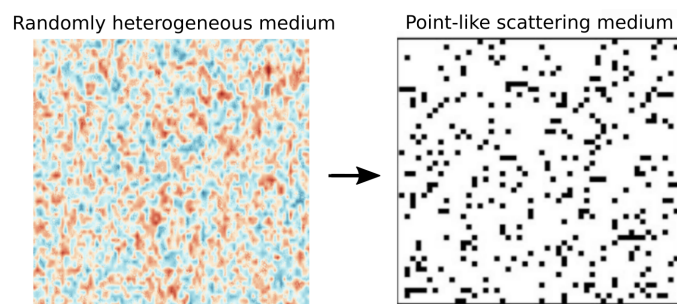


Figure 1.4: The media characterized by random heterogeneity (left panel) are represented as composed of point-like scatterers randomly distributed (right panel).

1.4.1.1 Scattering characteristics

The energy-flux density is defined as the amount of energy passing through a unit area perpendicular to the propagation direction per unit time. As illustrated in Fig. 1.5, an incident plane wave with energy-flux density J^0 is considered to interact with a scatterer and generates spherically outgoing waves with energy-flux density J^1 . Without considering the polarization and partition of energy into three components, the amount of energy scattered per unit time into a given solid angle element $d\Omega$ is $J^1 r^2 d\Omega$, where $r^2 d\Omega$ is the corresponding surface element. The differential scattering cross-section of the scatterer is defined as follows

$$\frac{d\sigma}{d\Omega} = \frac{J^1 r^2}{J^0} \quad (1.2)$$

A randomly inhomogeneous medium is modelled as a homogeneous background medium having propagation velocity V_0 and distributed point-like scatterers with number density n (Fig. 1.4). The distribution is assumed to be randomly homogeneous and isotropic, and each scattering is characterized by the differential scattering cross-section $d\sigma/d\Omega$ given by Eq. 1.2. According to Sato et al. (2012), we can define the scattering coefficient as the scattering power per unit volume given by the product of the number density and the differential scattering cross-section:

$$g \equiv 4\pi n \frac{d\sigma}{d\Omega} \quad (1.3)$$

where the cross-section usually depends on frequency and the quantity g has the dimension of reciprocal length. The total scattering coefficient is defined by the average over all directions:

$$g_0 \equiv \frac{1}{4\pi} \oint g d\Omega = n \oint \frac{d\sigma}{d\Omega} d\Omega = n\sigma_0 = l^{-1} \quad (1.4)$$

where σ_0 is the total scattering cross-section, which is the integral of the differential scattering cross-section over solid angle. The total scattering coefficient is the reciprocal of the mean free path l .

The wave energy decreases with increasing travel distance due to scattering and we can thus define a scattering attenuation term. Considering an incident plane wave with angular frequency ω , the energy-flux density at travel distance x decays as $\exp(-g_0 x) =$

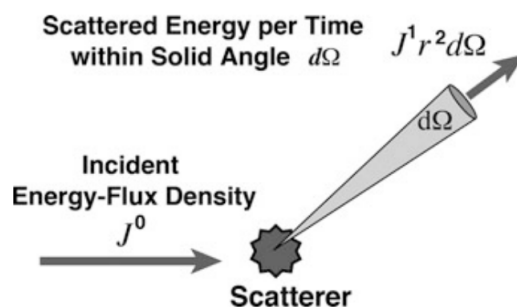


Figure 1.5: Concept of the differential scattering cross-section $d\sigma/d\Omega$ of a single scatterer.

$\exp(-Q_{sc}^{-1}k_0x)$, where $k_0 = \omega/V_0$, and the scattering attenuation is

$$Q_{sc}^{-1}(\omega) = \frac{g_0}{k_0} = \frac{g_0 V_0}{\omega} \quad (1.5)$$

In the case of isotropic scattering, $d\sigma/d\Omega = \sigma_0/4\pi$ and $g = g_0$.

1.4.1.2 Single scattering approximation

Aki and Chouet (1975) propose the single-scattering models for coda waves generation. The coda is considered as a superposition of backscattering wavelets from randomly distributed and discrete scattering sources in a medium with uniform velocity. Each wavelet is due to a single scatterer in the absence of the other scatterers. In this model, the scattering is a weak process. Assuming single scattering and, in the first order, the source and the receiver at the same location, Aki and Chouet (1975) developed a model for a *single-backscattering* process introducing an equation for the coda wave energy density at frequency f (central frequency of the bandpass filter applied to seismogram) and elapsed time t from the origin:

$$E(f, t) \propto S t^{-m} e^{-\pi f t / Q_c} \quad (1.6)$$

E is the seismic energy per unit volume within a unit frequency band. m is determined by geometrical spreading; $t = 2r/v$, so the energy density is proportional to $1/r$, if m is equal to 1 and indicates surface waves, or $1/r^2$, if m is 2 and indicates body waves. Q_c is the quality factor which takes into account the phenomenological coda attenuation. S is the earthquake source term, which varies with earthquake magnitude.

As a further step, it was calculated the single scattering energy considering a receiver at position x located at a distance r from a point source at the origin in the case of isotropic scattering (Sato et al., 2012). The single-scattering energy, given by the spatial integral of energy density $\int \int \int_{-\infty}^{\infty} E(\mathbf{x}, t) d\mathbf{x}$, increases monotonously with increasing lapse time. To satisfy the conservation of total energy, the integral of energy density has been multiplied by the exponential scattering attenuation term $e^{-\omega t/Q_{sc}}$ to account for energy lost due to scattering by the direct energy propagation term (Sato et al., 2012).

When waves are radiated from a point source in a random medium, single scattering provides a good description of the propagation characteristics at small distances from the source and at a short lapse time from the source origin time. However, multiple scattering dominates over single scattering as travel distance or lapse time increases. As travel distance increases, incoherent fluctuation waves increase and the interference effects destroy the phase information. Besides, the single scattering model is the most appropriate for the coda generation model at the longest wavelengths. Several works modelled the coda of seismic phases recorded at regional and global scales relying on the single scattering approximation and assuming the coda sensitivity to be a scattering ellipsoid (Xie and Mitchell, 1990; De Souza and Mitchell, 1998; Mitchel et al., 1998; Mitchell et al., 2008, 2015).

1.4.1.3 Multiple scattering model: diffusive approximation

In the single-scattering model, the coda is a superposition of scattered waves, each of them due to a single scattering in the absence of the other scatterers. At large lapse time, it is reasonable to assume that direct energy becomes small and that multiple scattering produces a smooth spatial distribution of energy density. In the *multiple scattering* model, the seismic energy transfer can be considered as a diffusion process because of the multiple scattering that affects the waves. Consider a medium having a randomly homogeneous and isotropic distribution of isotropic scatterers in which energy W is spherically radiated from a source and is scattered through diffusion. A strong multiple scattering process can be well described by the diffusion equation (Aki and Chouet, 1975)

$$\frac{\partial E}{\partial t} = D \nabla^2 E - \frac{\omega}{Q_c} E \quad (1.7)$$

where E is the seismic energy per unit volume, D is the diffusivity and the last term represents the loss by anelasticity which turns the seismic energy into heat. In this case, Q_c is the intrinsic quality factor Q_i and does not include the loss by scattering. The

solution for a point source in time and space, where Q_c can be considered Q_i , is given by

$$E^D(\mathbf{x}, t, \omega) = \frac{W(\omega)}{(4\pi Dt)^{3/2}} e^{-\frac{r^2}{4Dt}} e^{-Q_i^{-1}\omega t} \quad (1.8)$$

for three-dimensional diffusion corresponding to body wave scattering. The exponent $-3/2$ is intermediate to body wave (-2) and surface wave (-1) single-scattering theories. $W(\omega)$ is the total seismic energy generated by the earthquake within the unit frequency band around ω . For large t and small distance $(x^2 + y^2 + z^2)^{1/2}$ at which the coda waves are observed, Eq. 1.8 becomes a function of only time t and is independent of distance.

1.5 Q_c^{-1} Measurements

As discussed previously, in addition to seismic velocity measurements, attenuation provides relevant information about the structure of the Earth. In fact, mapping the frequency-dependent anelastic absorption (related to temperature, chemical composition, melt or fluid contents) and scattering of seismic waves represents valid support for velocity tomography measurements. Scattering loss and intrinsic absorption both control the propagation of short period S waves through the crust. The complex pattern of seismic radiation generated by an earthquake generally affects both the estimation of the total seismic attenuation and the separation of specific attenuation mechanisms using direct waves. Del Pezzo et al. (2011) used the MLTWA (*Multiple lapse time window analysis*, Fehler et al. (1992)) in order to obtain separate estimates of the average inverse quality factors for S waves, i.e. Q_{sc}^{-1} and Q_i^{-1} , or a combination of these two parameters. The method is based on the fit of the measured energy envelope of the waveforms to the seismic energy envelope theoretically predicted by the radiative transfer theory, in three time windows.

To evaluate separately the intrinsic attenuation and scattering, intrinsic attenuation can be estimated by fitting the energy envelope of seismic coda waves, which decays following the exponential law described in Eq. 1.8 (diffusive approximation - Sec. 1.4.1.3)

$$E(t, f) = S(f)t^{-\alpha} e^{-2\pi ft/Q_c} \quad (1.9)$$

where at long lapse time Q_c represents the intrinsic quality factor with good approximation. E is the energy, $S(f)$ is a frequency dependent source and/or site term, t is the lapse time, f is the frequency and α is a positive exponent depending on the physical model

used to describe coda waves. This method is applied from local to regional scale in the volcanic and continental regions (Calvet et al., 2013; Mayor et al., 2016; De Siena et al., 2017; Napolitano et al., 2019). To measure the multiple forward scattering in comparison with absorption, the peak-delay method is used. Peak delay is defined as the time lag between the S-wave arrival and the maximum amplitude of the arrival (Takahashi et al., 2009). Comparison of coda-Q and peak delay time measurements allows the interpretation of the origin of seismic attenuation (scattering/absorption) (De Siena et al., 2016; Napolitano et al., 2019).

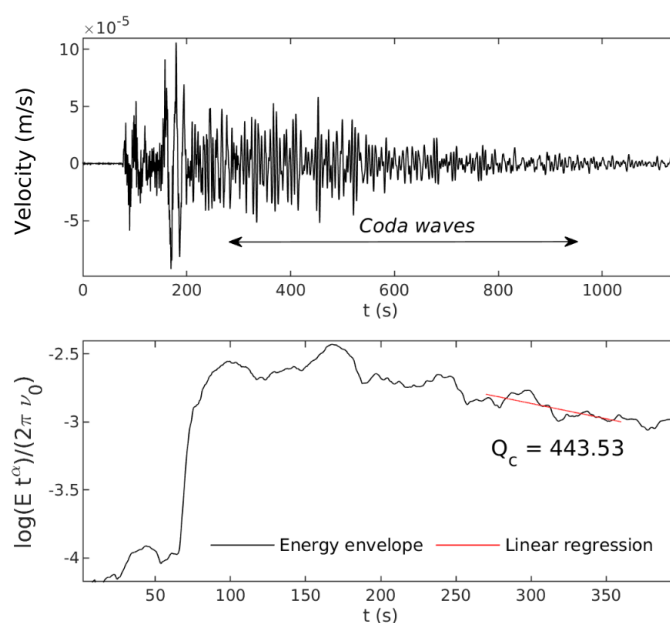


Figure 1.6: Example of vertical component velocity seismogram recorded at regional distance (534km) and the envelope in the frequency band 0.5-1.5Hz.

The variation of coda waves quality factor from region to region is large. In general, Q_c^{-1} is about 10^{-2} at $1Hz$ and decreases to about 10^{-3} at $20Hz$. The frequency dependence can be written in the form of a power of frequency f as it follows (Sato et al., 2012)

$$Q_c = Q_0 f^n \quad (1.10)$$

This power law is fitted for Q_c at each central frequency f . This analysis allows to verify if the average of Q_c changes with frequency. From the experimental value of Q_c , Q_0 and n can be calculated and compared with the values of other zones. As Q_c depends on n , the use of Eq. 1.10 allows to understand if we are looking at the crust or more

heterogeneous zones.

Chapter 2

Seismic tomography

Seismic tomography aims at obtaining 2D or 3D models of the Earth's structure, using travel times and amplitudes from both body (P and S) and surface waves. Seismic tomography was introduced into seismology by Aki and Lee (1976); Aki et al. (1977), who showed how to use travel times from local and teleseismic earthquakes to obtain a 3-D velocity structure of the region beneath the seismic network. Based on travel times, velocity tomography has been intensively applied on regional and global scales to determine the P- and S-wave velocity structure of the lithosphere and deeper structures (Thurber et al., 2009; Xu and Zhao, 2009; French and Romanowicz, 2014). Travel-time tomography thus answers questions about the geodynamics and tectonics, e.g., by estimating the amount of the subducted lithosphere and detecting the upwelling of hot material from the mantle (Spakman and Wortel, 2004; Piromallo and Morelli, 2003).

However, as mentioned in Chapter 1, the deterministic structures do not explain all the observations. Because of its strong dependence on temperature, partial melting, and water content, seismic attenuation has the potential to provide valid information on Earth's structure and dynamics, in addition to velocity imaging.

In the following sections, I introduce the theory of the inverse problems and its applications to coda-waves attenuation imaging.

2.1 Inverse problem and regularization

Tomography is based on the solution of a linear or non-linear inverse problem, which, given observed data (e.g. travel times of a phase), allows the building of a model of the velocity structure. Discrete inverse problems can be posed by assuming that the physics of a process is known and, for a set of model parameters described by a vector

\mathbf{m} , gives rise to a set of observed data described by a vector \mathbf{d} . The data can thus be considered the result of a function G acting on the model parameters and this can be expressed, in the case of a linear inverse problem, by the equation (Aster et al., 2011)

$$\mathbf{d} = G\mathbf{m} \quad (2.1)$$

where the matrix G is called the data kernel. The solution to inverse problems is a particular model \mathbf{m} that minimizes some measure of the distance between the actual data and $G(m)$ (the norm of residuals) and it rarely leads to exact information about the values of the model parameters as there may be many models that adequately fit the data (non- uniqueness of the solution). A parameter estimation problem aims at representing spatial variations of a physical quantity, such as seismic velocity, and the model parametrisation, i.e., the node spacing, is fundamental, as the inverse problem ground on it. The parameters defining the model can be an n -element vector \mathbf{m} and a finite number of data points can be expressed as an m -element vector \mathbf{d} . Three different cases can be distinguished in order to discuss the inverse problem solution: the solution is *overdetermined* if $m > n$, *underdetermined* if $m < n$ and *exactly determined* if $m = n$ (G is a square matrix). A method of analyzing and solving least squares problems in ill-conditioned systems is the singular value decomposition, or SVD (Aster et al., 2011). In the SVD an m by n matrix G is factored into

$$G = U\Lambda V^T \quad (2.2)$$

where U is an m by m orthogonal matrix with columns that are unit basis vectors spanning the data space, R^m , V is an n by n orthogonal matrix with columns that are basis vectors spanning the model space, R^n , and Λ is an m by n diagonal matrix with non-negative diagonal elements called singular values λ . In order to minimize the residuals between the data and the values predicted from the model, a *generalized inverse matrix* can be defined

$$G^{-g} = [G^T G]^{-1} G^T \quad (2.3)$$

The solution to the inverse problem (Eq. 2.1) can be constructed from the singular-value decomposition as (Lay and Wallace, 1995)

$$\mathbf{m} = V_p \Lambda_p^{-1} U_p^T \mathbf{d} \quad (2.4)$$

where V_p and U_p are obtained from the partition of Λ into a submatrix Λ_p of nonzero singular values and several zero matrices. If the inverse problem is ill-conditioned, i.e., $\lambda_i \rightarrow 0$, small singular values can be excluded to obtain a solution close to the natural solution, but this approach can worsen the model and data resolution. Instead of choosing a sharp cutoff for the singular values, it is possible to include all the singular values while damping the smaller ones. This methodology is known as regularization. Ill-posed problems thus need additional assumptions: regularisation parameters are thus employed to solve the inversion by preventing model over-fitting and smoothing the non-uniqueness of the solution. Tikhonov regularization is one of the most commonly used for regularization of linear ill-posed problems. Considering the solution instability with respect to small changes in data noise and initial conditions, the aim is to prevent an ‘overfit’ of the data (by fitting noise) and to take into account the limitations of observations (e.g., array of stations not well distributed) (Rawlinson et al., 2014). In practice, all regularization methods for computing stable solutions to inverse problems involve a compromise between the ‘size’ of the regularized solution (how large is the value of the sum of the model parameters m_i) and the quality of the fit that it provides to the given data. What distinguishes the various regularization methods is how they measure these quantities, and how they decide on the optimal compromise between the two quantities.

In seismic tomography, solution robustness can be assessed using synthetic reconstruction tests. To test the spatial resolution of solutions produced by linear or nonlinear inversion schemes, the most common tool is the checkerboard resolution test in which the synthetic model comprises an alternating pattern of higher and lower wave velocity (or some other seismic property such as attenuation) in 2D or 3D (Fig. 2.1). Based on the actual source-receiver array, the inversion method is applied to the synthetic data set to recover the test model. Differences between the true and recovered model provide a basis for assessing the reliability of the solution (Rawlinson and Spakman, 2016).

2.2 Imaging of Q_c spatial variations

Seismic tomography applications involve mainly seismic velocity and attenuation. Seismic attenuation has become a powerful imaging attribute as it showed increased sensitivity to the small-scale heterogeneities of the crust and mantle. This parameter can be evaluated from direct- and coda-waves and mapped in space as a function of the

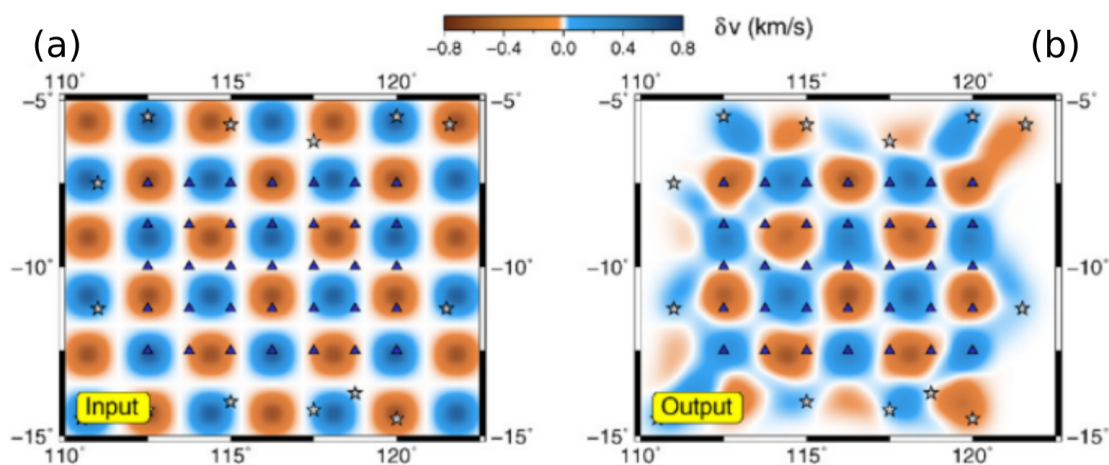


Figure 2.1: Example of a checkerboard resolution test (modified from Rawlinson et al., 2010): (a) synthetic model with alternating paths, (b) results of the synthetic data inversion.

frequency.

Coda waves attenuation imaging has been applied at the regional and local scale, and mainly in volcanic and continental areas. Depending on coda lapse time, it is possible to assume a single scattering (Romanowicz and Mitchell, 2007), multiple-scattering (Calvet et al., 2013) or diffusive approximations (Del Pezzo et al., 2016).

Without performing inversion, the regionalization approach has been employed for coda waves considering the sensitivity distributed within ellipsoids whose size increase with the lapse time (Mitchell et al., 2008). While this assumption grounds on the single scattering approximation, in the multiple scattering regime, the coda wave sensitivity is not distributed within an ellipsoid and strongly depends on the type of perturbation (scattering or absorption). In the diffusive model, the coda sensitivity to heterogeneities is larger at the locations of the source and the station (Pacheco and Snieder, 2005).

Calvet et al. (2013) adopt a regionalization approach to map coda attenuation in space assigning Q_c values to ray paths between stations and hypocentres. According to the higher sensitivity around the station and the source, the authors select a limited range of source-receiver distances and averaged the Q_c values of the paths crossing each block. Mayor et al. (2014) took a step forward in the regionalization approach and built sensitivity kernels to account for higher sensitivity around the source and the station. Using these kernels, Mayor et al. (2016) employ the regionalization approach to map spatial variations of seismic absorption at a regional scale (the Alps and Northern

Apennines).

Coda-wave sensitivity kernels can thus be defined to describe the sensitivity of coda waves to the space surrounding the source and receiver (Fig. 2.2). These kernels have improved the characterization of heterogeneous crustal layers (for a review see Sketsiou et al., 2020) as well as volcanic and faulted media (De Siena et al., 2017; Napolitano et al., 2019).

Del Pezzo et al. (2016) provide different sensitivity kernels using Monte Carlo simulation of the radiative transfer equation. These kernels are only valid at short lapse times and for highly heterogeneous and diffusive media and show that the sensitivity of coda waves to local variations of absorption is larger around the source/receiver and the area between them (Fig. 2.2 - K1). The weighting functions obtained via Monte Carlo simulations are the following

$$\begin{aligned}
 f[x, y, x_r, y_r, x_s, y_s] = & \frac{1}{4\pi\delta_x D^2 \delta_y} \exp \left[- \left(\frac{(x - \frac{x_r+x_s}{2})^2}{2(\delta_x D)^2} + \frac{(y - \frac{y_r+y_s}{2})^2}{0.5(\delta_y D)^2} \right) \right] \\
 & + \frac{1}{2\pi\delta_x D^2 \delta_y} \exp \left[- \left(\frac{(x - x_s)^2}{2(\delta_x D)^2} + \frac{(y - y_s)^2}{2(\delta_y D)^2} \right) \right] \\
 & + \frac{1}{2\pi\delta_x D^2 \delta_y} \exp \left[- \left(\frac{(x - x_r)^2}{2(\delta_x D)^2} + \frac{(y - y_r)^2}{2(\delta_y D)^2} \right) \right]
 \end{aligned} \quad (2.5)$$

where D is the source–station distance, x and y the spatial coordinates, $[x_r, y_r]$ are the station coordinates and $[x_s, y_s]$ the source ones and δ_x and δ_y are the spatial aperture of the weighting function.

Kernel-based coda attenuation imaging is applied by using both regionalization and inversion methods. De Siena et al. (2017) developed an inversion scheme of kernel-based coda-wave attenuation targeting volcanic media. The authors applied a frequency-dependent mapping of Q_c^{-1} at Campi Flegrei caldera using space-weighting sensitivity functions (Eq. 2.5) defined by Del Pezzo et al. (2016). The main assumption is all the seismic energy remains inside the propagation grid. The inversion is tested in the continental crust with thick Moho, for waveforms duration of 100s and in the absence of leakage in the mantle (Borleanu et al., 2017; Napolitano et al., 2019). Ogiso (2019) and Shito et al. (2020) applied the diffusive kernels to a wider area of lateral extension of about 500 km in southwestern Japan. This inversion procedure provides a forward model to image scattering and absorption, allowing to perform resolution tests, which

is a significant advantage of the inversion techniques.

The approximation of single, multiple scattering and diffusion and consequently the use of different kernels depend on the frequency range and the lapse time. The standard application at low frequencies requires the definition of scattering ellipsoids (using the SS assumption, e.g., Romanowicz and Mitchell (2007)) or segments in the multiple scattering approximation. At higher frequency and local scales, diffusive kernels are used. Diffusive kernels (Eq. 2.5) from Del Pezzo et al. (2016) are analytic and allow good resolution along the path and around the source and receiver. Other kernels are based hypothesis of Pacheco and Snieder (2005) and are lapse-time-dependent and valid independently of the presence or not of a diffusive regime. The corresponding 3D spatial sensitivity is given by a time-dependent function

$$K_{i,j}^{3D}[\varrho, t, B_0, Le^{-1}, v] = \int_0^T E^{3D}[r_{sq}, \tau, B_0, Le^{-1}, v] E^{3D}[r_{qr}, T - \tau, B_0, Le^{-1}, v] d\tau \quad (2.6)$$

setting the velocity v , the seismic albedo B_0 , the extinction length Le^{-1} at average values for the crust. E^{3D} is the energy envelope solution for a 3D model. In this case, the resolution between the source and receiver is lost. Akande et al. (2019) employ this 3D kernel function to obtain the first three-dimensional attenuation model in the Campi Flegrei area (Fig. 2.3). Gabrielli et al. (2020) compare the results of the inversion procedure obtained using diffusive kernels and the ‘‘Pacheco-Snieder’’ ones. They show the approach is equivalent using both diffusive kernels if the energy remains constrained in the single layer. The advantage of analytic kernels is that they allow a good resolution even though the area is not covered enough by sources and receivers (Fig. 2.2).

2.3 From rock samples to regional scale

While the phenomenological study of coda waves has been addressed to clarify the origin, the attenuation imaging studies aim at physically calibrating the Q_c measurements to correlate the lateral variation and the physical properties of the medium.

From rock samples to larger scales, the dependency of the coda quality factor on the physical properties of the media has been explored in different geological settings. Di Martino et al. (2021) present the first attempt for investigating the relationship between seismic attenuation measured from coda waves and rock properties. The authors found that coda attenuation is mainly influenced by the pore space distribution in sam-

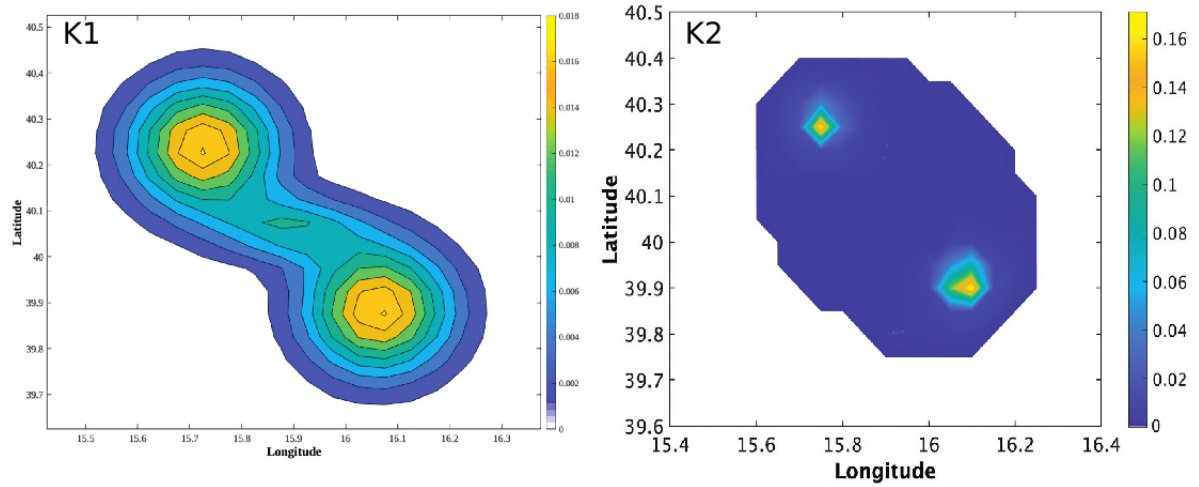


Figure 2.2: Differences in sensitivity areas between the analytic (K1) and time-dependent (K2) kernels (modified from Sketsiou et al., 2020)

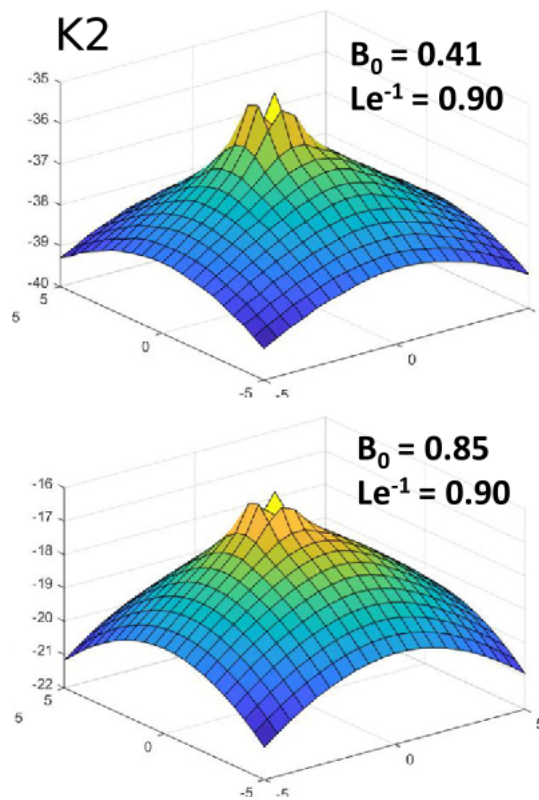


Figure 2.3: Computational kernels (K2) computed for different values of B_0 and Le^{-1} (modified from Akande et al., 2019).

ples. Several applications of the method have been performed at a local scale in continental, volcanic or faulted areas (Calvet et al., 2013; Mayor et al., 2016; Borleanu et al.,

2017; De Siena et al., 2016).

Intrinsic attenuation is strongly dependent on temperature, partial melting, fluid and water content. The results obtained in fault regions show how absorption imaging can mark the profile of fluid-filled fractures networks (Napolitano et al., 2020). Gabrielli et al. (2021) analyzed data of the seismic sequence in Central Italy in 2016-2017 and related high Q_c^{-1} to the deep migration of CO_2 -bearing fluids across the strike of the fault network from a deep source of trapped CO_2 (Fig. 2.4).

At the regional scale, the sensitivity to large scale structures cannot be neglected anymore. Below 3 Hz, crustal reverberations at the regional scale are crucial to model coda attenuation (Morozov and Safarshahi, 2020), especially if the crustal thickness variation is comparable to the wavelength (Cormier and Sanborn, 2019). The diffusive approximation is untested for a shallow Moho and the oceanic crust, which cause energy leakage into the mantle and reverberations (Wegler, 2005; Margerin, 2017). The drastic spatial variations in the deterministic (interfaces) and scattering properties of the sampled media strongly affect coda-wave attenuation measurements. Crustal thickness variations (Sanborn and Cormier, 2018; Cormier and Sanborn, 2019) together with the loss of energy due to leakage into the mantle (Margerin et al., 1999; Wegler, 2005; Margerin, 2017) cause the main bias in the attenuation mapping. Forward modelling is the key answer to correctly model the crustal features allowing a feasible interpretation of high and low coda attenuation at regional epicentral distances. In Chapter 4, I will present the application of coda attenuation imaging across the Italian peninsula and the Tyrrhenian oceanic basin and the results of forward-modelling, which point out the propagation effects dominating the seismogram envelopes.

2.4 Multi-Resolution seismic Attenuation Tomography (MuRAT)

This thesis addresses the imaging of coda waves attenuation using the MuRAT software package. In the framework of seismic attenuation tomography, MuRAT (<https://github.com/LucaDeSiena/MuRAT>) is an open-access code dealing with the separation between scattering and intrinsic attenuation. MuRAT has been developed to image the heterogeneous Earth by providing the tools to measure and map in space total and scattering attenuation and absorption from direct- and coda-waves.

The scattering attenuation is estimated using the peak delay method (De Siena et al.,

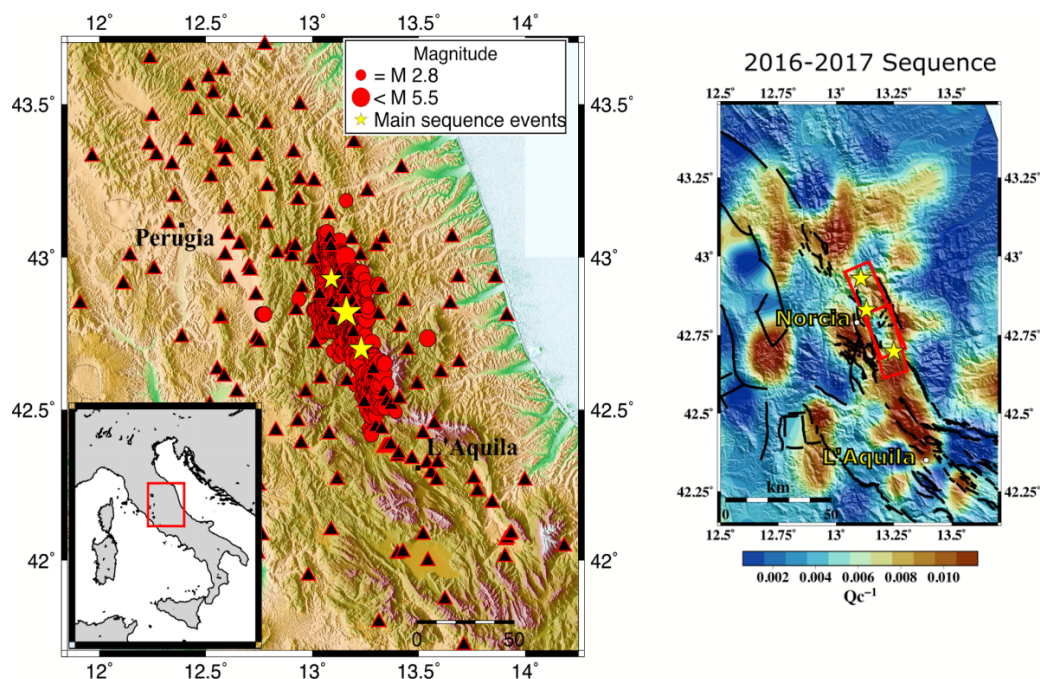


Figure 2.4: Maps of absorption (right panel) across the Central Italy faulted for the seismic sequences of 2016 (left panel) at a central frequency of 1.5Hz (modified from Gabrielli et al., 2021)

2016; Napolitano et al., 2020). While propagating, direct wave packets broaden because of scattering and diffraction. To quantify this elastic attenuation, the method measures the delay between the arrival time of the P or S waves and the maximum energy of the envelope of the direct wave (as introduced in Sec 1.5). The primary assumption of the method is that the wavelength ($\lambda = 2\pi/k$) is smaller than the correlation distance (a), so the condition that has to be verified is $ak \gg 1$, where k is the wavenumber. This assumption is valid for frequencies above 1 Hz, as below that the wavelength becomes comparable to lithospheric scale structures. According to Takahashi et al. (2007), the values for high and low scattering are mapped through a regionalization approach.

MuRAT features the 2D and 3D modelling of coda attenuation using an inversion procedure based on diffusive approximation and sensitivity kernels. The Q_c method measures the decay of the envelope from a given lapse time (Eq. 1.9). MuRAT implements either a linearised approach or a grid search approach to measure Q_c . The linearised approach is proposed first by Aki and Chouet (1975) to fit the exponential decay after taking the logarithm of the energy. The alternative non-linear approach is based on a grid search algorithm that consists in minimizing the residual between the observed

energy (obtained from the waveform envelope at a fixed frequency) and the predicted energy (estimated for a specific Q_c from the exponential law given a pre-defined list of Q_c values) (Napolitano et al., 2020; Sketsiou et al., 2020). As far as the inversion, the code implements either a standard Tikhonov inversion based on singular value decomposition and an iterative conjugate gradient least square inversion minimizing both model norm and Laplacian using the 3D computational kernels devised by Del Pezzo et al. (2018). MuRAT2D uses analytic diffusive kernel functions (Del Pezzo et al., 2016) or the computational lapse-time dependent 2D kernels (Pacheco and Snieder, 2005). Depending on the selected inversion, the code uses the L-curve between residual and norm length or the cost functions to choose the damping parameters. The checkerboard test (Rawlinson and Spakman, 2016) is employed for assessing the robustness of the inversion results.

The last updated version of MuRAT3D has implemented a parallelized code for the non-linear regression and inversion scheme speeding up the computational times.

Q_c has shown high potential as an imaging attribute in volcanic (De Siena et al., 2016, 2017; Gabrielli et al., 2020), fault and regional scales (Napolitano et al., 2020; Sketsiou et al., 2020). Akande et al. (2019) obtained the first 3D kernel-based coda attenuation model using 3D sensitivity kernels and the inversion approach implemented in MuRAT. Using 3D multiple-scattering coda-attenuation kernels, the authors map the Campi Flegrei caldera structure during the unrest. Due to the high sensitivity of Q to heterogeneous structures, fluids and geothermal reservoirs, coda attenuation provides a tool for imaging and understanding the complex crustal features, from a volcanic edifice to a faulted area.

Chapter 3

Modelling by Radiative Transfer

Forward modelling tools allow us to enhance the understanding of structural models of the local and regional Earth structure. Depending on the frequency, the seismic wavefield is sensitive to different scale structures. As frequency increases and wavelengths decrease, the seismic wavefield becomes sensitive to smaller-scale structures such as material heterogeneities. These heterogeneities have a key role in coda generation as they become a source of scattering. Deterministic propagation across interfaces and stochastic processes have been separately modelled in the wave equation solvers and tomography tools. The two approaches can be exploited simultaneously by implementing the description of random media as a velocity perturbation field.

Modelling the small-scale structure with wave equation solvers requires a very fine grid to capture small-size features affecting the short-wavelength wavefield and to solve for the temporal and spatial derivatives. This approach is expensive in terms of computational resources. Radiative transport provides an alternative approach without modelling the wavefield based on the wave equation. It is based on ray theory (not wave dynamics) and handles small-scale (on the order of the wavelength) and large-scale (much longer than the wavelength) structures using different methodologies (Sanborn et al., 2017; Sanborn and Cormier, 2018). In fact, radiative transfer based tools combine the ray-tracing methods to solve ray propagation in 3D velocity models and radiative transport to model scattering process.

3.1 Radiative Transfer Theory (RTT)

As lapse time increases, higher-order multiple scattering will dominate over the single scattering process. Radiative transfer theory is an effective approach for modelling

the effects of multiple scattering and variations of medium heterogeneities on the wave propagation. It can investigate the relation between the statistical treatment of wave propagation through random media and the spatiotemporal variation of mean energy density in the media. The RRT describes the spatial and temporal evolution of wave energy density in random media without considering the interference effect. The RTT ignores the phase information and is used to explain the features of high-frequency coda envelopes, when energy is radiated from a point source in a scattering medium.

Besides seismology, the RTT has been employed for modelling wave propagation in other fields such as atmospheric and planetary frameworks (e.g. for the propagation of light in the atmospheres of planets) (Chandrasekhar, 2013; Mishchenko et al., 2006). Wu (1985) and Wu and Aki (1988b) first applied the RTT to high-frequency seismogram envelopes of local earthquakes to separate the scattering effect and the absorption based on the measured energy density distribution curves. They considered a randomly inhomogeneous medium for an isotropic point source analyzing the case of isotropic scattering assuming both the single scattering and diffusion approximation. Hoshiaba (1991) and Fehler et al. (1992) used the solution of RTT in the case of the multiple isotropic scattering model to develop the multiple lapse time window analysis (MLTWA) for the measurement of intrinsic absorption and scattering loss from S wave energy envelopes. This theory has been extended to the description of energy envelopes of surface waves (Maeda et al., 2003).

Based on RTT, Sato (1994) formulated and investigated the effects of the multiple non-isotropic scattering process given spherically symmetric radiation. However, there is a difference in the non-spherical radiation pattern case for P- and S-waves. Sato et al. (1997) thus built an RTT-based model to describe the multiple isotropic scattering process for a point shear-dislocation source radiation.

Monte Carlo simulations have been developed for synthesizing seismogram envelopes based on RTT models for investigating the complex Earth structures and the effects of the velocity fluctuations on wave propagation (Hoshiaba, 1994; Sens-Schönfelder et al., 2009). The transport of energy in a priori model is simulated through the combination of stochastic and deterministic dynamics. RTT is a powerful means that allows the discrimination of scattering and absorption processes from the overall deterministic processes (i.e., reflection, refraction). RTT has thus been applied for exploring the seismic response of small-scale lithospheric heterogeneities and geologically constraining the structures, such as sedimentary layers (Levander et al., 1994; Pullammanappallil

et al., 1997) and volcanic areas (Gabrielli et al., 2020). Characterizing the small-scale heterogeneities in the upper (highly heterogeneous) 10 km of the Earth is crucial to understand the behaviour of the coda of regional seismic phases.

3.2 Mathematical formulation of RTT

As travel distance increases, the amplitude of the mean wave decreases and incoherent fluctuation waves around the mean wave increase. The interference of incoherent fluctuation waves destroys the phase information. This means that we can better understand the propagation characteristics not from the mean wavefields but from the ensemble average of the energy density of the total wavefields (the *mean energy density*) disregarding phase information.

The RTT equation describes the energy transfer in random media depending on the mean wave energy and the medium heterogeneities spectrum. The rate of energy transfer is averaged over times and volumes large compared with the scales of local fluctuation wavefields (correlation distance a and the typical wavelength λ) around the mean wavefield and small compared with the scales corresponding to significant changes in the mean wave amplitude. The formulation requires a characterization of the random media to take into account the phase and amplitude changes per travel distance based on the dispersion relation of the mean wavefield (Sato et al., 2012).

RTT equation is solved in the case of isotropic and non-isotropic scattering and for isotropic and non-spherical source radiation. Following Sato et al. (2012), this section shows the energy solution for a point source emitting spherical and impulsive radiation. The RTT can be extended to the elastic waves having P- and S- wave modes which are characterized by the propagation velocities α_0 and β_0 , respectively and conversion between P- and S-waves can be implemented into the model. The isotropic scattering is taken into account by scattering coefficients that are isotropic for all scattering modes, i.e., g_0^{PP} , g_0^{PS} , g_0^{SS} , g_0^{SP} . The mathematical formulation describes the processes represented in Figure 3.1, which illustrates the multiple scattering process. P- and S-wave energy densities are expressed as sums of coherent wave energy densities from the source (W_P and W_S in Fig. 3.1). The energy propagation equation is solved using the Green's functions. The energy densities from last scattering points (E_P and E_S) are

expressed in integral form as following

$$\begin{aligned}
E^P(\mathbf{x}, t) &= W^P G^P(\mathbf{x}, t) + \iint \iint_{-\infty}^{\infty} \{E^P(\mathbf{x}', t')\alpha_0 g_0^{PP} + E^S(\mathbf{x}', t')\beta_0 g_0^{SP}\} \\
&\quad G^P(\mathbf{x} - \mathbf{x}', t - t') d\mathbf{x}' dt' \\
E^S(\mathbf{x}, t) &= W^S G^S(\mathbf{x}, t) + \iint \iint_{-\infty}^{\infty} \{E^S(\mathbf{x}', t')\beta_0 g_0^{SS} + E^P(\mathbf{x}', t')\beta_0 g_0^{PS}\} \\
&\quad G^S(\mathbf{x} - \mathbf{x}', t - t') d\mathbf{x}' dt' \\
E(\mathbf{x}, t) &= E^P(\mathbf{x}, t) + E^S(\mathbf{x}, t)
\end{aligned} \tag{3.1}$$

where W^P and W^S are the total radiated P and S energy. The Green's functions for P and S wave energy propagation are given by

$$\begin{aligned}
G^P(\mathbf{x}, t) &= \frac{1}{4\pi r^2 \alpha_0} H(t) \delta\left(t - r/\alpha_0\right) e^{-(\alpha_0 g_0^{PP} + \alpha_0 g_0^{PS} + b)t} \\
G^S(\mathbf{x}, t) &= \frac{1}{4\pi r^2 \beta_0} H(t) \delta\left(t - r/\beta_0\right) e^{-(\beta_0 g_0^{PP} + \beta_0 g_0^{SP} + b)t}
\end{aligned} \tag{3.2}$$

where r is the distance from the source. $H(t)$ and δ are the Heaviside and Dirac function, respectively. The exponential term e^{-bt} common to P and S waves accounts for the intrinsic absorption. These equations can be solved for the energy density distribution as a function of space and time.

In the diffusion approximation, at late lapse time, the equipartition state is reached and the local energy density is stable partitioned $E^S/E^P = \text{const}$. The total energy density equation for the elastic wave in the isotropic scattering model is given by

$$\partial_t E - D \nabla^2 E = (W^P + W^S) \delta(\mathbf{x}) \delta(t) \tag{3.3}$$

whose solution in terms of the total energy density is

$$E(\mathbf{x}, t) = \frac{W^P + W^S}{(4\pi Dt)^{3/2}} H(t) e^{-\frac{r^2}{4Dt}} \tag{3.4}$$

where D is the effective diffusion coefficient accounting for the P and S scattering coefficients

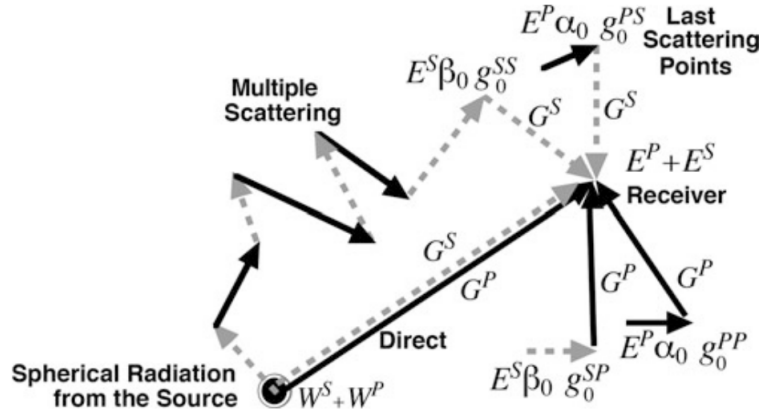


Figure 3.1: Configuration of the multiple scattering process including PS conversions. (figure from Sato et al., 2012)

3.3 Random Media

A statistical model is used to describe the spectral characteristics of heterogeneities causing the scattering process. The statistical characteristics of the media are described by the autocorrelation function (ACF) or power spectral density function (PSDF). To represent the velocity heterogeneities, the wave velocity V is not a constant but a sum of the mean velocity V_0 and the perturbed velocity δV which depends on the location \mathbf{x} as

$$V(\mathbf{x}) = V_0 + \delta V(\mathbf{x}) = V_0[1 + \xi(\mathbf{x})] \quad (3.5)$$

where non-dimensional quantity $\xi(\mathbf{x}) = \delta V(\mathbf{x})/V_0$ is the fractional fluctuation of wave velocity and is a random function of coordinate \mathbf{x} . Considering an ensemble of random media ξ with the same statistical characteristics, the angular brackets $\langle \dots \rangle$ indicates the average over the ensemble, where the mean velocity is chosen so that $V_0 = \langle V(\mathbf{x}) \rangle$ and $\langle \xi(\mathbf{x}) \rangle = 0$.

When the randomness is stationary (homogeneous) overall space, the ensemble average of a product $\xi(\mathbf{x})\xi(\mathbf{y} + \mathbf{x})$ is independent of coordinate \mathbf{y} but a function of lag \mathbf{x} only. To characterize the random media, the ACF of the fractional velocity fluctuation is defined as

$$R(\mathbf{x}) \equiv \langle \xi(\mathbf{x})\xi(\mathbf{y} + \mathbf{x}) \rangle \quad (3.6)$$

which gives a statistical measure of the spatial scale and the magnitude of medium inhomogeneity. If randomness is isotropic, then ACF becomes a function of the lag

distance $r \equiv |\mathbf{x}|$ only. The magnitude of the fractional fluctuation is given by the mean square (MS) fractional fluctuation $\varepsilon^2 \equiv R(0)$. The spatial variation of randomness is well characterized by correlation distance a , as $R \ll \varepsilon^2$ for $r \gg a$.

The Fourier transform of the ACF gives the PSDF as

$$\begin{aligned} P(\mathbf{m}) &= P(m) = \int \int \int_{-\infty}^{\infty} R(\mathbf{x}) e^{-i\mathbf{m}\mathbf{x}} d\mathbf{x} \\ R(\mathbf{x}) &= R(r) = \frac{1}{2\pi^2 r} \int \int \int_{-\infty}^{\infty} P(\mathbf{m}) e^{i\mathbf{m}\mathbf{x}} d\mathbf{m} \end{aligned} \quad (3.7)$$

where \mathbf{x} is the wavenumber vector and $m = |\mathbf{m}|$.

In the numerical study of the wave propagation, it is necessary to make realizations of random media for a given PSDF $P(\mathbf{m})$. Fig. 3.2 shows how different random media (i.e., different power spectra of velocity fluctuations) can be synthesized by changing the PSDF $P(\mathbf{m})$. A random medium sample $\xi(\mathbf{x})$ can be synthesized using $\sqrt{P(\mathbf{m})}$ as the amplitude spectrum and using the Fourier transform as follows

$$\xi(\mathbf{x}) = \frac{1}{(2\pi^2)^3} \int \int \int_{-\infty}^{\infty} \sqrt{P(\mathbf{m})} e^{i\phi(\mathbf{m})} e^{i\mathbf{m}\mathbf{x}} d\mathbf{m} \quad (3.8)$$

where the phase spectrum $\phi(\mathbf{m})$ is chosen to be random between 0 and 2π .

There are several types of ACFs of random media that are convenient to use for studying the wave propagation. Sato et al. (2012) reviewed several types of mathematically tractable ACFs and their PSDFs for homogeneous and isotropic random media:

- Gaussian ACF, given by

$$R(\mathbf{x}) = R(r) = \varepsilon^2 e^{-r^2/a^2} \quad (3.9)$$

and the PSDF is

$$P(\mathbf{m}) = P(m) = \varepsilon^2 \sqrt{\pi^3} a^3 e^{-m^2 a^2/4} \quad (3.10)$$

The Gaussian ACF is used to describe media that are poor in short wavelength components since the PSDF goes rapidly to zero for large m .

- Exponential ACF, given by

$$R(\mathbf{x}) = R(r) = \varepsilon^2 e^{-r/a} \quad (3.11)$$

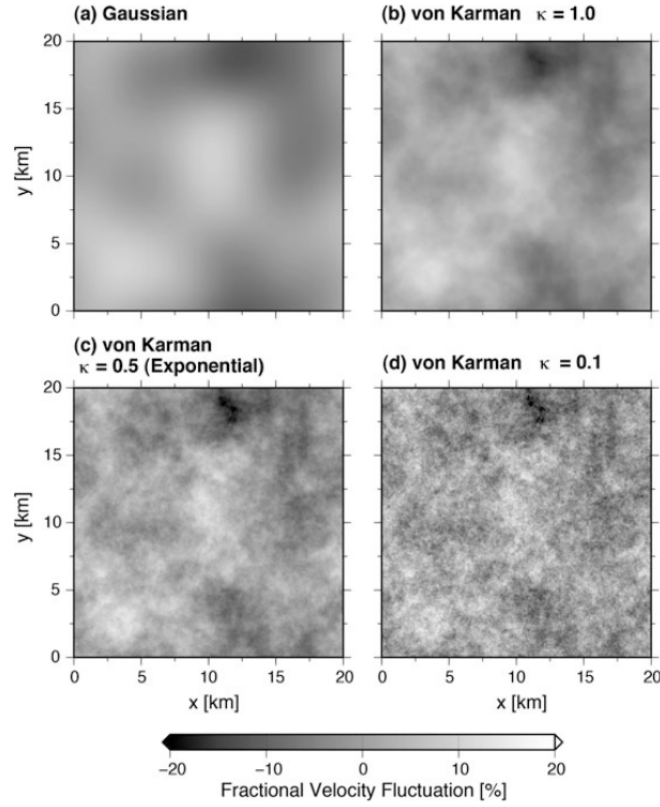


Figure 3.2: Density plots of 2-D random medium samples, where $a = 5\text{km}$ and $\varepsilon = 0.05$. (a) Gaussian ACF. (b) – (d) von Kármán type ACFs with different k -values

For the 3-D case, the PSDF is

$$P(\mathbf{m}) = P(m) = \frac{8\pi\varepsilon^2 a^3}{(1 + a^2 m^2)^2} \quad (3.12)$$

The PSDF obeys a power law for large wavenumbers.

- von Kármán ACF, given by

$$R(\mathbf{x}) = R(r) = \frac{\varepsilon^2 2^{1-k}}{\Gamma(k)} \left(\frac{r}{a}\right)^k K_k\left(\frac{r}{a}\right) \quad (3.13)$$

for $k = 0 - 1$. $\Gamma(k)$ is the gamma function and K is the modified Bessel function of the second kind of order k . The PSDF is

$$P(\mathbf{m}) = P(m) = \frac{8\pi^{3/2}\Gamma(k + 3/2)\varepsilon^2 a^3}{\Gamma(k)(1 + a^2 m^2)^{k+3/2}} \quad (3.14)$$

The PSDF obeys a power law for large wavenumbers ($am \gg 1$). A power-law decay for large wavenumbers means that the PSDF for Von Kármán type random media is rich in short wavelength components compared to that of Gaussian type random media. Its ACF is more appropriate for describing random velocity inhomogeneities of the real Earth medium compared to a Gaussian type because of its power-law characteristic.

3.4 Radiative3D

As mentioned above, the radiative transfer theory describes the spatiotemporal variation of wave energy density in random media without considering the interference effect. The energy propagation can be simulated by shooting many particles from a source; then, each particle propagates carrying unit energy which interacts with heterogeneities distributed across the uniform background characterized by velocity V_0 . The transport of energy in the model is simulated by a combination of stochastic and deterministic dynamics. The simulation is performed via Monte Carlo technique, which treats source radiation, propagation distance and scattering as stochastic processes for the propagation of particles.

An open-access code dealing with radiative transfer simulations is Radiative3D (<https://rainbow.phys.uconn.edu/geowiki/Radiative3D>). Sanborn (2017) designed this code addressing the RTT-based simulations of synthetic seismic energy envelopes at seismometers located across the Earth in three-dimensional models. The simulation is done for a single frequency and monochromatic elastic energy is released from a source at a fixed location and time and it propagates as a discrete packet (*phonon*). The computational advantage of radiative transfer is that the model meshes describe only the large-scale background medium, while the small-scale heterogeneities are described by statistical parameters without explicitly defining a perturbation field. The phonon's path through the model is thus determined via a combination of ray theory to handle the deterministic propagation across the large scale structure and scattering theory, which is the stochastic handling of scattering due to small-scale heterogeneities. Scattering events are due to perturbations in the large-scale background structure which affect the particle's deterministic path. Figure 3.3 show a simplified sketch of the source (earthquake or explosion), the phonon propagation across interfaces and scattering events. With a sufficient number of phonons emitted from the source event,

a picture of the energy transport throughout the model can be retrieved. In the following sections, details on the code implementation are summarized according to the main reference (Sanborn, 2017).

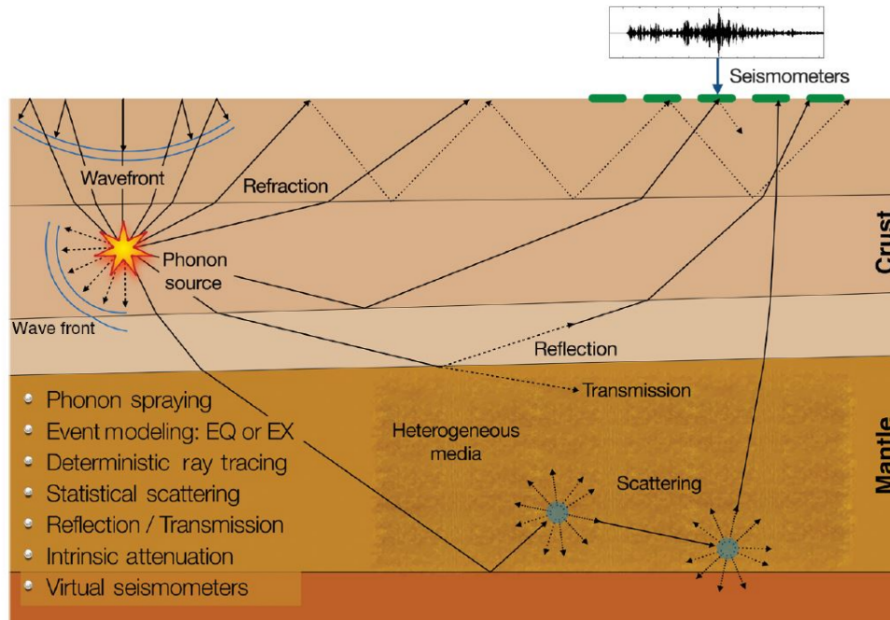


Figure 3.3: Propagation of discrete packets of elastic energy computed by the radiative transfer algorithm (from Cormier and Sanborn, 2019).

3.4.1 Deterministic propagation

Ray theory deals with elastic wave problems considering rays rather than wave dynamics. This approach is more accurate when the ratio of the wavelength of the wavefield to the scale length of the medium where it propagates approaches zero. The energy flux and so the wave amplitude is defined at each point in the wavefield following the wavefront. The rays define the paths of energy particles through the medium and, knowing their velocity, allows the tracking of the energy transport as a function of time. Besides, as P and S waves have distinct phases and group velocities, phonons for P and S wave modes can be treated as distinct particles with independent ray trajectories.

The implemented models are composed of adjoining volumetric cells in which a single set of parameters characterizes the media to determine paths within the cell. If phonons travelling from one cell to another cell encounter a discontinuity in materials physical parameters, reflection, refraction, diffraction, and conversions between P and

S polarization modes are modelled in the simulations. The developers treated these effects by employing the ray theory formalism from Červený (2001). The amplitude of ground motion is thus computed at an interface for a ray of known amplitude and polarization interacting with the interface at a particular time and location. The computation takes into account the effects of both the incident and product rays resulting from reflection/transmission at the interface. The code tracks the trajectories of phonons assumed to carry discrete quantities of energy through the hypothesized Earth models. The receivers collect phonons in the “gather area” (i.e., the area with a certain radius around the receiver) interacting with the interface close to the receivers. The results of the simulation are displacement amplitudes obtained from the energy carried by phonons.

3.4.2 Stochastic propagation

RADIATIVE3D implements elastic scattering modelling via radiative transport approach following Shearer and Earle (2004). A scattering event is considered as an interruption of the deterministic trajectory of phonons, which are radiated from the scattering point with a deflected propagation direction. The scattering could also generate and re-emit a different polarization mode (e.g., P/S conversion). The new direction and mode are chosen randomly based on the scattering coefficients, which are derived in terms of the statistical characterization of the heterogeneity spectrum of the medium, based on the Born approximation (Sato et al., 2012). The Von Kármán type PSDF (Eq. 3.14) is adopted to describe the heterogeneity spectrum giving the dependency between the heterogeneity strength and wavenumber and can be computed as the Fourier transform of the ACF of small-scale velocities and density heterogeneity. The scattering coefficients are computed as products of functions describing the scattered radiation patterns and the PSDF, which controls the amplitude in the outgoing wavenumbers and can favour forward over backward scattering. The average of the scattering coefficients overall deflection angles provides the scattering probability per unit length and the mean-free-path (i.e., the average propagation distance between scattering events) can be computed.

The effect of intrinsic attenuation is to reduce the amount of energy in each phonon as a function of time, but it does not reduce the number of phonons reaching the target. As the phonon’s paths include conversions between P and S modes, the effects of intrinsic attenuation in the time evolution of energy particles is taken into account by constructing an attenuation operator that couples intrinsic attenuation with scattering-conversion not only considering the attenuation coefficients Q_P^{-1} and Q_S^{-1} .

3.4.3 Simulation parameters and set up

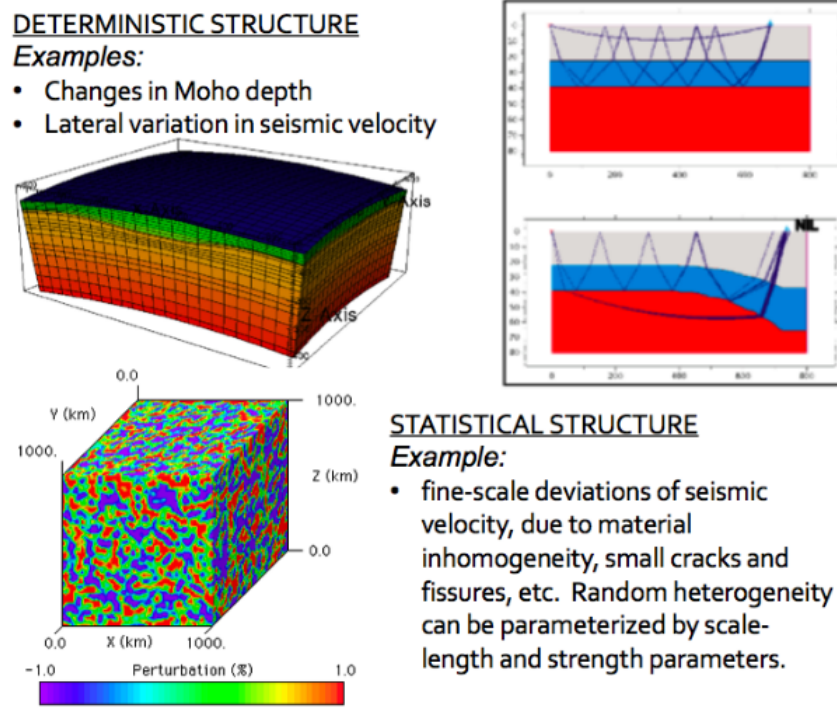


Figure 3.4: Examples of large-scale heterogeneity (deterministic structure) and its effects on S and Lg waves propagation (upper panel). Example of configuration of 3D small-scale heterogeneity (statistical structure) (after Sanborn, 2017)

As shown in Fig. 3.4, Earth model is composed of a large-scale deterministic structure, consisting of discontinuities separating layers, and a perturbed statistical structure described by a heterogeneity spectrum, which influences the stochastic dynamics. The material properties that can be used to describe the slowly-varying background elastic properties of the medium are the seismic wave velocities (for P and S waves), density, and intrinsic attenuation quality factors (Q_P , Q_S). The parameters describing the heterogeneity spectrum (a von Karman spectrum) of small velocity perturbations controlling the scattering process are fractional fluctuation size ε , correlation distance a , a decay rate factor k called the Hurst parameter and proportionality factor ν between density and velocity fluctuation. The background ratio of P and S velocities is locally uniform and the fractional fluctuation of P and S velocities are equal. The code can model ray paths in media characterized by the gradient in physical properties. Earth layers can be implemented with linear gradients of density, P and S waves velocity. The remaining properties are treated as uniform throughout the layer. These properties are all uniform

throughout the layer cells and are discontinuous across cell boundaries. Besides, the interfaces can have arbitrary orientation allowing to reproduce lateral variation in layer thickness. If the seismic wave velocities are spatially varying, the ray paths are not governed only by reflection and refractions across the boundaries but become curves. The RADIATIVE3D code builds on previous ray-tracing code (Menke, 2005) to model the phonons trajectory, which results in a series of arc segments recomputed at each cell boundary or at scattering points.

The advantage of RADIATIVE3D is to handle sharp contrasts of physical properties at the interfaces with the radiative transfer approach. It allows the modelling of the effects of lateral variations in crustal thickness and sedimentary thickness (the 3D medium is azimuthally symmetric) on the wavefield envelope. Figure 3.5 shows how different crustal structures can be implemented by the software to take into account crustal pinches, sediments or water and lateral varying heterogeneities.

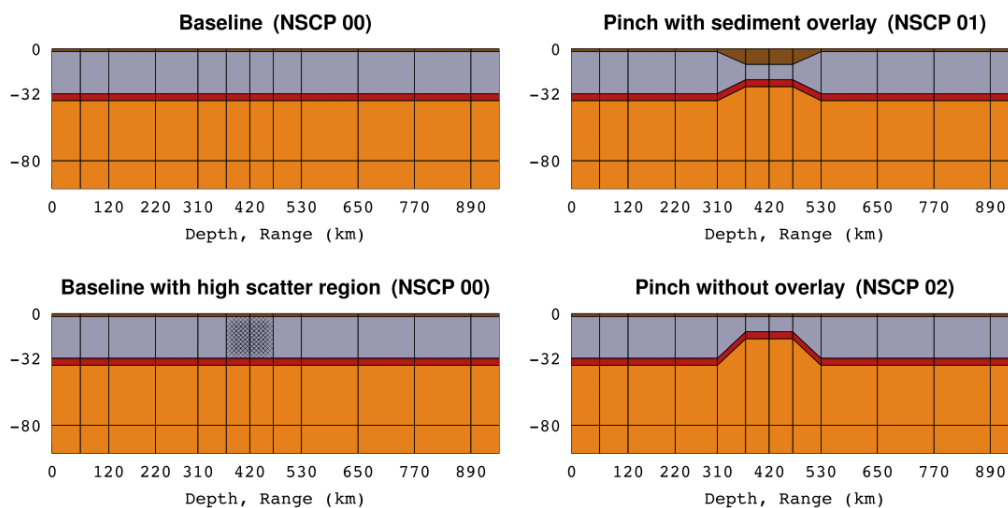


Figure 3.5: Examples of Earth discontinuities implemented in RADIATIVE3D (after Sanborn and Cormier, 2018).

Chapter 4

Seismic attenuation modelling across Italy and the Tyrrhenian basin

4.1 Introduction to regional scale attenuation

The attenuation of coda waves (Q_c^{-1}) has become an additional imaging attribute in the last two decades (Romanowicz and Mitchell, 2007; Calvet et al., 2013; Borleanu et al., 2017). As introduced in Chapter 1, "coda waves" are wave-trains following a crustal phase, like a direct-S wave (Calvet et al., 2013) or Lg wave, generated and multiply-reflected inside the crust (Campillo et al., 1985; Sens-Schönfelder et al., 2009). The coda of Lg-waves has been modelled and employed for mapping in a larger number of studies due to its sensitivity to well-constrained crustal depths and the abundance in recordings at regional and global scales (Xie and Mitchell, 1990; De Souza and Mitchell, 1998; Mitchel et al., 1998; Mitchell et al., 2008, 2015). These works rely on the single scattering approximation and assume the coda sensitivity to a scattering ellipsoid (Sato et al., 2012). In the last decade, shear-wave attenuation imaging studies have started to use a multiple-scattering and/or diffusive approximation (Calvet et al., 2013; Borleanu et al., 2017). At the local scale, at frequencies above 1 Hz, and especially in volcanoes, the diffusive approximation has been justified by the high heterogeneity of media that rapidly disperse coherent information enhancing coda (Wegler and Lühr, 2001). Below 3 Hz, the size of velocity heterogeneities becomes comparable with seismic wavelength λ , leading to a transition from a small-scattering far-field to a resonant scattering regime (Cormier and Sanborn, 2019). In this case, coda waves primarily consist of strong reverberations (dominated by higher mode and fundamental mode surface waves) and scattering due to larger-scale structures (Gabrielli et al., 2020). At the regional scale,

these reverberations are recognized as crucial to model coda envelopes effectively at $\sim 1\text{Hz}$ (Morozov and Safarshahi, 2020). Recognizing the effect of crustal and near-surface layering on coda waves is important to understand the validity of models of coda generation alternative to those grounded on S-wave Q and uniformly-distributed random, small-scale heterogeneity, independent of frequency. According to the standard description of coda waves, the redistribution of energy in the tail of crustal phases is a manifestation of multiple scattering (Sato et al., 2012) that a diffusion equation can model at late lapse times (Aki and Chouet, 1975). If late-lapse-time Q_c^{-1} provides a direct measurement of energy absorption (Calvet et al., 2013), the results of Cormier and Sanborn (2019) suggest that these techniques could be applied in oceanic settings.

Diffusive kernels based on radiative transfer theory and representing the sensitivity of body-wave phases to crustal structures have been introduced by different researchers in the last decade (Obermann et al., 2013; Mayor et al., 2014; Margerin et al., 2016; Del Pezzo et al., 2016, 2018). The kernels adopt the Paasschens (1997)'s approximation of the energy transport equation in the single-layer hypothesis of Pacheco and Snieder (2005). Most recent applications focus on local volcanic and faulted media at frequencies above 1 Hz (Obermann et al., 2013; Prudencio et al., 2013a,b; De Siena et al., 2017; Prudencio et al., 2018; Gabrielli et al., 2020; Sketsiou et al., 2020; Napolitano et al., 2020). Mayor et al. (2016) provide the first application of kernel-based coda attenuation imaging at a regional scale (the Alps and Northern Apennines). They employ a regionalization approach for mapping absorption anomalies with the kernels devised by Mayor et al. (2014). The application is made possible by the short source-station distances and the thick Moho, which avoids the sharp contrasts of scattering properties enhancing Lg waves (Sens-Schönfelder et al., 2009). A framework for the inversion of kernel-based coda-wave attenuation in volcanic media has been developed by De Siena et al. (2017) (as discussed in Chapter 2 - MuRAT). This inversion scheme assumes that seismic energy propagates only within the boundaries of the inversion grid: this is generally the case for diffusive kernels as the energy remains concentrated near the source and station (Obermann et al., 2013; Mayor et al., 2014; Del Pezzo et al., 2016). In this case, energy can be normalized in space to obtain spatially-dependent attenuation values from source-station measurements. However, De Siena et al. (2017) applied the procedure to a small-scale volcanic area of about 10 km lateral extension. Ogiso (2019) and Shito et al. (2020) extended the use of diffusive kernels to depth-dependent regional media (lateral extension of the order of 500 km) in southwestern Japan. This inver-

sion procedure provides a forward model to image scattering and absorption, allowing resolution tests.

The effect of crustal pinching (Sanborn et al., 2017; Sanborn and Cormier, 2018) and loss of energy due to leakage into the mantle (Margerin et al., 1999; Wegler, 2005; Margerin, 2017) contrasts the hypothesis that coda attenuation is a simple superposition of scattering and absorption, especially at frequencies around 1Hz. Therefore, one important issue is the validity of diffusive kernels to model the propagation of Lg coda waves at the regional scale under the ocean. If we cannot rely on kernels, there is still the possibility that diffusive coda attenuation mapping could highlight where the strongest reverberations occur. In areas where data sensitivity is sufficient, kernel-based imaging could mark the location of either high-scattering materials or regions of anomalous Moho variations.

Both the deterministic and stochastic characteristics of multiple scattering in a thick crust can be modelled using radiative transfer theory (Sens-Schönfelder et al., 2009). The RADIATIVE3D code is employed to model coherent and stochastic energy envelopes induced by deterministic large-scale structure and small-scale heterogeneities. This code represents the ideal forward modelling tool for the Lg waves, especially across the oceanic basins or in the areas where scattering characteristics change rapidly in space, at least if sufficient information on seismic interfaces is available. The efficient estimation of deterministic effects on coda wavefields recorded at the regional scale appears urgent given the above-mentioned debate on the true origin of coda waves, and now that the coda of noise cross-correlations are also used for Q_c imaging (Soergel et al., 2020).

The Tyrrhenian Sea is ideally suited to understand the limitation of diffusive approximations in the presence of crustal reverberations, crustal pinches, and volcanic materials. Several high-resolution Moho maps exist (Di Stefano et al., 2011; Manu-Marfo et al., 2019) and a study regarding the efficiency of the crustal and uppermost mantle shear waves (Lg and Sn) was carried out by Mele et al. (1997) in this region at low frequencies. These authors found inefficient Sn propagation for paths across the southern Tyrrhenian Sea. They interpreted observations as due to asthenospheric material in the uppermost mantle, likely related to volcanic activity and high heat flow. Lg blockage was particularly relevant off the coast of Calabria and under the Apennine mountain belt.

In this chapter, the data analysis of seismic attenuation and the envelope forward

modelling is presented to discuss the effect of lateral variations of crustal structure (variations in crustal thickness, crustal reverberations, multiple scattering and absorption) on coda attenuation in the Tyrrhenian basin. The procedure and the results presented in this chapter have been published in *Physics of the Earth and Planetary Interior* in 2021 (Nardoni et al., 2021).

4.2 Data and Methods

4.2.1 Data selection and processing

After the deconvolution of the instrument response, we analyze velocity waveform data recorded by permanent and temporary broadband seismic stations in Italy and Corsica (Fig. 4.1). The stations belong to the permanent seismic networks operated by the Istituto Nazionale di Geofisica e Vulcanologia (INGV) and the Réseau sismologique et géodésique français (RESIF, 3 stations in Corsica) and to a 10-receivers temporary seismic network, LiSard (whose acronym stands for “lithosphere of Sardinia”), which operated from July 2016 to November 2018. To achieve the best coverage across the Tyrrhenian Sea, we select 50 crustal earthquakes of magnitude (M_w) ranging from 4 to 6, that occurred between 2010 and 2018 and were recorded at approximately 270 stations. Only events with a high magnitude (> 4) are considered to exclude a low signal-to-noise ratio for data recorded across the Tyrrhenian Sea. The location of epicenters, magnitude, and origin time of earthquakes have been determined by the INGV (<http://cnt.rm.ingv.it/>). The high-magnitude events occurred mainly in the high-seismic area of Central Italy and are detected with a good signal-to-noise ratio at the stations that are located in Sardinia and Sicily, allowing a good coverage of the basin.

The initial dataset was then processed based on other criteria. The epicentral distances range from 400 km up to almost 800 km to consider only regional distances. Most of the data are characterized by focal depths in the range of 1 to 20 km to select only crustal seismic sources. The final dataset consists of around 700 waveforms and the heterogeneous ray density is shown in Fig. 4.1. We then computed the spectrograms to determine the main frequency content of the seismograms. As an example, Fig. 4.2 represents the spectrogram of a high-magnitude earthquake that was recorded in Sicily and shows that the main signal contribution is around 1 Hz at this scale. We thus filter the seismograms in the frequency band 0.5-1.5 Hz applying a fourth-order Butterworth

band-pass filter.

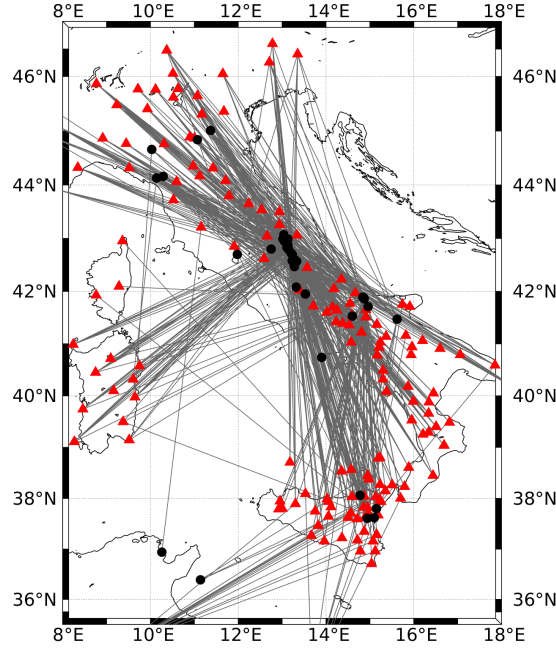


Figure 4.1: Data coverage represented by grey segments connecting sources (black circles) and stations (red triangles).

4.2.2 Coda attenuation measurements

Coda attenuation is measured using the inverse of the coda quality factor (Q_c^{-1}). The energy envelope of seismic coda waves in the standard description decays as (see Chapter 1):

$$E(t, f) = S(f)t^{-\alpha}e^{-2\pi ft/Q_c(f)} \quad (4.1)$$

where E is the energy density, $S(f)$ is a frequency-dependent source and/or site term, t is the lapse time, f is the central frequency, and Q_c is dependent on frequency. The factor α is a fixed exponent and depends on the physical model used to describe coda waves. At low frequencies and in the single scattering regime, $\alpha = 2$ (Sato et al., 2012) and the coda quality factor depends on scattering and absorption: $Q_c^{-1} = Q_{sc}^{-1} + Q_i^{-1}$, where sc and i stand respectively for scattering and intrinsic contributions. At long lapse times and sufficiently high frequency, coda waves are ideally composed of multiple-scattered waves and, over a certain lapse time, coda waves can be forward modelled by

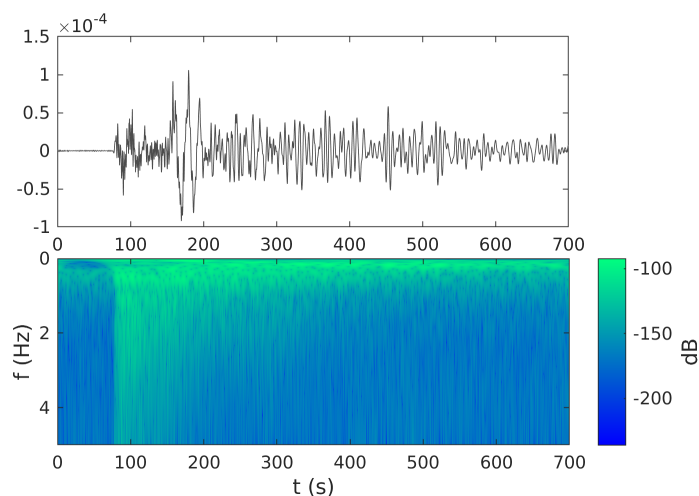


Figure 4.2: (upper panel) Vertical component of the earthquake occurred in Central Italy (named Event A) and recorded by a receiver located in Sicily. (bottom panel) S-transform applied to the seismogram shown above. The values of the colorbar are dB.

a diffusion process (Aki and Chouet, 1975). In this assumption, $\alpha = 3/2$ and Q_c is a measurement of seismic absorption Q_i (see Sato et al., 2012, Chapter 3, Section 3.1.3). Q_c^{-1} values are estimated from Eq. 4.1 performing a linear regression in a coda time window which, as shown by Calvet and Margerin (2013), should not be affected by any transient (coherent) wave packet.

4.2.2.1 Q_c Lapse Time Dependence

Calvet and Margerin (2013) state the importance of taking into account the same range of epicentral distances and of adopting the same coda onset time (t_w) for all data to avoid the mixing of early and late coda windows. Different coda onsets are thus explored without limiting the selected distance range. The choice $t_w = 2t_S$ (t_S is the arrival time of S-waves), a standard threshold for coda attenuation measurements, requires onsets greater than 200 s due to both the average epicentral distance and S-wave velocity. Based on this information, we selected two different coda onsets t_w , i.e. 220 s and 270 s, setting the coda window length L_w to 100 s and 90 s, respectively. The first choice is more conservative in terms of signal-to-noise ratio and source-station coverage, while the second is more suitable to represent coda waves in the diffusive regime. To compare the tomographic results, we estimate the value of Q_c^{-1} in the two coda windows selected by performing a standard least-squares linear fit of the logarithm of $E(t, f)t^{1.5}$ (see Eq.4.1) on the envelope obtained from the Hilbert transform. Values of Q_c are accepted

if the correlation coefficient of the linear regression is greater than 0.6 (Calvet et al., 2013) to avoid coherent waves arrival (Fig. 4.3).

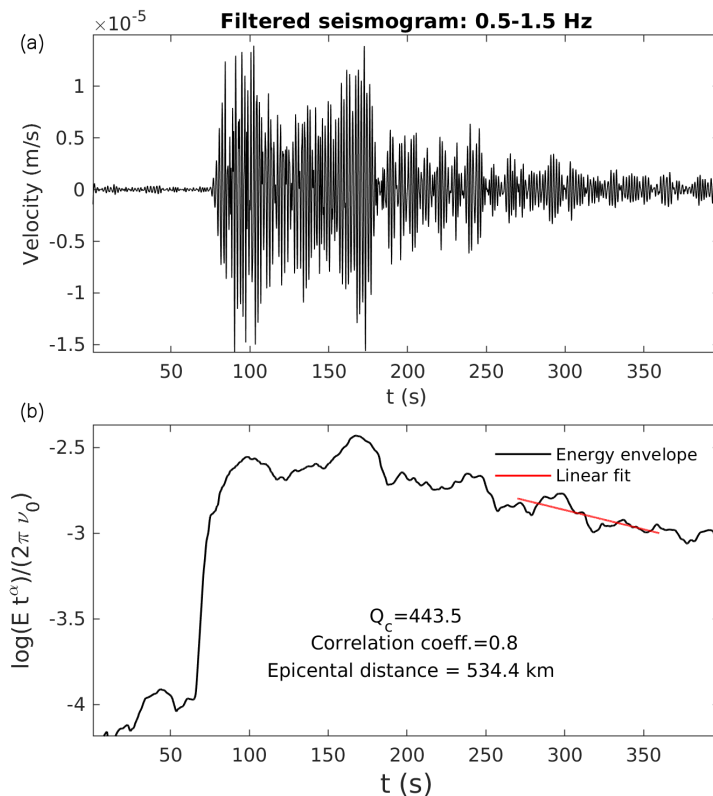


Figure 4.3: (a) Filtering of the seismogram, shown in Fig. 4.2, in the frequency band 0.5-1.5 Hz. (b) Envelope (black line) of the filtered vertical component, shown in panel (a), and linear regression performed in the time window 270-360 s (red line).

In Fig. 4.4, we plotted Q_c as a function of the epicentral distance for the two cases mentioned above to test our assumption of seismic diffusion in the selected window. Calvet and Margerin (2013) show that we can define the ideal coda window if Q_c^{-1} is constant with epicentral distance. In that case, multiple scattering is approaching the diffusive regime. Coherent and reverberating waves in the crust will act against diffusion. All the plots computed for different values of t_w as well as the visual inspection of seismograms show that there is no clear decreasing or increasing trend relative to the epicentral distance associated with wave transients after 200 s. We apply a fit using the normal function to Q_c^{-1} distribution for each coda onset to evaluate the mean value and the standard deviation (Fig. 4.4) and the outliers threshold ($Q_c^{-1} > 5 \cdot 10^{-3}$).

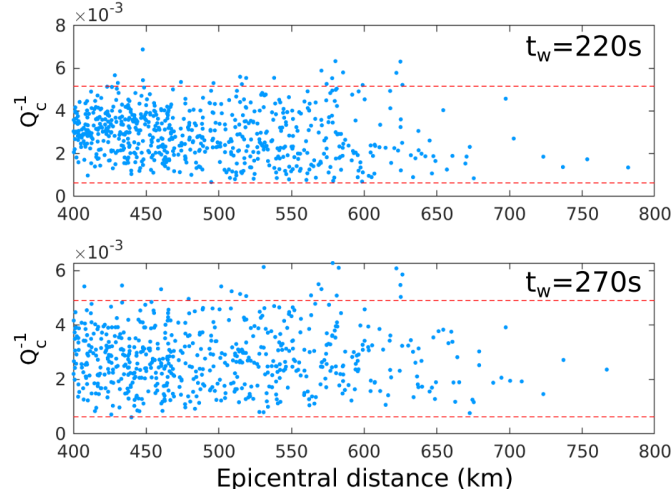


Figure 4.4: Q_c^{-1} obtained at 1 Hz is plotted as a function of the epicentral distance. The lapse times and lengths of the coda windows are $t_w = 220s$ and $L_w = 100s$ (upper panel); $t_w = 270s$ and $L_w = 80s$ (bottom panel). The red dashed lines correspond to the mean values $Q_c^{-1} \pm \sigma$ (σ is the standard deviation).

4.2.3 Inversion for coda attenuation

The measurements carried out in the previous section were aimed at testing if we could model scattering at the chosen lapse time and window length with a diffusive approximation. If energy remains in a single-scattering crustal layer, we can then set up the inversion scheme devised by De Siena et al. (2017) to obtain spatially-dependent coda attenuation using 2D source-station sensitivity kernels (Mayor et al., 2014; Del Pezzo et al., 2016; Ogiso, 2019) for each source and receiver pair. The kernels allow us to map the effective sensitivity of the Q_c parameters in space and build the rows of the inversion matrix. The first kernels used (K1) are those proposed by (Eq. 2.5 - Del Pezzo et al., 2016). Their primary limitation is that they are computed via a Monte Carlo numerical simulation of the energy transport theory equation in a diffusive highly-heterogeneous medium at the local scale, for the first 15 seconds of the seismogram. Sketsiou et al. (2020) compare these kernels and lapse-time dependent computational kernels devised for diffusive media (Paasschens, 1997; Pacheco and Snieder, 2005; Obermann et al., 2013; Mayor et al., 2016; Del Pezzo et al., 2018; Ogiso, 2019), finding little differences in applications at the regional scale. While the K1s dramatically reduce computation times during the forward step of the tomographic procedure, computational lapse-time dependent kernels (K2) (Pacheco and Snieder, 2005) are more appropriate to model the

spatial sensitivity in a multiple scattering regime. As other studies have demonstrated (Fig. 2.2), both K1 and K2 show the highest sensitivity in source and receiver positions. However, the K2 sensitivity is reduced along the segment between sources and stations. Due to the absence of stations and sources across the basin in our study (Fig. 4.1), these kernels will lead to a loss of source-station sensitivity in the Southern Tyrrhenian Basin as shown in Fig. 4.5.

The inversion strategy normalizes the energy density across the inversion grid, assuming that no energy has left the grid through its deep and lateral boundaries (De Siena et al., 2017). While this approximation is proven to stand for the lateral boundaries when using sensitivity kernels (Sketsiou et al., 2020), this is not the case for shallow Moho under oceans, causing reverberations and leakage that trade-off with scattering and absorption.

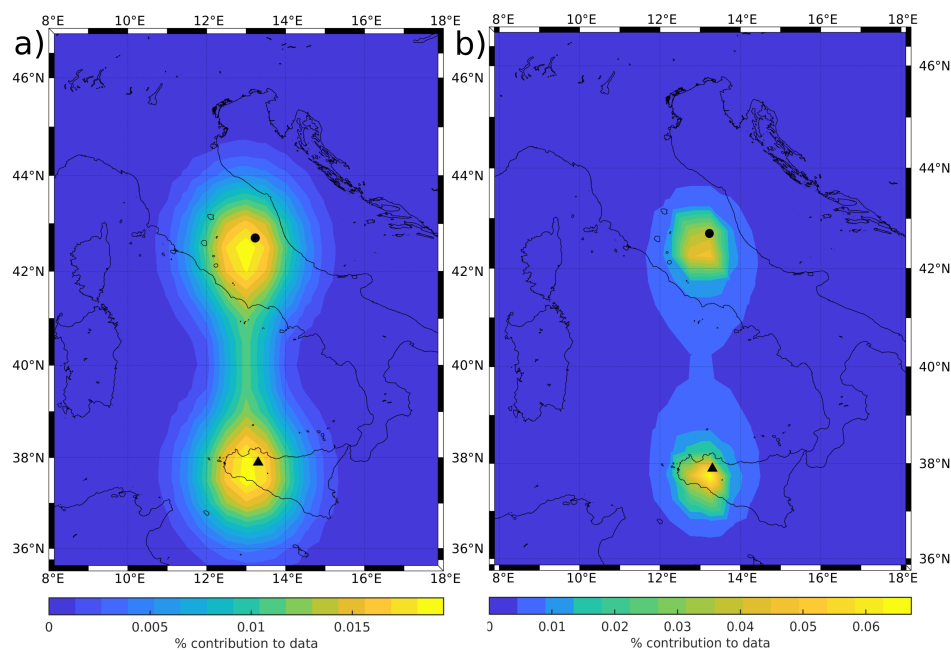


Figure 4.5: Contribution of each node to the coda quality factor measurement for a single source-receiver pair: comparison between (a) analytic and (b) computational kernels.

We used a first-order Tikhonov inversion, employing both the analytic K1 and computational K2 kernels for the construction of the inversion matrix (De Siena et al., 2017; Sketsiou et al., 2020) and parameterized the area with a grid spacing of 0.5° in both

latitude and longitude to invert for the spatial distribution of Q_c^{-1} . We use the inversion not just as a benchmark for resolution but also to understand if the forward model and kernels we propose are physically acceptable.

The inversion problems have data vectors of 680 elements for the coda window 220-320 s and 620 elements for 270-360 s. The rows of the inversion matrices G (680 by 504 and 620 by 504, respectively) are the normalized kernels (De Siena et al., 2017) used to solve, overall, 504 model parameters. The inversion problems are ill-posed and over-determined only in the parts of the grid sampled by sufficient sources and stations (Fig. 4.1). The L-curve has been computed (Fig. 4.6) to select a proper damping parameter for the Tikhonov regularization (as explained in Sec 2.1). At 1 Hz, the same damping parameter (i.e. 0.13) has been selected for both coda windows to obtain a map of the spatial variations of coda attenuation. We evaluate its resolution by performing a checkerboard test with cell dimension 4 times the node spacing ($2^\circ \times 2^\circ$ - Fig. 4.7 and 4.8).

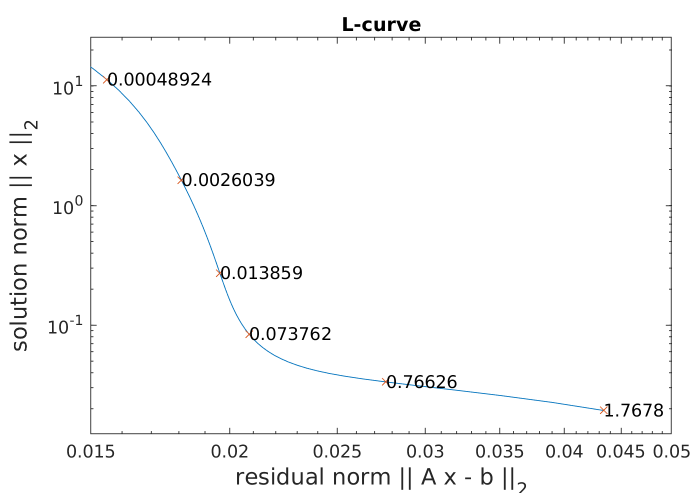


Figure 4.6: L-curve corresponding to the inversion for the onset at $t_w = 270s$. The damping factor is set at 0.13 for both coda windows.

4.3 Results

4.3.1 Coda-attenuation mapping

The inversion results for both coda windows, 220-320 s and 270-360 s, are shown in Figure 4.9. Figure 4.9a, corresponding to the window 220-320 s, consistently shows

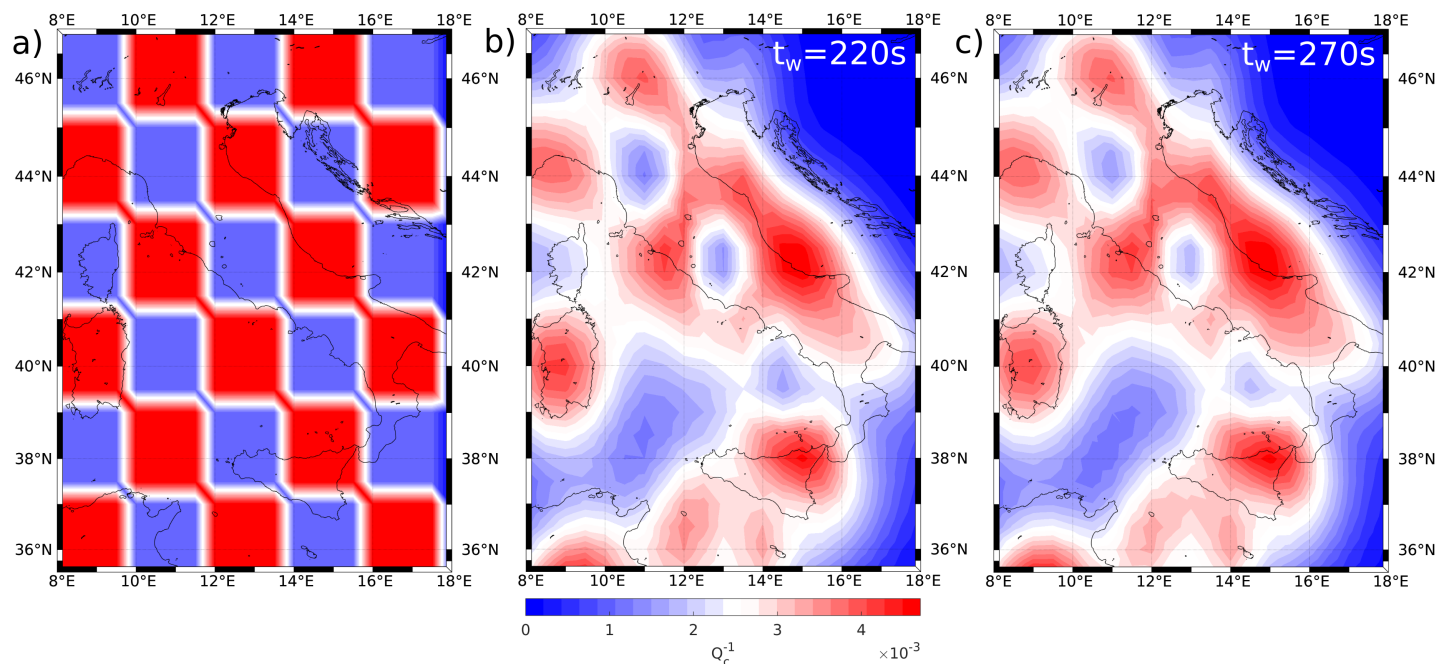


Figure 4.7: (a) Input and outputs of the checkerboard test for the onsets $t_w=220s$ (b) and $t_w=270s$ (c).

the highest attenuation across the continental regions. The resolution test (Figure 4.7) allows the interpretation of high-attenuation zones across the peninsula and the Northern Tyrrhenian Sea and low-attenuation areas across Tuscany and the southern basin. Extending south from $\sim 41^\circ$ latitude and $\sim 13^\circ$ longitude until 38° latitude, across the Tyrrhenian Sea, we observe the most intense low-attenuation anomaly (negative Q_c down to -0.004). The negative attenuation anomaly in the southern part of the basin is obtained using positive data and different damping parameters in the inversion procedure. The hit count, generally in tomographic imaging when using coda (Soergel et al., 2020), ensures that this is a well-covered area (Fig. 4.1). Profile AA' taken at the centre of this NS low-attenuation anomaly crosses the shallowest Moho depths modelled by Manu-Marfo et al. (2019) across the Tyrrhenian Sea. Negative Q_c anomalies in this region could then be interpreted as a marker of the breakdown of the diffusive regime (Margerin, 2017). In practice, the assumption on which we build the kernels is invalid in the case of energy leakage and crustal thinning. The existence of zones of negative Q_c in the final tomographic maps obtained using positive high-quality data can thus be a marker of both insufficient coverage and improper forward model. The results can

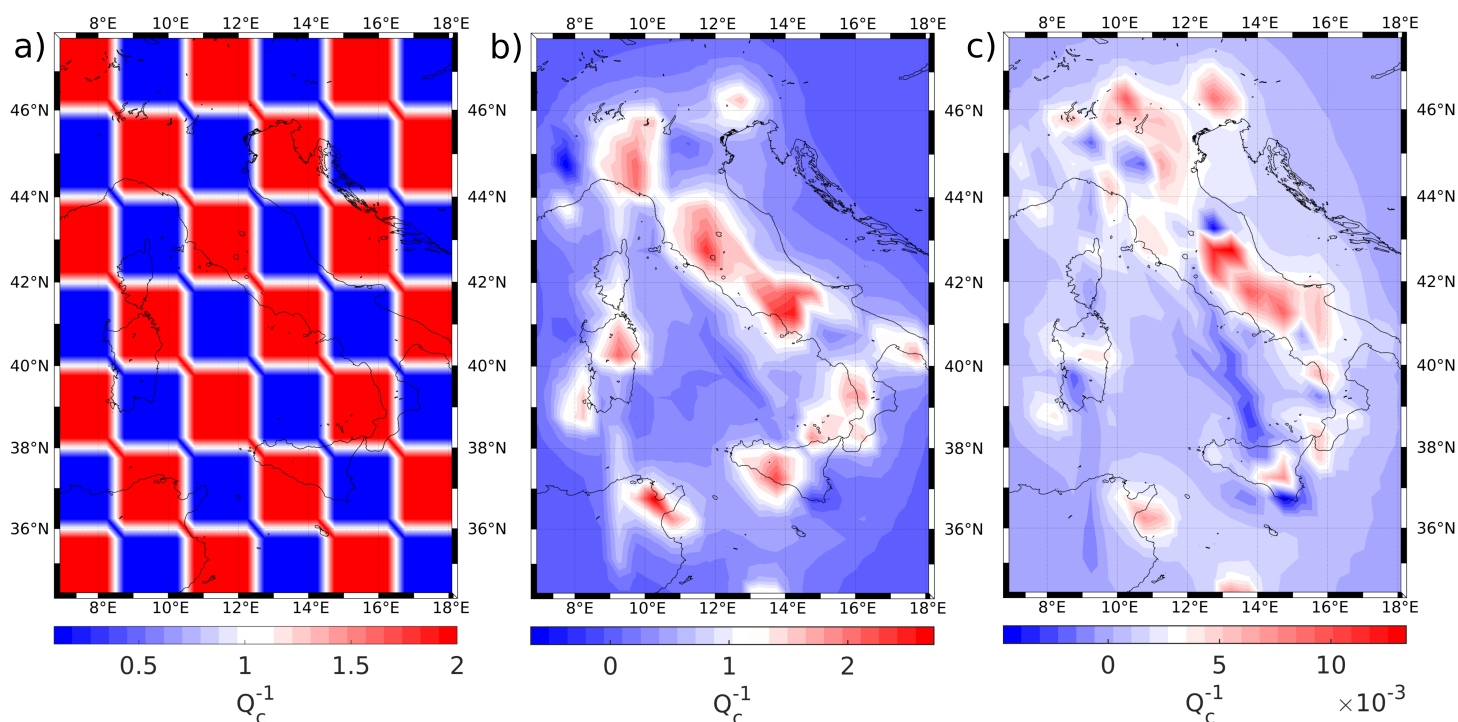


Figure 4.8: (a) and (b) are the input and output of the checkerboard test, respectively; (c) is obtained by inverting the real data. Both panels (b) and (c) are obtained using K2 kernels in the coda window 270-360 s. Panel (b) shows that the resolution is very low compared to the resolution obtained with kernel K1 (Fig. 4.7c).

mark areas of energy leakage and crustal reverberations, benchmarked by geological and geophysical observations.

The second choice of coda window (270-360 s) better fits the diffusive assumption at the expense of the signal-to-noise ratio. In this case, we had to restrict the coda duration to $L_w = 90s$ to avoid modelling noise. Fig. 4.9b shows the inversion results with the same damping factor defined for the previous onset (0.13). The comparison between these two maps in Figure 4.9 shows consistent attenuation anomalies along the peninsula. While the negative Q_c anomalies are strongly dampened, their signature persists across profile AA' in the Southern Tyrrhenian basin.

Fig. 4.8c shows the results obtained for the second coda window using K2 kernels. As expected from the sensitivity (Fig. 3), the resolution is lower across the basin applying K2s (see the checkerboard test in Fig. 4.8a-b). The resolved areas (i.e., those where sources and receivers are located) show similar patterns with both kernels (compare Fig. 4.9b and Fig. 4.8c). We thus build the forward modelling and discussion focusing on

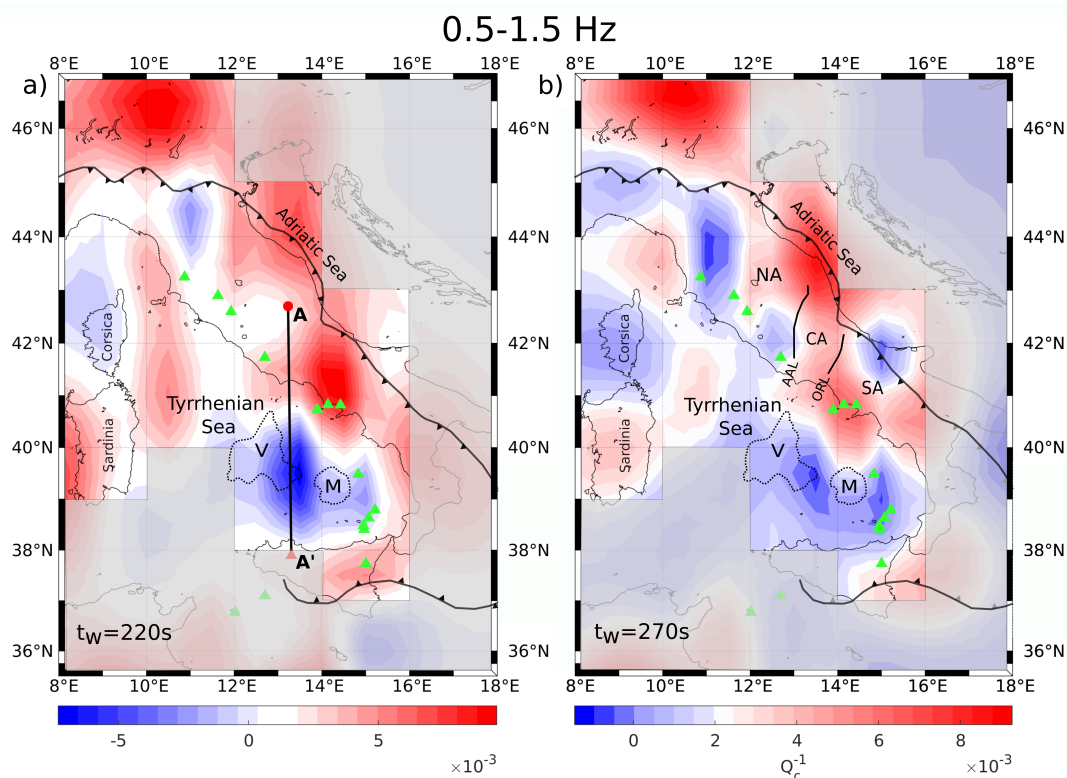


Figure 4.9: Lateral variations in seismic absorption in the frequency band 0.5-1.5Hz, estimated in the coda window 220-320 s (a) and 270-360 s (b). The grey areas are those not resolved through the inversion and are determined using the checkerboard test results (Fig. 4.7). Profile AA' marks the section modelled with Radiative3D: the modelled sources are located in A and the receiver in A'. The dotted lines highlight the two main sub-basins, Vavilov (V) and Marsili (M), in the Southern Tyrrhenian Sea. The green triangles represent the volcanic centers. The main structural feature represented by the black line is the thrust front. The boundary between the northern (NA), central (CA) and southern (SA) Apennine domains are defined by the Anzio-Ancona Line (AAL) and Ortona-Roccamonfina Line (ORL) (Rosenbaum et al., 2008).

the analytic kernel-based inversion.

4.3.2 Modeling with Radiative3D

Previous tests suggest that, on average, transient coherent phases do not affect the coda wavefield for the onset $t_w = 220s$. The test is often used as a benchmark for equipartition in the continental crust, a necessary condition to apply diffusive techniques (Calvet and Margerin, 2013; Sketsiou et al., 2020). Regardless, the diffusion approximation is unlikely to be applied at these frequencies and lapse times across the entire

medium. The outliers across the epicentral distance range (Fig. 4.4) are indicative of non-diffusive behaviour at specific distances. Likely causes are shallow Moho depths, which characterize especially the southern Tyrrhenian Sea (Manu-Marfo et al., 2019), and reverberating phases in the crust linked, e.g., to sediment accumulation (Shapiro et al., 1996) and volcanic activity (Mele et al., 1997). We use the map obtained for $t_w = 220s$ to guide the radiative transfer forward modelling and thus clarify the origin of the anomalous results in the tomographic maps. We select source-station paths that cross anomalies with negative Q_c values and areas of shallow Moho depths under the resolved portions of the Tyrrhenian Sea (Manu-Marfo et al., 2019). Seismic waves travelling through these regions are governed by crustal phases, whose propagation is influenced mostly by crustal thickness variation and sediments accumulation (Zhang and Lay, 1995; Shapiro et al., 1996).

The Radiative3D code is the ideal framework to forward model envelopes in these settings (Sanborn et al., 2017), testing the onset of Lg waves and leakage effects related to the imaged structures. Radiative3D can model the combined effects of both large-scale and small-scale structures on the seismograms envelopes (see Chapter 3 for more details). The code provides the distribution of seismic energy inside the medium by joining coherent ray propagation in deterministic structures and the effects of background velocity fluctuations on direct and scattered waves.

The setup of the simulation includes meshes representing water, sediments, crustal layers, and Moho. The layers are characterized by different values of velocity fluctuations percentage ε , correlation length a (for a von Karman heterogeneity spectrum), and coda quality factor Q . The Moho depth is set according to two different studies: Manu-Marfo et al. (2019) and Finetti (2003). We simulate an azimuthally symmetric medium, i.e, one that does not take into account lateral variations of the crustal profile. The velocity of each layer is set according to Manu-Marfo et al. (2019) (Tab. 4.2). Then, we varied the Moho depth, the scattering parameters and the values of the velocity in each layer along the profile to obtain the best fit between the synthetic envelope and the real data. As ε and a are affected by important trade-offs (Cormier and Sanborn, 2019) we decided to keep a constant and only vary ε . From preliminary analyses, the arrival of coherent phases (direct, reflected, or refracted) is mostly affected by changes in Moho depth. Thus we kept the velocities in each layer constant.

4.3.2.1 Selected earthquakes for comparison

We selected from the INGV catalog (<http://cnt.rm.ingv.it/>) two earthquakes that occurred in central Italy in 2016. We considered a high broadband and high gain seismometer, located in Sicily (37.89° , 13.30° - IV.CORL). For this source-receiver geometry, the waves propagate across the main negative values of Q_c^{-1} . The first filtered signal in Fig. 4.11 corresponds to an earthquake (Event A) located at (42.7° , 13.23°) and a depth of 8 km. Fig. 4.12 shows the filtered signal of the second event (Event B) located at (42.6° , 13.29°) and at a depth of 9 km. The sources location is implemented based on the INGV catalog. Both earthquakes nucleated on normal faults, as shown by their almost-identical focal mechanisms calculated by the INGV (Fig. 4.10). The strike, dip, and rake parameters were embedded in Radiative3D to simulate the source.

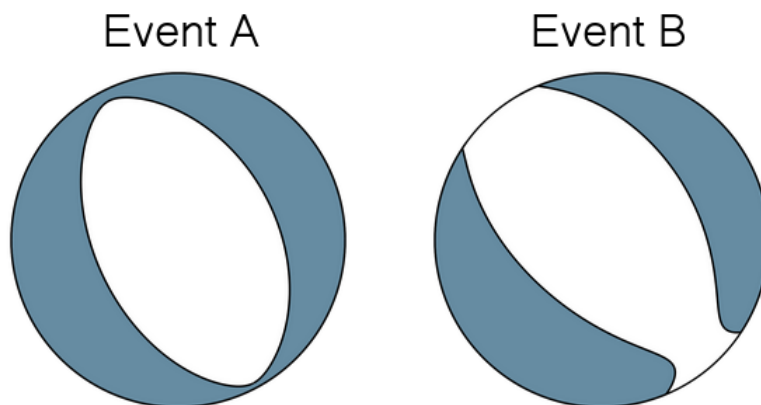


Figure 4.10: Focal mechanisms of the two seismic sources A and B located in Central Italy and modelled via Radiative3D.

4.3.2.2 Parametric study

All the parameters necessary to forward model coherent waves in Radiative3D are presented in Tables 4.1-4.2. The model that best fits both seismic arrivals and direct-wave amplitudes (Model 1 - Table 4.1) is the one where the Moho rises gradually from the Italian coast towards the south of the Tyrrhenian sea, producing a thin crustal pinch (Figure 4.11a). Figure 4.11b and 4.12 compare the synthetic energy envelope produced by this model at 1 Hz with the seismogram of Event A and Event B filtered between 0.5 and 1.5 Hz. We also show a second model obtained in our parametric study, where both steepness of the Moho and pinches onsets are kept at the same locations, but the Moho

is deeper (Fig. 4.13). The second model reproduces the S- and early-coda wave energies efficiently, but it fails to retrieve the onset and amplitude of compressional waves. The fit to the observed P coda fails likely due to a missing correction for P versus S radiated phonons in Radiative3D, which does not handle source spectral differences for P and S waves (Venkataraman and Kanamori, 2004; Yang and Ben-Zion, 2016).

| | Model 1 | | Model 2 | |
|-----------------|-----------|---------|-----------|---------|
| | Unpinched | Pinched | Unpinched | Pinched |
| Sediments/Sea | 2 km | 4 km | 2 km | 4 km |
| Crust | 35 km | 7 km | 43 km | 22 km |
| Moho transition | 5 km | 5 km | 5 km | 5 km |

Table 4.1: Layers thicknesses set up in Model 1 and Model 2. In the pinched region, the models do not include sediments: the first 4km thick layer represents the sea.

| | V_P | V_S | ρ |
|-------------|--------------|--------------|--------|
| Sediments | 5.22 to 5.45 | 2.90 to 2.95 | 2.20 |
| Sediments* | 2 to 2.5 | 1.00 to 1.50 | 1 |
| Crust | 5.40 to 6.84 | 3.00 to 4.10 | 2.80 |
| Crust* | 5.75 to 6.47 | 3.25 to 3.70 | 2.80 |
| Transition | 6.87 to 7.20 | 4.15 to 4.20 | 3.40 |
| Transition* | 6.56 to 6.65 | 3.75 to 3.80 | |
| Mantle | 7.60 and up | 4.30 and up | > 3.50 |

Table 4.2: P- and S-waves velocities (V_P , V_S) and densities (ρ) characterizing the layers in Model 1 and Model 2. * refers to the layers in the pinched region.

Once the parameters controlling deterministic propagation were set, we varied the scattering (ε) parameters in both the crust and the mantle (Table 4.3), trying to fit the broadening of crustal phases (Fig. 4.14). The best forward model of the seismogram associated with Event A corresponds to the shallow Moho (Fig. 4.11) and a relevant contrast between high scattering in the crust and low scattering in the mantle. The same is apparent when selecting Event B, recorded at the same station (Fig. 4.12).

As in Cormier and Sanborn (2019), we discuss the effects of regional and local heterogeneities on seismic wave propagation in terms of different scattering regimes by exploiting the trade-off between the velocity fluctuation ε and the scale length a , i.e, the heterogeneities size. Fig. 4.15 shows different combinations of ε and a , corresponding to different am product, where m is the wavenumber. By varying these two parameters, the trade-off $am \sim 1$ (corresponding to $\varepsilon^2 a$) allows the retrieval of the same synthetic

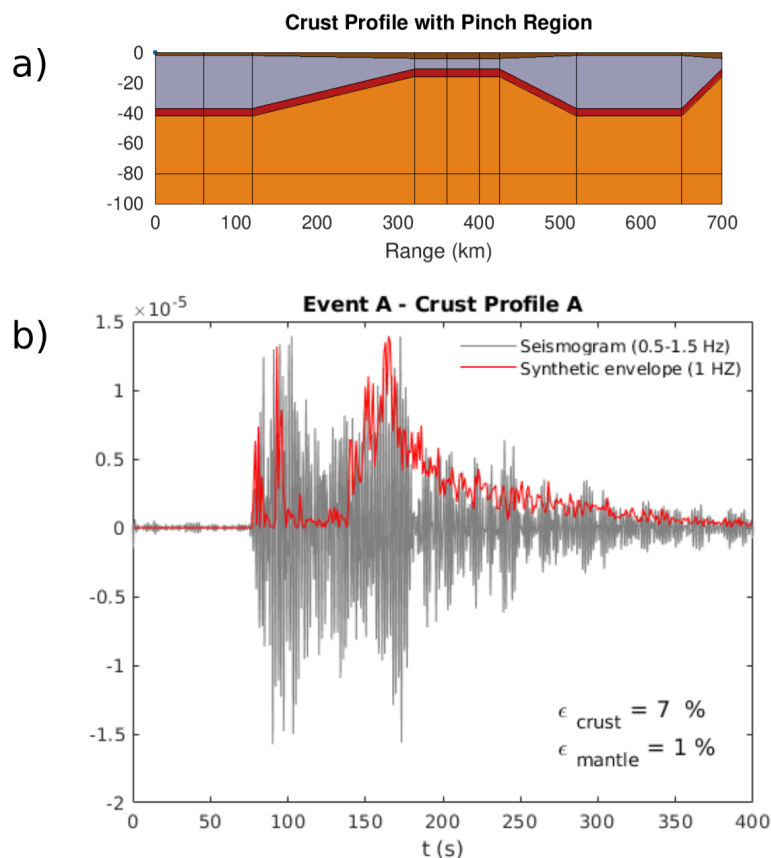


Figure 4.11: (a): Setup of Model 1: layers below the free surface represent sediments and water, the crust, the Moho transition, and the mantle. Layers thicknesses and velocities are shown in Tabs. 4.1-4.2, respectively. (b): The red envelope is obtained by simulating a source with the characteristics of Event A. The receiver is at an epicentral distance of 534 km with an azimuth of 175° .

| | Layers: sediments-crust-pinch-moho-mantle | | | | |
|------------|---|-----------------------------|--|--|--|
| | ϵ | | | | |
| | Q_s | | | | |
| Fig. 4.11b | 0.07, 0.07, 0.07, 0.01, 0.01 | 500, 1500, 2000, 1500, 1000 | | | |
| Fig. 4.14a | 0.07, 0.07, 0.07, 0.06, 0.06 | " | | | |
| Fig. 4.14b | 0.04, 0.04, 0.04, 0.01, 0.01 | " | | | |

Table 4.3: The values of ϵ and Q_s corresponding to the different layers (sediments, crust, crust in the pinched region, Moho transition and mantle) are shown in this table for the different synthetic envelope we obtained.

envelope in Fig. 4.11. Wu and Aki (1988a) describe this scattering domain as resonant scattering (Mie scattering) due to heterogeneities with a size comparable to the wave-

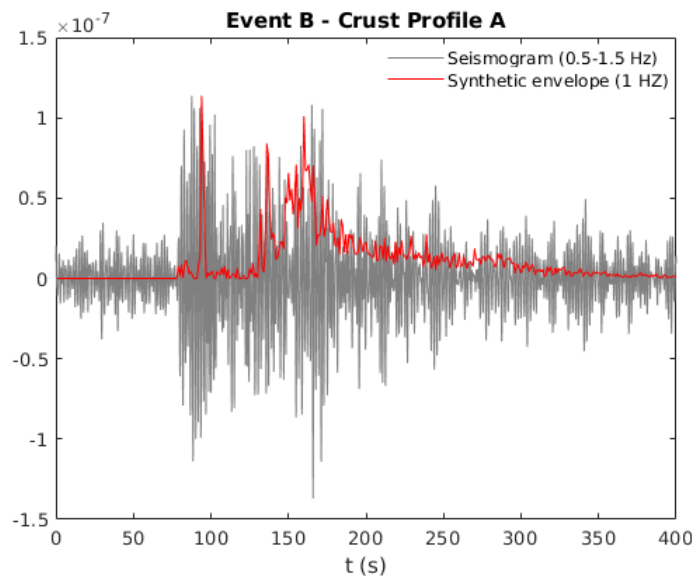


Figure 4.12: The red envelope is obtained by simulating a source with the characteristics of Event B for the same station located in Sicily. The set up of the model is shown in Fig. 4.11a

length. We filtered the signal in the frequency band 0.5 – 1.5 Hz: as the corresponding wavelength is around 7 – 3 km, the propagation is affected by the presence of the crustal pinch, where the crust is only 7 km thick.

At these frequencies and lapse times, a choice of the coda time-window based exclusively on the stability of Q_c with epicentral distance (Fig. 4.4) clearly oversimplifies the complexities induced by a changing Moho and crustal thickness variations and changing sediment accumulation. As here the Mie scattering regime rules scattering propagation, crustal reverberations are the dominant physical mechanism generating coda, explaining the anomalous behaviour of the tomographic maps. The trade-off between ε and a (Fig. 4.15) shows that: (1) at these frequencies a high-scattering regime (ε^2/a) is unable to model the early coda; (2) synthetic envelopes corresponding to different scattering regimes are still clearly separated at 220 s but progressively coincide from 270 s onwards. This onset is preferred to estimate the Q_c parameters, as the overlap between envelopes is a better marker of a multi-scale diffusive process.

4.3.2.3 Comparison between data and synthetic Q_c^{-1}

We measure Q_c using the time window 270-360 s for the synthetic traces recovered for Events A (Mw 6.0) and B (Mw 4.8), shown in Figures 4.11b and 4.12, respectively.

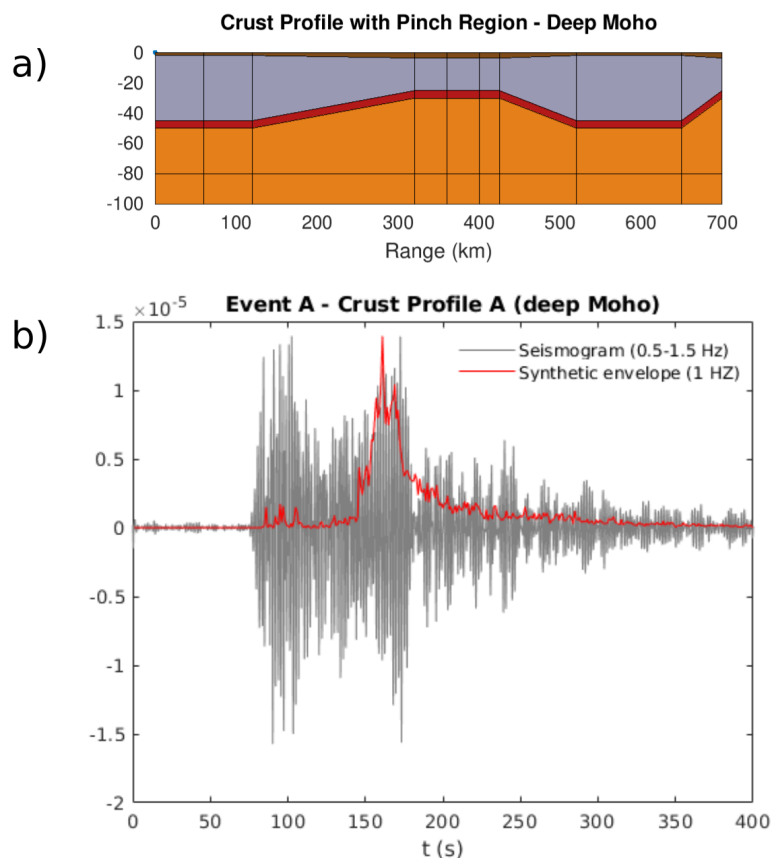


Figure 4.13: (a): Setup of Model 2: layers below the free surface represent sediments and water, the crust, the Moho transition and the mantle. Layers thicknesses and velocities are shown in Tabs. 4.1-4.2, respectively. (b): The red envelope is obtained by modelling a source with the characteristics of Event A.

The Radiative3D code does not account for the earthquake magnitude, so the synthetic traces are normalised to the maximum amplitude of the real data. The agreement between synthetic and data Q_c^{-1} is excellent for the high-magnitude Event A (Fig. 4.16). The low-magnitude Event B has a lower signal-to-noise, and the coda window 270-360s is thus dominated by noise, with no agreement between the synthetic and real Q_c^{-1} . We remind that this event was discarded from our tomographic procedure. This observation implies that low-magnitude coda waves could be blocked in the presence of strong Moho variations.

To evaluate energy leakage and crustal reverberations due to crustal thickness variations, we obtained the synthetic trace Q_c^{-1} with and without the pinched region. Figure

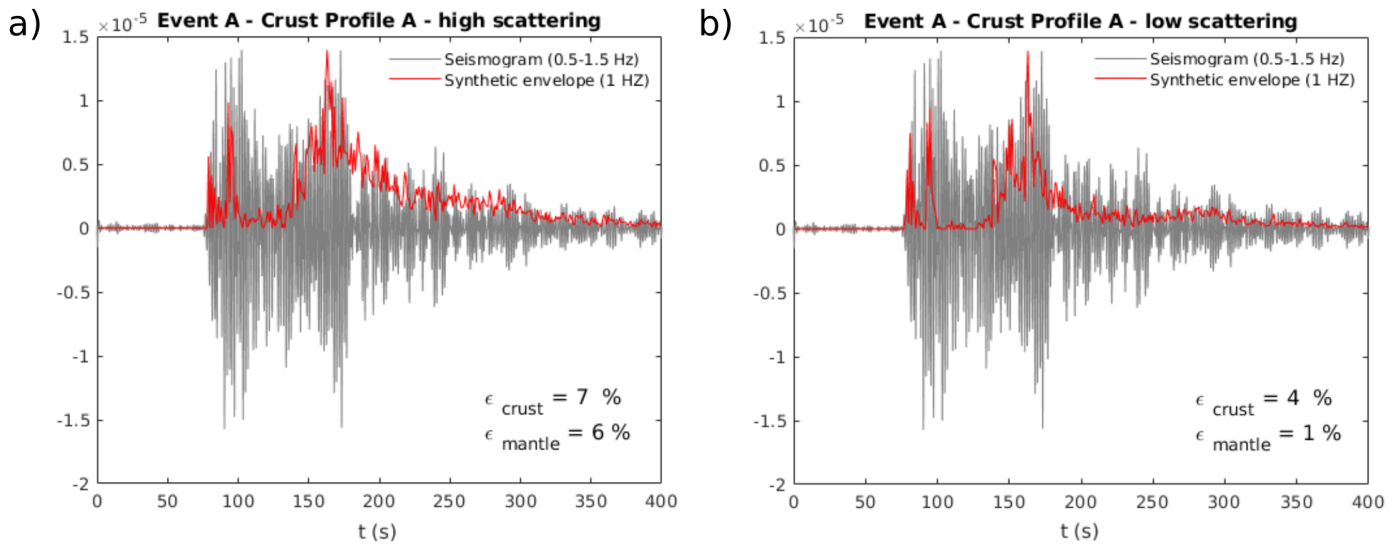


Figure 4.14: (a) represents the synthetic envelope obtained by setting high scattering values in the crust and the mantle, i.e $\epsilon = 7 - 6\%$. (b) shows the results by setting lower ϵ values: 4% for the crust and 1% for the mantle .

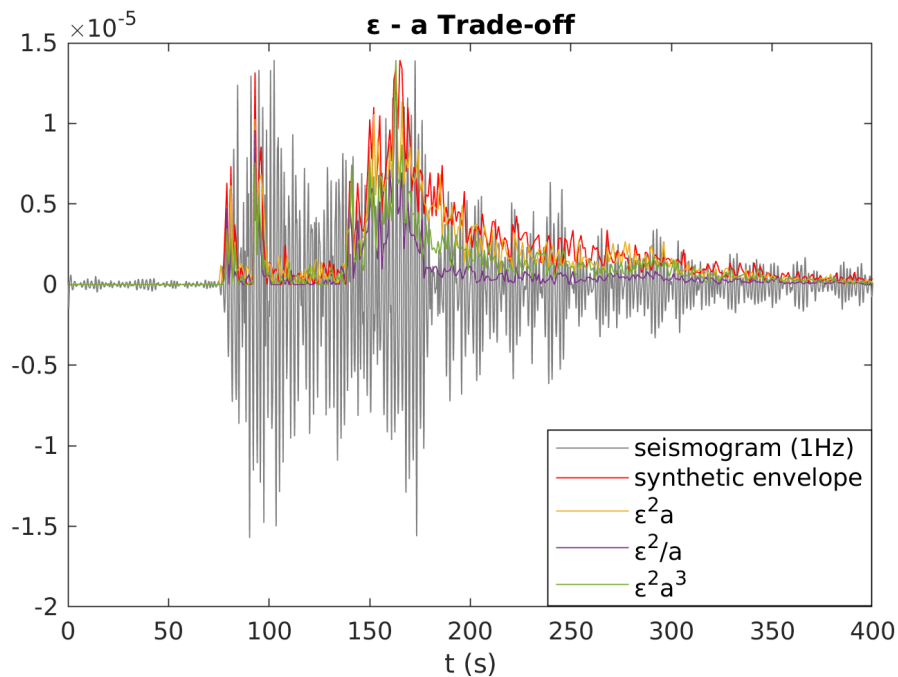


Figure 4.15: The grey signal represents the real seismogram filtered at 0.5-1.5 Hz. The red envelope is the synthetic one and the other envelopes correspond to different scattering domains (yellow: $am \sim 1$, purple: $am \gg 1$, green: $am \ll 1$)

4.17 shows the synthetic traces and Q_c^{-1} values obtained for the two models. The comparison shows the dramatic leakage affecting direct wave energy and the reduction of peak delays in the presence of a shallow Moho (Calvet and Margerin, 2013; Borleanu et al., 2017). However, the shallow Moho causes reverberations that apparently flatten the envelope, causing lower coda attenuation. In Figure 4.18), we show the Q_c^{-1} calculated in three different coda windows. We demonstrate that the presence of the pinch generally increases the Q_c^{-1} value except for the window 270-360s where the effect of crustal reverberations turns out to be dominant. This observation indicates that diffusion cannot be reached even at these later lapse times (Morozov and Safarshahi, 2020).

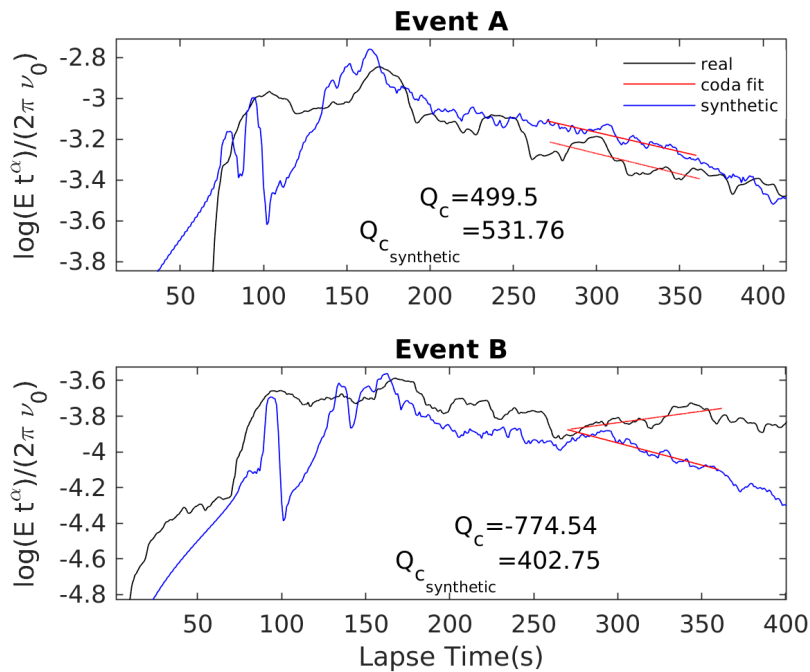


Figure 4.16: Comparison between the Q_c value estimations obtained for the synthetic traces and the station recordings.

4.4 Discussion

4.4.1 Southern Tyrrhenian basin

By mapping coda attenuation (Fig. 4.9a), we found the main negative Q_c anomaly located in the region characterized by the shallowest Moho mapped by Manu-Marfo et al. (2019) in the Southern Tyrrhenian basin. Then we forward modelled envelopes

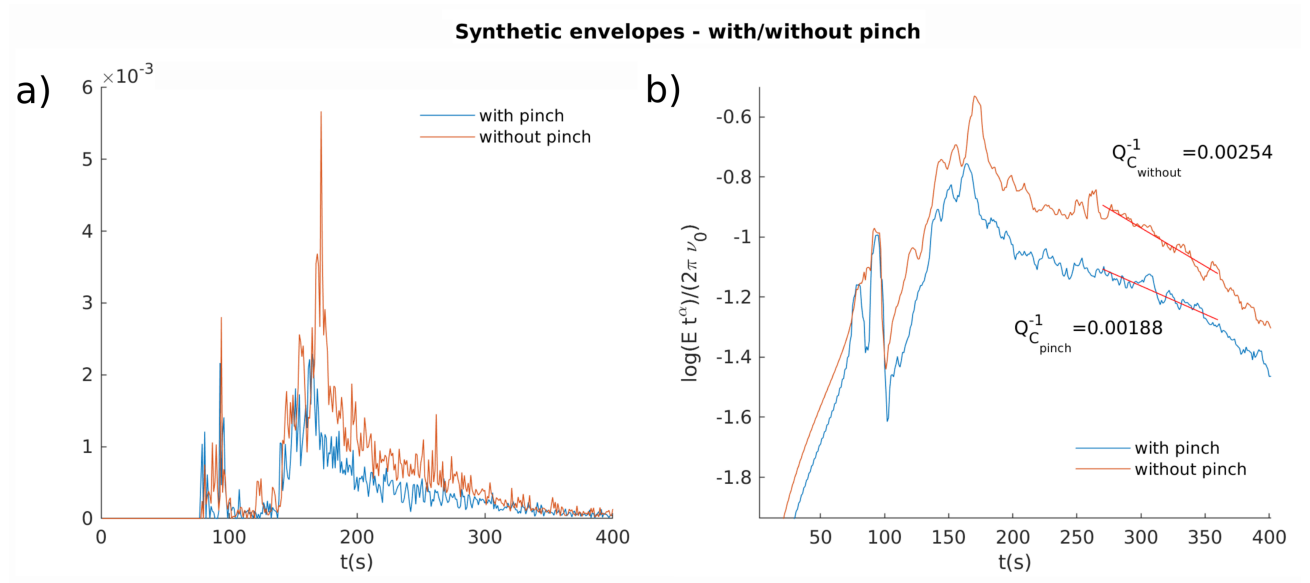


Figure 4.17: (a) Synthetic envelopes obtained for the crustal layer with and without the pinch. (b) Estimation of the coda quality factor from the synthetic envelopes.

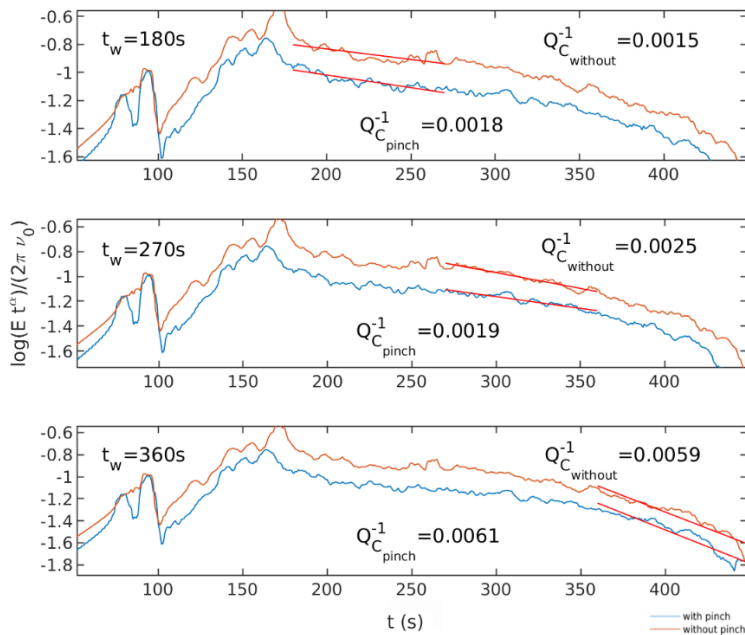


Figure 4.18: We obtain synthetic envelopes for crustal models with (blue line) and without (orange line) the pinched region. We compare the Q_c^{-1} values obtained in 3 different coda windows from these two synthetic envelopes, keeping fixed the window length at 90 s.

across this region. The best Radiative3D model of seismic phases and amplitudes is indeed obtained for a very shallow Moho (Moho depths $< 15\text{km}$), which must characterize the area of pinch between 41 and 38 degrees of latitude and 13 degrees of longitude. The anomalous behaviour of this region is thus linked to the formation of Lg waves, which are unexpected for such shallow Moho depths. Tomographic and Radiative3D models both suggest the existence of a structure different from the typical surrounding oceanic crust. In the central and southern Tyrrhenian basin, the negative Q_c anomalies obtained in a diffusive approximation are thus a reliable indicator of a higher-scattering volume and crustal reverberations, and cannot be interpreted with a standard separation of scattering and intrinsic attenuation.

Lg waves propagate through the continental crust at velocities between about 3.2 and 3.6 km/s (Campillo et al., 1985; Romanowicz and Mitchell, 2007). We can assume that the coda envelopes are still dominated by crustal phases and the earlier coda window imaging comprises the coda of the Lg phase recorded across profile AA'. Most of the studies regarding the Lg phase focus on its onset in frequency bands from 0.5 Hz up to 3 Hz or above (Campillo et al., 1985; Zhang and Lay, 1995; Rodgers et al., 1997; Baumgardt, 2001; Sens-Schönfelder et al., 2009). By targeting the 1 Hz frequency band (0.5 – 1.5 Hz) we demonstrated that a weak scattering regime, the preferred model for continental-scale propagation (Mitchell et al., 2008), is unable to model our observations (Fig. 4.15). The differences in Lg propagation observed across the Tyrrhenian Sea (Mele et al., 1997) are thus likely due to the onset of the Mie scattering regime. In this regime, scattering and absorption imaging techniques that are either based on a single- (small) scattering regime (Mitchell et al., 2015) or on higher-scattering approximations (Calvet et al., 2013; Sato et al., 2012; Sketsiou et al., 2020) are strongly biased.

While estimating Q_c , we did not apply any correction for the leakage of energy into the mantle, which potentially contributes to the decay of the coda around 1Hz (Korn, 1993; Margerin et al., 1999). The gradient in Moho topography we propose through our modelling can cause this energy leakage as a result of the reduced angle of incidence of the raypath (Bostock and Kennett, 1990). However, leakage should reduce, not increase the energy recorded across the pinch, thus producing higher, not lower attenuation.

As the shallow-Moho profile in Fig. 4.11a is the best to forward model the signal, the crustal thinning does not corrupt the efficiency of the Lg propagation and its amplitude, which is comparable to the compressional phases (Fig. 4.11b, Fig. 4.13b). Shapiro et al. (1996) and Baumgardt (2001) have observed that Moho depths are actu-

ally not as important as expected for the blockage of the Lg phase. They found out that thick sediment accumulation in a sedimentary basin could be responsible for the attenuation of the crustal phase because energy is transferred into slow shear waves trapped inside the sediments. The presence of thin sediments in the Southern Tyrrhenian basin and their absence especially across the considered path has been assessed by several studies (Duschenes et al., 1986; Moskalenko, 1992; Pepe et al., 2005; Pontevivo and Panza, 2006). It is thus the most likely explanation for the more efficient propagation of Lg in the Southern Tyrrhenian basin with respect to the northern part (Shapiro et al., 1996) where thicker sedimentary layers are present (Moeller et al., 2013). Also, if the characteristics of the region crossed by profile AA' are very different from those around them, such wave trapping becomes a feasible explanation of the anomalously-high energy recorded in the Lg coda.

While the Moho map of Manu-Marfo et al. (2019) shows unique shallow Moho across the negative Q_c area, (Sartori, 2003) pointed out a small region of deeper Moho inside it. This region has been geologically identified as a portion of continental crust, named Issel bridge, separating the recent and small Marsili basin in the East from the larger Vavilov basin in the West. These two oceanic sub-basins, the Vavilov Plain and the Marsili Plain, are separated by a thicker continental crustal layer, where the Moho depth supposedly increases up to $\sim 15km$ (Mascle and Rehault, 1990; Sartori, 2003). The presence of continental and high-velocity crust is thus highlighted by the negative Q_c^{-1} in the inversion results obtained with the coda window starting at $tw = 220$ s (Fig. 4.9a) and is confirmed by the forward modelling. At these time lapses, the hypothesis of a single uniform layer comprising propagation is invalid. The mapping of coda anomalies at these frequencies and scales is instead a marker of a sharp lateral variation in Moho depths associated with alternating oceanic and continental crust. While the results obtained at a longer coda-window onset ($t_w = 270$ s) are more likely to represent absorption patterns, they still confirm the anomalous attenuation characteristics of this portion of the Tyrrhenian Sea.

Both coda windows show an average Q_c^{-1} value equal to $2.7 \cdot 10^{-3}$ ($Q_m = 370$) for the resolved areas. For the continental region in Northern Italy, Mayor et al. (2016) provide a Q_c^{-1} average value for the frequency band 1-2Hz ($Q_m = 203$), which is higher than our estimation. A higher Q_c^{-1} value is retrieved also by Bianco et al. (2002) for the Southern Apennines. However, both these measurements are done in regions of thick Moho. We are mapping attenuation in a wider area comprising the oceanic basin. As

demonstrated in Figure 4.17, the regions of crustal reverberations lower the Q_c^{-1} values within the basin, and thus their average over oceanic datasets. While this observation goes against the standard application of coda-wave imaging (Calvet and Margerin, 2013; Borleanu et al., 2017), this sensitivity opens a pathway for the measurement of Moho depths using coda attenuation variations.

4.4.2 The Apennines and the Northern Tyrrhenian basin

Both coda window choices show similar coda attenuation patterns along the Italian peninsula (Figure 4.9). The maps obtained at a later onset are interpreted as absorption maps (Calvet et al., 2013), thus strictly correlated to fluids/melts, sediments, and complex fault systems. The highest resolved Q_c^{-1} values are indeed clearly related to both thermal heterogeneities marking magmatism and sedimentary basins. The first very-high absorption anomaly extends across the Central Campanian province, a region characterized by high heat flow (Scrocca et al., 2003) and coincides (at $\sim 14^\circ, 41^\circ$) with the magmatic systems of the Neapolitan volcanoes (Fig. 4.9b). Across the Po Plain (Northern Italy) and the Adriatic coast, we found a good spatial correlation between high-absorption anomalies and sedimentary basins that can reach down to 15 km of thickness (Molinari et al., 2015a), in regions characterised by low- V_p anomalies across the Apennine foredeep (Di Stefano et al., 2009). In addition to these primary high-absorption anomalies along the Italian peninsula, a trend of relatively-high absorption follows the Apennines and shows good consistency with the current tectonic front. Only the stable Apulia platform, at the margin of our resolved area, is characterized by average attenuation.

The Northern Tyrrhenian basin is overall characterized by low velocities (Molinari et al., 2015b) that support the existence of a thick sedimentary cover (Moeller et al., 2013). Causing the inefficient propagation of Lg wave (Shapiro et al., 1996), these sediments are likely responsible for the relatively-high absorption anomaly between the Sardinia-Corsica block and Tuscany.

Di Stefano et al. (1999) retrieved deep (22 km and below) high-velocity anomalies beneath the peri-Tyrrhenian margin of the Apennines from northern Tuscany to the south. They related these anomalies to strong impedance contrasts producing reflections indicative of a relic of the European lithosphere (Pauselli et al., 2006). The low-absorption anomalies found across the western part of the Northern Apennines (Fig. 6) support the existence of an older lithospheric body extending in this area. Low coda-

attenuation patterns similar to ours have been obtained in the area by Soergel et al. (2020), who mapped Q_c^{-1} using the coda of noise cross-correlations and a regionalization approach.

4.5 Concluding remarks

We have tested kernel-based coda attenuation imaging in the diffusive approximation at the regional scale (epicentral distances $> 400km$) in a mixed continental-oceanic setting. We have obtained tomographic maps of coda attenuation for both the Italian peninsula and the Tyrrhenian Sea for two different coda windows. A negative attenuation anomaly obtained for the coda window 220 – 320 s suggests that the diffusive approximation is unfulfilled across an SN-trending region within the Southern Tyrrhenian basin. This region of continental crust separates two oceanic basins (Vavilov and Marsili) and allows a more efficient propagation of the crustal Lg phase than expected at these lapse times. These interpretations guided a Radiative Transfer forward modelling of the seismic energy envelope that combines the effects of both large-scale and small-scale structures, responsible for deterministic and stochastic scattering processes. A Radiative3D-based inversion of full envelopes for direct- and coda-wave attenuation appears an ideal tool to resolve trade-offs between data coverage and forward modelling in attenuation imaging of mixed continental and oceanic settings.

The results highlight the mixed oceanic-continental nature of the southern part of the Tyrrhenian Sea, and the effect of Moho depth variations across the basin, which control intermediate and late-lapse-time coda waves energies. By varying the trade-off between the scale length and the velocity fluctuations parameters, the Mie scattering regime is the most appropriate to fit the behaviour of the whole envelope. The differences between this and lower-scattering regimes are reduced using coda envelopes measured from 270 s onward. Coda attenuation anomalies mapped using later onsets apparently resolve bodies associated with high absorption along the Italian peninsula, especially where geodynamic modelling infers the inflow of asthenospheric materials in the lowermost part of the crust, feeding magmatic systems. The primary high-attenuation pattern coincides with the location of the magmatic systems feeding the Neapolitan volcanoes. The other high-attenuation anomalies across the Po Plain and the Adriatic coast are in agreement with the presence of thick sediment covers. Our results show the potential to resolve variations of Moho depths and sediments in the oceanic setting, regions of

crustal reverberations, and volcanism.

Chapter 5

Wave equation modelling

In the second part of the thesis, I have improved the forward model of the seismic wavefield energy with full-waveform modelling to explore the 3D propagation of waves, including the effects of topography, bathymetry and laterally varying interfaces. The following chapters thus introduce the wave equation and the finite difference method to compute numerical solutions.

5.1 The seismic wave equation

The field to determine is either the displacement field $u_i(x, t)$ or its time derivative the velocity field $v_i(x, t) = \partial_t u_i(x, t)$. The displacement field is correlated to the strain field $\epsilon_{ij}(x, t)$, which in turn is proportional to the stress field $\sigma_{ij}(x, t)$ with the general fourth-order tensor of elastic constants $c_{ijkl}(x)$ as proportionality factors. Elastic constants and space-dependent density $\rho(x)$ characterize and represent the geophysical properties of the elastic Earth model. The seismic sources can be characterized by the seismic moment tensor $M_{ij}(x, t)$ or by the body forces $f_i(x, t)$.

An isotropic elastic medium is considered. As the waves propagate from the source, the relation between the stresses and displacements is given by the homogeneous equation of motion as follows

$$\begin{aligned} \rho \partial_t^2 u_x(\mathbf{x}, t) = & \partial_x [\sigma_{xx}(\mathbf{x}, t) + M_{xx}(\mathbf{x}, t)] \\ & + \partial_y [\sigma_{xy}(\mathbf{x}, t) + M_{xy}(\mathbf{x}, t)] \\ & + \partial_z [\sigma_{xz}(\mathbf{x}, t) + M_{xz}(\mathbf{x}, t)] \\ & + f_x(\mathbf{x}, t) \end{aligned} \tag{5.1}$$

This equation describes the x-component and is the same for the other two motion components. σ_{ij} indicates the stress component of the stress tensor, u_i is the displacement along i direction and \mathbf{x} is the position vector. M_{ij} and f_i are the moment tensor element and the external force component. Equation 5.1 and the equations for the other directions are known as Euler equations for elasticity, corresponding to Newton's law of motion for particles.

The equation of motion can be expressed in terms of either stress-displacements and stress-velocity. The stress tensor, that describes the forces acting on a deformable continuous medium, and the strain, that is produced by variation in displacement within the material, are related via the *constitutive equation* that characterizes the properties of the material. The constitutive law for an isotropic elastic medium is given by the generalized Hooke's law:

$$\sigma_{ij} = \lambda\theta\delta_{ij} + 2\mu\epsilon_{ij} \quad (5.2)$$

where λ and μ are the Lamé parameters and θ is the dilatation

$$\theta = \nabla \cdot \mathbf{u} = \frac{\partial u_x}{\partial x} + \frac{\partial u_y}{\partial y} + \frac{\partial u_z}{\partial z} \quad (5.3)$$

and the strain tensor has the following components

$$\epsilon_{ii} = \frac{\partial u_i}{\partial x_i} \quad (5.4)$$

$$\epsilon_{ij} = \frac{1}{2} \left(\frac{\partial u_i}{\partial x_j} + \frac{\partial u_j}{\partial x_i} \right) \quad (5.5)$$

Eq. 5.1 becomes

$$(\lambda + \mu) \frac{\partial \theta}{\partial x} + \mu \nabla^2 (u_x) = \rho \frac{\partial^2 u_x}{\partial t^2} \quad (5.6)$$

and if the three directions are combined, we have

$$(\lambda + \mu) \nabla (\nabla \cdot \mathbf{u}(\mathbf{x}, t)) + \mu \nabla^2 \mathbf{u}(\mathbf{x}, t) = \rho \frac{\partial^2 \mathbf{u}(\mathbf{x}, t)}{\partial t^2} \quad (5.7)$$

where $\nabla^2 \mathbf{u} = (\nabla^2 u_x, \nabla^2 u_y, \nabla^2 u_z)$. This is the equation of motion for an isotropic elastic medium written entirely in terms of the displacements. Eq. 5.7 can be rewritten using the vector identity

$$\nabla^2 \mathbf{u} = \nabla (\nabla \cdot \mathbf{u}) - \nabla \times (\nabla \times \mathbf{u}) \quad (5.8)$$

to obtain

$$(\lambda + 2\mu)\nabla(\nabla \cdot \mathbf{u}(\mathbf{x}, t)) - \mu\nabla \times (\nabla \times \mathbf{u}(\mathbf{x}, t)) = \rho \frac{\partial^2 \mathbf{u}(\mathbf{x}, t)}{\partial t^2} \quad (5.9)$$

To solve Eq. 5.9, the displacement can be expressed in terms of two functions according to the Helmholtz theorem

$$\mathbf{u}(\mathbf{x}, t) = \nabla\phi(\mathbf{x}, t) + \nabla \times \mathbf{\Gamma}(\mathbf{x}, t) \quad (5.10)$$

In this representation, the displacement is the sum of the gradient of a scalar potential, $\phi(\mathbf{x}, t)$, and the curl of a vector potential, $\mathbf{\Gamma}(\mathbf{x}, t)$, both of which are functions of space and time. Although this decomposition appears to introduce complexity, it actually clarifies the problem thanks to the quantities $\nabla \times (\nabla\phi)$ and $\nabla \cdot (\nabla \times \mathbf{\Gamma})$. The part associated with the scalar potential has zero curl and gives rise to compressional waves. Conversely, the part associated with the vector potential has zero divergence and causes no volume change and corresponds to shear waves.

So substituting the potentials and rearranging, Eq. 5.9 yields

$$(\lambda + 2\mu)\nabla(\nabla^2\phi) - \mu\nabla \times \nabla \times (\nabla \times \mathbf{\Gamma}) = \rho \frac{\partial^2}{\partial t^2}(\nabla\phi + \nabla \times \mathbf{\Gamma}) \quad (5.11)$$

separating compressional and shear contributions, we obtain one equation for each potential:

$$\nabla^2\phi(\mathbf{x}, t) = \frac{1}{\alpha^2} \frac{\partial^2\phi(\mathbf{x}, t)}{\partial t^2} \quad (5.12)$$

and

$$\nabla^2\mathbf{\Gamma}(\mathbf{x}, t) = \frac{1}{\beta^2} \frac{\partial^2\mathbf{\Gamma}(\mathbf{x}, t)}{\partial t^2} \quad (5.13)$$

where $\alpha = [(\lambda + 2\mu)/\rho]^{1/2}$ and $\beta = [(\mu)/\rho]^{1/2}$ are respectively the P waves and the S waves velocities.

Considering, for example, the scalar wave equation 5.12, the solution in approximation of plan wave, known as *harmonic plane wave*, is

$$\phi(\mathbf{x}, t) = Ae^{i(\omega t \pm \mathbf{k} \cdot \mathbf{x})} = Ae^{i(\omega t \pm k_x x \pm k_y y \pm k_z z)} \quad (5.14)$$

while if we consider spherical coordinates the spherical wave solution can be written in

the form (see Stein and Wysession (2009))

$$\phi(r, t) = \frac{f(x \pm vt)}{r} \quad (5.15)$$

where the factor $1/r$ represents the distance-dependent amplitude, which is related to the geometrical spreading.

Another formulation of the elastic wave equation having an important role in computational seismology is the *velocity–stress* formulation. The displacement field $u(x, t)$ is replaced by its time derivative, the velocity field $v(x, t) = \partial_t u(x, t)$ to obtain the following coupled equations

$$\begin{aligned} \rho \partial_t v_i &= \partial_j (\sigma_{ij} + M_{ij}) + f_i \\ \partial_t \sigma_{ij} &= \lambda \partial_t \theta \delta_{ij} + 2\mu \partial_t \epsilon_{ij} \\ \partial_t \epsilon_{ij} &= \frac{1}{2} (\partial_i v_j + \partial_j v_i) \end{aligned} \quad (5.16)$$

Finite-difference approaches are based on solutions to this set of coupled equations.

5.2 Seismic anisotropy

Most of the Earth's interior from samples to regional scale shows anisotropic behaviour in waves propagation. Some sort of anisotropic symmetry system has to be considered to explain propagation features. The stress σ_{ij} of an anisotropic body is related to the deformation by

$$\sigma_{ij} = c_{ijkl} \epsilon_{kl} \quad i, j, k, l = 1, 2, 3 \quad (5.17)$$

where c_{ijkl} is a fourth-order 9x9 tensor, which can be reduced to a 6x6 matrix c_{pq} with 21 independent elements due to symmetry conditions.

Elasticity matrix c_{pq} can be used to differentiate the different anisotropy symmetries for stress and strain relation. According to Carcione (2007), three primary cases of anisotropy are described as follows

$$C_{monoclinic} = \begin{bmatrix} c_{11} & c_{12} & c_{13} & 0 & c_{15} & 0 \\ c_{12} & c_{22} & c_{23} & 0 & c_{25} & 0 \\ c_{13} & c_{23} & c_{33} & 0 & c_{35} & 0 \\ 0 & 0 & 0 & c_{44} & 0 & c_{46} \\ c_{15} & c_{25} & c_{35} & 0 & c_{55} & 0 \\ 0 & 0 & 0 & c_{46} & 0 & c_{66} \end{bmatrix} \quad (5.18)$$

$$C_{orthorhombic} = \begin{bmatrix} c_{11} & c_{12} & c_{13} & 0 & 0 & 0 \\ c_{12} & c_{22} & c_{23} & 0 & 0 & 0 \\ c_{13} & c_{23} & c_{33} & 0 & 0 & 0 \\ 0 & 0 & 0 & c_{44} & 0 & 0 \\ 0 & 0 & 0 & 0 & c_{55} & 0 \\ 0 & 0 & 0 & 0 & 0 & c_{66} \end{bmatrix} \quad (5.19)$$

$$C_{transversely\ isotropic} = \begin{bmatrix} c_{11} & c_{12} & c_{13} & 0 & 0 & 0 \\ c_{12} & c_{11} & c_{13} & 0 & 0 & 0 \\ c_{13} & c_{13} & c_{33} & 0 & 0 & 0 \\ 0 & 0 & 0 & c_{55} & 0 & 0 \\ 0 & 0 & 0 & 0 & c_{55} & 0 \\ 0 & 0 & 0 & 0 & 0 & \frac{c_{11}-c_{22}}{2} \end{bmatrix} \quad (5.20)$$

The isotropic case can be retrieved from the latter case considering the Lamé constants: $c_{11} = c_{33} = \lambda + 2\mu$, $c_{55} = c_{66} = \mu$ and $c_{13} = \lambda$. These symmetries can describe most of the geological systems at different scales. Orthorhombic symmetry can be used to implement a finely layered medium, while the other symmetries can represent sets of cracks with cracks of different orientations.

5.3 Rheology

Rheological models describe the mechanical response of real materials under applications of stress. These models are used to characterize the viscoelastic behaviour of media based on different physical properties and composition. The fundamental rheological models are the elastic, viscous and the viscoelastic one. Different combinations of elastic and viscous behaviour allow for a quantitative description of stress-strain and the anelastic response in realistic media. The primary models are presented below

(Moczo et al., 2014):

- *elastic* media: the mechanical model for the behaviour of a perfectly elastic (loss-less) solid material is represented by a spring and stress is a linear function of strain

$$\sigma = \mu \epsilon \quad (5.21)$$

the only material parameter is a time-independent elastic modulus μ [Pa]. Stress at a given time depends only on the deformation at the same time (a Hooke solid does not have memory). The application of stress yields an instantaneous strain. Removal of the stress produces instantaneous and total removal of the strain. In other words, a Hooke solid can completely recover because the elastic energy does not dissipate (Fig. 5.1).

- *viscous* media: the model for a Newton linearly viscous liquid is described by the relation in which stress is a linear function of the strain rate

$$\sigma = \eta \frac{d\epsilon}{dt} \quad (5.22)$$

It is represented by a dashpot consisting of a cylinder filled with a viscous liquid, and a piston with holes through which the liquid can flow. The only material parameter is a time-independent viscosity η [Pa s]. The application of a step in stress leads to a linear increase of strain. The accumulated strain completely remains after the removal of the stress (a Newton liquid has memory) and the elastic energy has been dissipated (Fig. 5.1).

- *viscoelastic* models: the stress-strain relation is time-dependent. The contribution of elastic and viscous properties can be modelled in several ways to describe the viscoelastic behaviour in materials. Some of the principal models are listed below. *Maxwell model* consists of a spring and a dashpot connected in series (Fig. 5.2). For a Maxwell body, the stress remains constant and the strain variation is taken into account by the following relation

$$\frac{d\epsilon}{dt} = \frac{d\sigma}{\mu dt} + \frac{\sigma}{\eta} \quad (5.23)$$

Kelvin-Voigt model consists of a spring and a dashpot connected in parallel (Fig.

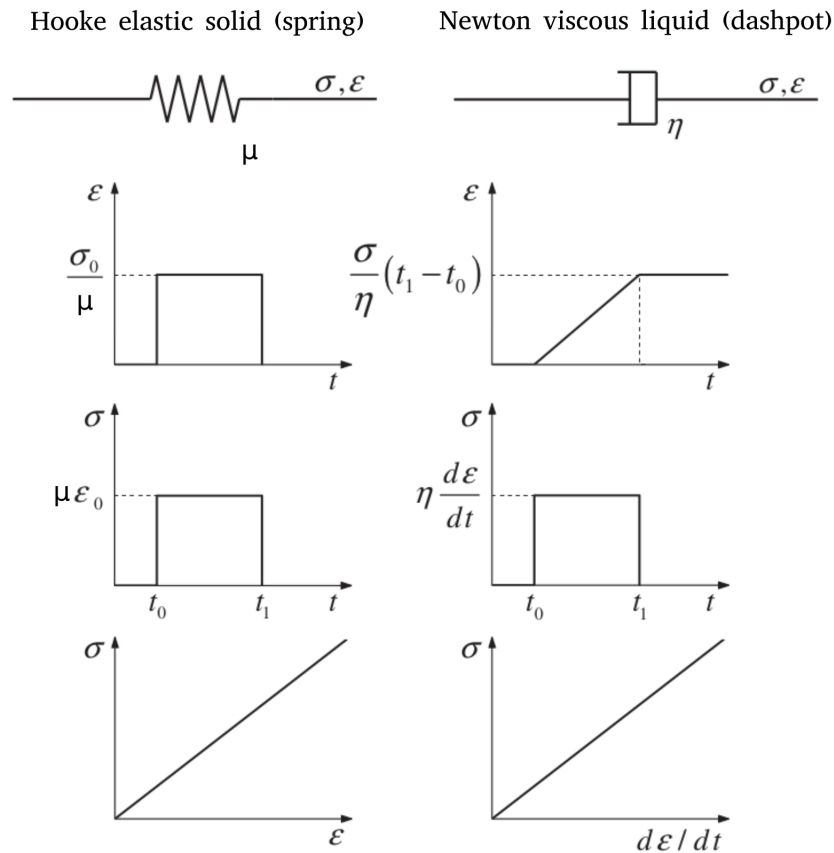


Figure 5.1: Behaviour of a Hooke solid (left) and a Newton liquid (right) upon the application of a step in stress. The lower diagrams show the relation between stress and strain.

5.2). For a Kelvin-Voigt body, the strain is constant, while the stress is

$$\sigma = \mu\epsilon + \eta \frac{d\epsilon}{dt} \quad (5.24)$$

For this model, the mathematical formulation describing the time dependency of the strain is given by the creep and the relaxation functions:

$$\begin{aligned} C(t) &= \frac{1}{\mu} (1 - e^{-\mu/\eta t}) \quad t > 0 \\ K(t) &= \mu H(t) + \eta \delta(t) \end{aligned} \quad (5.25)$$

where $H(t)$ is the Heaviside function.

When applied to realistic cases, these two models are not suitable descriptors of attenuation. The Maxwell body is capable of instantaneous elastic strain but cannot remove strain accumulated in the dashpot and return to the original equilibrium. A Kelvin–Voigt model can fully recover but is unable to respond with an instantaneous strain upon application of a step in stress.

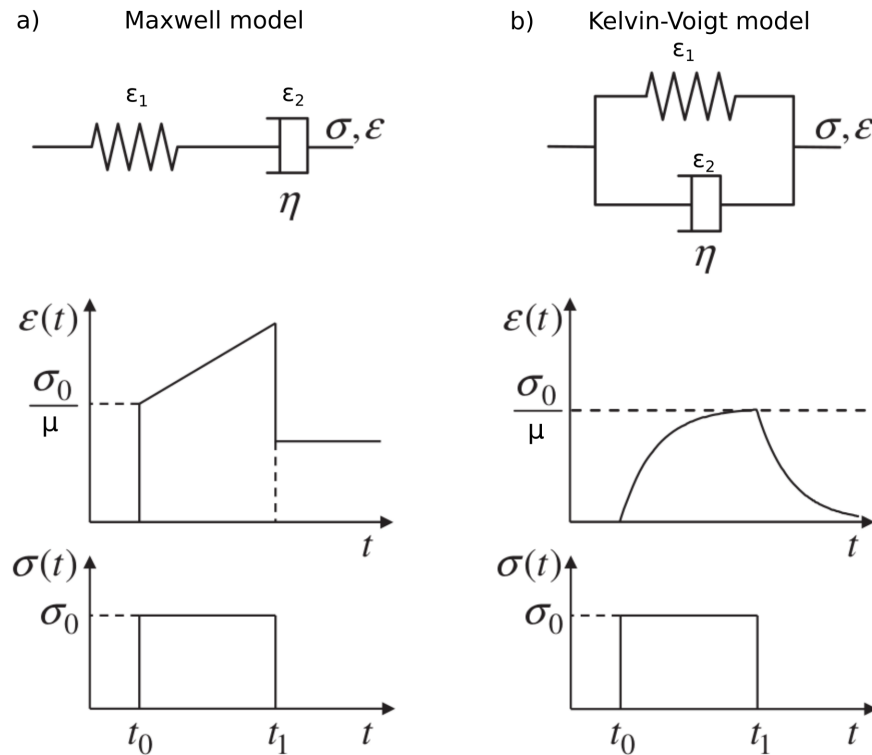


Figure 5.2: Behaviour of a Maxwell (a) and Kelvin-Voigt (b) body upon the application of a step in stress.

More complex viscoelastic models have to be taken into account to describe the rheology of real media. The *Standard Linear Solid* (SLS) model, also known as the *Zener* model, is an example. It can be composed of a Maxwell body connected in parallel with a spring to remove accumulated strain (Fig. 5.3a). Another representation of the SLS is a Kelvin–Voigt body connected in series with a spring to allow the instantaneous response with a nonzero strain upon application of a step in stress (Fig. 5.3b). The finite-difference simulation code employed in this thesis is based on the generalized Zener body (GZB) to describe the viscoelasticity. It consists of several viscoelastic Zener bodies with different relaxation times. The mathematical formulation of the relaxation functions and memory variables and its implementation in the code is explained

in Chap.6.

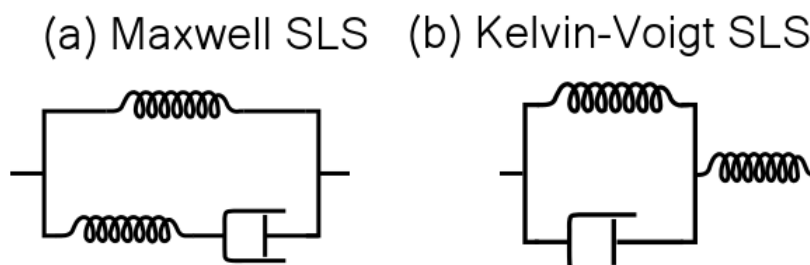


Figure 5.3: Two representations of the Standard Linear Solid model based on the Maxwell (a) and Kelvin-Voigt (b) formulation of viscoelasticity.

5.4 Source

The physical description of the seismic source parameters is a crucial aspect affecting the wavefield. Seismic sources can be parametrized as stress perturbations using the moment tensor $M_{ij}(x, t)$ or as external forces (e.g., pressure sources induced by water waves, artificial sources hitting the ground) $f_i(x, t)$. The *moment tensor* is defined as symmetric tensor with units of stress [$\text{Pa} = \text{N}/\text{m}^2$]:

$$\mathbf{M} = \begin{bmatrix} M_{11} & M_{12} & M_{13} \\ M_{21} & M_{22} & M_{23} \\ M_{31} & M_{32} & M_{33} \end{bmatrix} \quad (5.26)$$

Each element of the matrix describes a double-couple force system as illustrated in Fig. 5.4 and combining force couples of different orientations into the seismic moment tensor \mathbf{M} gives a general description that can represent various seismic sources. To describe the double-couple forces, the *scalar seismic moment* M_0 has to be defined

$$M_0 = \mu A d \quad (5.27)$$

where μ is the shear modulus, A is the surface area of the rupting fault plane and d is the average slip on the fault. It derives from the seismic moment function $M(t) = \mu d(t) A(t)$, which describes the faulting process in terms of the rigidity of the material

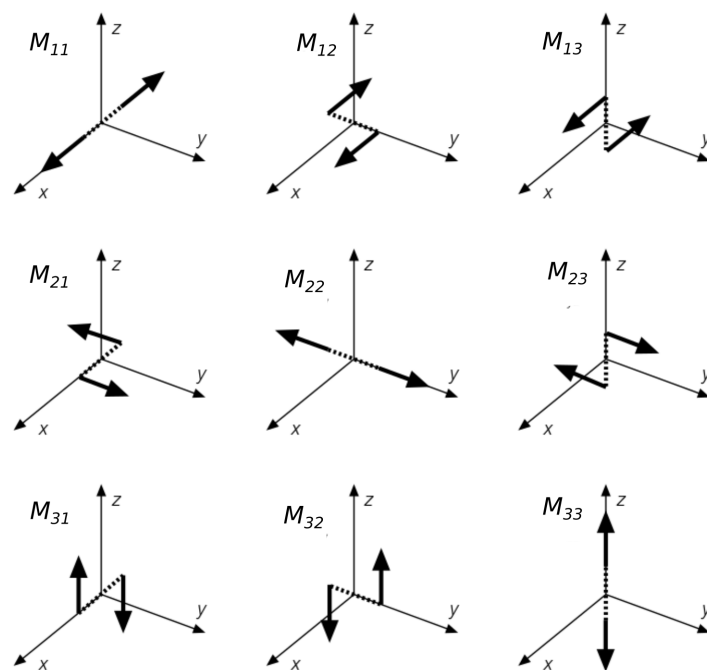


Figure 5.4: Double-couple forces corresponding to the elements of the seismic moment tensor. Each couple consists of two opposite forces separated by a distance d (dashed line), so the net force is always zero (modified from Stein and Wysession, 2009).

and history of the slip $d(t)$ and fault area $A(t)$. The terms are time-dependent, because they can vary during an earthquake. However the measure of earthquake size and energy release comes from the definition of the scalar seismic moment. The time evolution is evaluated by the *source time function* introduced in *moment rate function* $\dot{M}(t)$. The far-field displacements are proportional to the time derivative of the moment function, $M(t)$ (Lay and Wallace, 1995). The relation between the scalar moment and the force couples is

$$M_0 = \frac{1}{\sqrt{2}} \left(\sum_{ij} M_{ij}^2 \right)^{1/2} \quad (5.28)$$

The seismic moment determines the energy radiated from the seismic source and the moment tensor is responsible for the radiation pattern of P- and S-waves.

The wave-propagation problem is based on a the analytical solution to the problem of a double-couple point source in infinite homogeneous media. The displacement field radiated by a shear dislocation acting on the (x_1, x_2) plane (Fig. 5.5) can be solved and represented introducing spherical polar coordinates centered on the source. The unit vectors \hat{r} , $\hat{\theta}$, $\hat{\phi}$ represent the radial and the two transverse directions, respectively. In the displacement solution, the terms regarding the near-, the far- and the intermediate- field for P- and S- waves can be separated (Aki and Richards, 2002)

$$\begin{aligned} \mathbf{u}(\mathbf{x}, t) = & \frac{1}{4\pi\rho} A^N \frac{1}{r^4} \int_{r/\alpha}^{r/\beta} \tau M_0(t - \tau) d\tau \\ & + \frac{1}{4\pi\rho\alpha^2} A^{IP} \frac{1}{r^2} M_0\left(t - \frac{r}{\alpha}\right) + \frac{1}{4\pi\rho\beta^2} A^{IS} \frac{1}{r^2} M_0\left(t - \frac{r}{\beta}\right) \\ & + \frac{1}{4\pi\rho\alpha^3} A^{FP} \frac{1}{r} \dot{M}_0\left(t - \frac{r}{\alpha}\right) + \frac{1}{4\pi\rho\beta^3} A^{FS} \frac{1}{r} \dot{M}_0\left(t - \frac{r}{\beta}\right) \end{aligned} \quad (5.29)$$

where r is the distance from the source, ρ , α , β are density, P-velocity, and S-velocity, respectively, and $\hat{M}_0(t)$ is the source time function. It is assumed $\int \hat{M}_0 dt = M_0$, where M_0 is the scalar moment. A^N , A^I , A^F describe the radiation patterns of near-field,

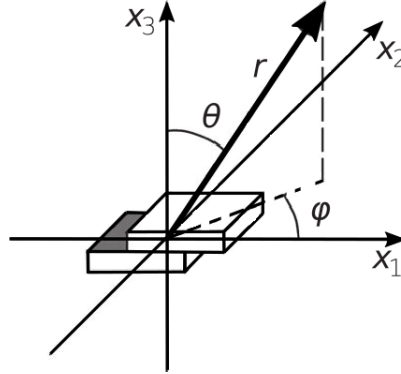


Figure 5.5: Spherical coordinates system used to describe the solution of the displacement generated by shear dislocation, which is parametrized by a double-couple point source.

intermediate and far-field for P-wave and S-wave:

$$\begin{aligned}
 A^N &= 9\sin(2\theta)\cos(\phi)\hat{r} & 6\cos(2\theta)\cos(\phi)\hat{\theta} & -\cos(\theta)\sin(\phi)\hat{\phi} \\
 A^{IP} &= 4\sin(2\theta)\cos(\phi)\hat{r} & -2\cos(2\theta)\cos(\phi)\hat{\theta} & -\cos(\theta)\sin(\phi)\hat{\phi} \\
 A^{IS} &= -3\sin(2\theta)\cos(\phi)\hat{r} & -3\cos(2\theta)\cos(\phi)\hat{\theta} & -\cos(\theta)\sin(\phi)\hat{\phi} \\
 A^{FP} &= \sin(2\theta)\cos(\phi)\hat{r} & & \\
 A^{FS} &= & +\cos(2\theta)\cos(\phi)\hat{\theta} & -\cos(\theta)\sin(\phi)\hat{\phi}
 \end{aligned} \tag{5.30}$$

5.5 Numerical methods

In seismology, the calculation of synthetic seismograms is an efficient method to better understand the structure of the Earth's interior or the sources of seismic energy. To compute seismograms from an arbitrary Earth's model, the solution of 3D partial differential equations descriptive of elastic wave propagation requires the use of numerical methods.

This can be performed using the time-domain solutions (finite differences) or the frequency-domain approaches (spectral elements). In the time-domain approach, the space-dependent seismic wavefield is computed at each time step. In frequency-domain approach, the wave equations are transformed into the spectral domain and solved for each frequency. Seismograms can then be obtained by inversely transforming the spec-

tra into the time domain.

Furthermore, synthesizing seismograms is useful to retrieve additional information about the structures and the processes governing the seismic rupture (Takemura et al., 2020). The wave equation modelling is a suitable methodology to extract information from the whole waveforms, not only from travel times. Matching complete waveforms by calculating synthetic seismograms through 3D models and directly comparing them with observations allows retrieving information from velocity to attenuation (Chen et al., 2007; French and Romanowicz, 2014; Karaoğlu and Romanowicz, 2018). In this framework, waves modelling is the basis for performing full-waveform inversion, which consists of an iterative procedure requiring the calculation of many forward problems to progressively improve the fit between synthetic and observed seismograms. Besides, the calculation of seismograms implies the implementation of a numerical algorithm that solves the seismic wave-propagation problem for any problem in 3D is computationally expensive. This process requires the *parallelization* of the codes computing the numerical solutions.

As mentioned above, the wave equation solution can be computed using different numerical algorithms (e.g., finite-difference, spectral elements). In this thesis, I performed wave equation modelling by using the finite difference method. The following sections introduce this method.

5.5.1 Finite Differences

Using the stress-displacement formulation of the wave equation, the error of a finite-difference approximation depends on the size of the increment dx employed in the derivative approximation and is a quadratic function of dx . By reducing the size of this increment by a factor of 2, the error would be four times smaller. Thus, introducing the stress-velocity formulation allows to take directly the first derivative of the material parameters and not the second derivatives. Considering 2D space, the relations

$$\begin{aligned}\partial_t u &= v \\ \sigma &= \mu \partial_x u,\end{aligned}\tag{5.31}$$

where the only non-zero stress component is $\sigma_{xy} = \sigma_{yx}$, leads to first-order differential equations

$$\begin{aligned}\rho \partial_t v &= \partial_x \sigma + f \\ \partial_t \sigma &= \mu \partial_x v\end{aligned}\tag{5.32}$$

Defining a regular spaced grid in time and space (Fig. 5.6a), the discrete unknowns are

$$v_i^j = v(i dx, j dt)\tag{5.33}$$

and replacing the partial differentials with centred finite-difference approximations to the first derivative based on the grid staggering leads to

$$\begin{aligned}\frac{v_i^{j+1/2} - v_i^{j-1/2}}{dt} &= \frac{1}{\rho_i} \frac{\sigma_{i+1/2}^j - \sigma_{i-1/2}^j}{dx} + \frac{f_i^j}{\rho_i} \\ \frac{\sigma_{i+1/2}^{j+1} - \sigma_{i+1/2}^j}{dt} &= \mu_{i+1/2} \frac{v_{i+1}^{j+1/2} - v_i^{j+1/2}}{dx}\end{aligned}\tag{5.34}$$

Velocity and stress unknowns can be extrapolated

$$\begin{aligned}v_i^{j+1/2} &= \frac{dt}{\rho_i} \frac{\sigma_{i+1/2}^j - \sigma_{i-1/2}^j}{dx} + v_i^{j-1/2} + dt \frac{f_i^j}{\rho_i} \\ \sigma_{i+1/2}^{j+1} &= \mu_{i+1/2} \frac{v_{i+1}^{j+1/2} - v_i^{j+1/2}}{dx} dt + \sigma_{i+1/2}^j\end{aligned}\tag{5.35}$$

In 2D, each component of the stress-strain relation is

$$\begin{aligned}\partial_t \sigma_{xx} &= (\lambda + 2\mu) \partial_x v_x + \lambda \partial_z v_z \\ \partial_t \sigma_{zz} &= (\lambda + 2\mu) \partial_z v_z + \lambda \partial_x v_x \\ \partial_t \sigma_{xz} &= \mu (\partial_x v_z + \partial_z v_x)\end{aligned}\tag{5.36}$$

The first derivatives of the velocity field with respect to both spatial coordinates can be evaluated based on the staggering scheme in 1D (Fig. 5.6b). At the receiver, we thus obtain the velocity wavefield at each time step.

The diagonal elements of the stress tensor are defined at the same locations. The velocity and off-diagonal stress components are defined at shifted locations along the axes. Based on this scheme, the first derivatives are calculated at these staggered grid loca-

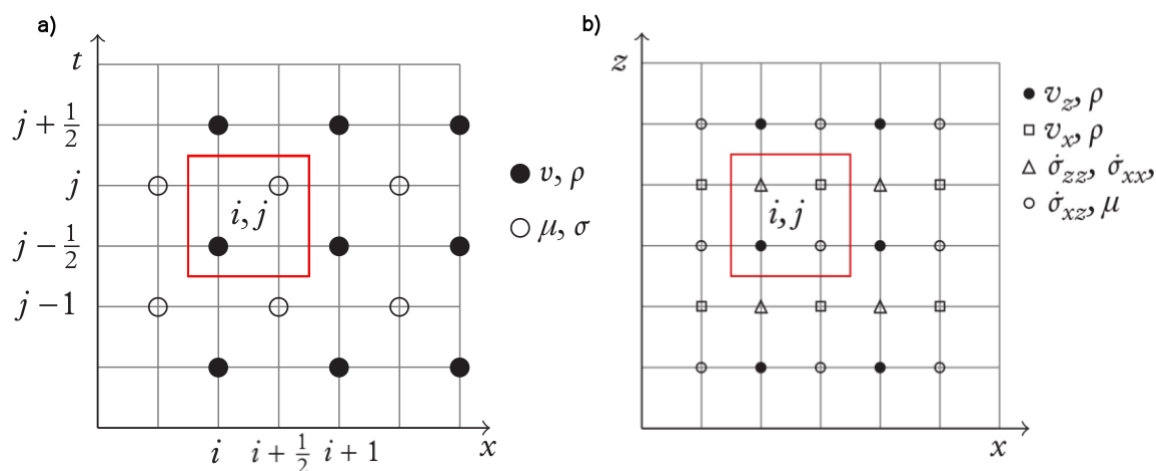


Figure 5.6: (a): spatio-temporal grid staggering in 1D with the vertical and horizontal indices corresponding to time and the space, respectively. (b): spatial grid staggering for the 2D velocity–stress formulation. (modified from Igel, 2017)

tions. To evaluate the stresses and extrapolate the velocity field, the physical parameters ρ , λ , μ have to be known at different locations inside one grid cell and, if the variations of these parameters are not known analytically, the values have to be interpolated.

5.5.2 Continuity condition across interfaces

In a realistic Earth model, away from a rupturing fault, the two most important boundary conditions are related to the Earth’s free surface and internal material discontinuities (interfaces).

When the simulation problems involve the Earth’s surface, the free-surface boundary condition (i.e. air/solid or air/water interface) has to be implemented. To consider the forces acting in a specific direction n_j normal to the interface given a space-dependent stress field σ_{ij} , the *traction* vector T_i is given by the Cauchy theorem as follows

$$T_i = \sigma_{ij}n_j \quad (5.37)$$

where n_j is a unitary vector. At the Earth’s free surface the boundary condition leads to perpendicular tractions equal to zero. The free surface boundary condition implies the existence of surface waves (a dominant feature in regional and global broadband

seismograms). Assuming the z -direction pointing upwards $\mathbf{n} = [0, 0, 1]$

$$\sigma_{xz} = \sigma_{yz} = \sigma_{zz} = 0 \quad (5.38)$$

Inside the Earth rapid changes of material parameters (e.g., layers discontinuities) may occur. The stratifications in sediments, the crust–mantle (Moho) discontinuity, the core–mantle boundary, or the inner-core boundary are the main examples. Due to lithostatic pressure such discontinuities can in most cases be treated as perfectly welded interfaces. Across such discontinuities, displacement and tractions are continuous. At the interface between two media 1 and 2 this condition can be expressed as

$$\begin{aligned} \sigma_{ij} n_j^{(1)} &= \sigma_{ij} n_j^{(2)} \\ u_i^{(1)} &= u_i^{(2)} \end{aligned} \quad (5.39)$$

In the case of an interface between two solid layers, both compressional and transverse components have to verify the continuity condition. For an interface between solid and liquid, the shear stresses must be zero, and the continuity is applied only to the normal component of the traction and displacement. If the interfaces are not parallel, the continuity conditions become more complex. As shown in Figure 5.7, at each point of the discretized interface, Eq. 5.38 and 5.39 have to be verified in the case of free-surface boundary and two-layers interface, respectively.

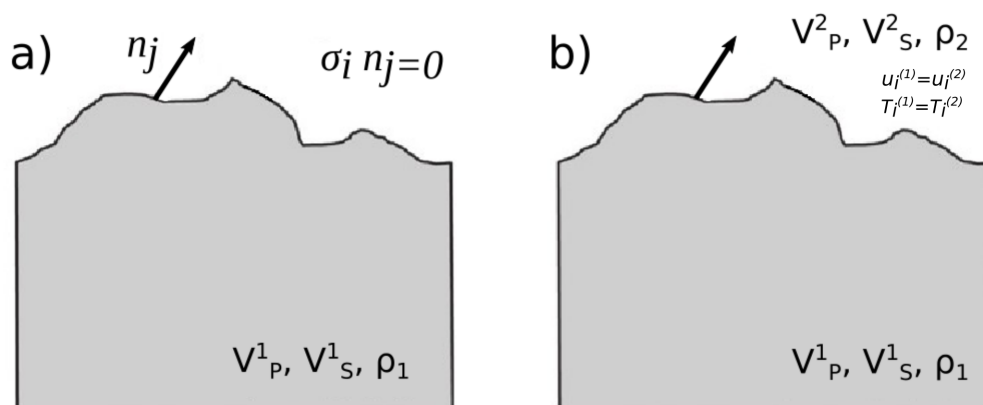


Figure 5.7: (a) Free-surface boundary condition in the presence of surface topography. (b) Across the two-layers interface with changing geophysical parameters, the boundary condition controls the continuity of traction and displacement.

Chapter 6

Open-source Seismic Wave Propagation Code

OpenSWPC (<http://github.com/takuto-maeda/OpenSWPC>) is a tool aimed at performing parallel numerical simulations of seismic wave propagation in a wide variety of targets. The code is designed to be implemented on supercomputers and is made accessible to users via input files to be fully open to the seismological community. The tool is developed based on a staggered-grid FDM code (Finite Difference Method, described in Chap. 5) to model seismic waves in 3D and 2D viscoelastic media on a local-to-regional scale. The necessary information to run simulations is defined in input text parameter files without modifying the code. The simulation results are seismograms and snapshots of the wavefield propagation. The outputs are given in NetCDF (Network Common Data Form) and Seismic Analysis Code (SAC) formats.

The staggered-grid FDM method for simulating seismic waves and the algorithms adopted in OpenSWPC is based on the theory for viscoelasticity and numerical algorithms explained in Moczo et al. (2014) and (Igel, 2017) (for more details see Chap. 5).

In the following sections, details on the code implementation are summarized according to the main reference (Maeda et al., 2017).

6.1 Wave equation and viscoelastic model

The FDM simulation of seismic wave propagation adopts the equation of motion of continuum mechanics using the velocity and stress formulation in the Cartesian coordi-

nate system (see Chapter 5)

$$\rho \frac{\partial v_i}{\partial t} = \sum_{j=1}^{N_D} \frac{\partial \sigma_{ij}}{\partial x_j} + f_i \quad (6.1)$$

where N_D is the model dimension (2 or 3), v_i is the particle velocity of the elastic motion in the i^{th} component, ρ is the density, σ_{ij} is the i, j^{th} component of the stress tensor and f_i is the i^{th} component of the body force. The two-dimensional case reproduces the motion of P-SV or SH polarization.

The waves propagate in heterogeneous viscoelastic media with frequency- independent attenuation. To describe the viscoelasticity, the code developers adopted the Generalized Zener Body (GZB, Fig. 6.1)(Maeda et al., 2013), which consists of a parallel connection of Zener bodies (introduced in Chap. 5) having different relaxation times to obtain nearly constant Q in a wide frequency range. The Zener body models the behaviour of a viscoelastic material using a linear combination of springs and dashpots to represent elastic and viscous components (Kelvin-Voigt model, see Chapter 5).

This viscoelastic body is described by the following relaxation functions for elastic moduli $\pi = \lambda + \mu$ and μ

$$\begin{aligned} \psi_\pi(t) &= \pi_R \left(1 - \frac{1}{N_M} \sum_{m=1}^{N_M} \left(1 - \frac{\tau_m^{\epsilon P}}{\tau_m^\sigma} \right) e^{-t/\tau_m^\sigma} \right) H(t) \\ \psi_\mu(t) &= \mu_R \left(1 - \frac{1}{N_M} \sum_{m=1}^{N_M} \left(1 - \frac{\tau_m^{\epsilon S}}{\tau_m^\sigma} \right) e^{-t/\tau_m^\sigma} \right) H(t) \end{aligned} \quad (6.2)$$

where N_M is the number of Zener bodies connected in parallel, τ_m^σ is the relaxation time of the m th body, $\pi_R = \lambda_R + 2\mu_R$ and μ_R are the relaxed moduli. $\tau_m^{\epsilon P}$ and $\tau_m^{\epsilon S}$ are the creep times of the two polarized waves. Connecting Zener bodies with different relaxation times allows to cover the wide frequency range of constant Q. The code provides the implementation of *memory variables* following the Robertsson et al. (1994) definition of viscoelasticity with the τ -method proposed by Blanch et al. (1995). This formulation is based on the constant ratio between the relaxation and creep times among

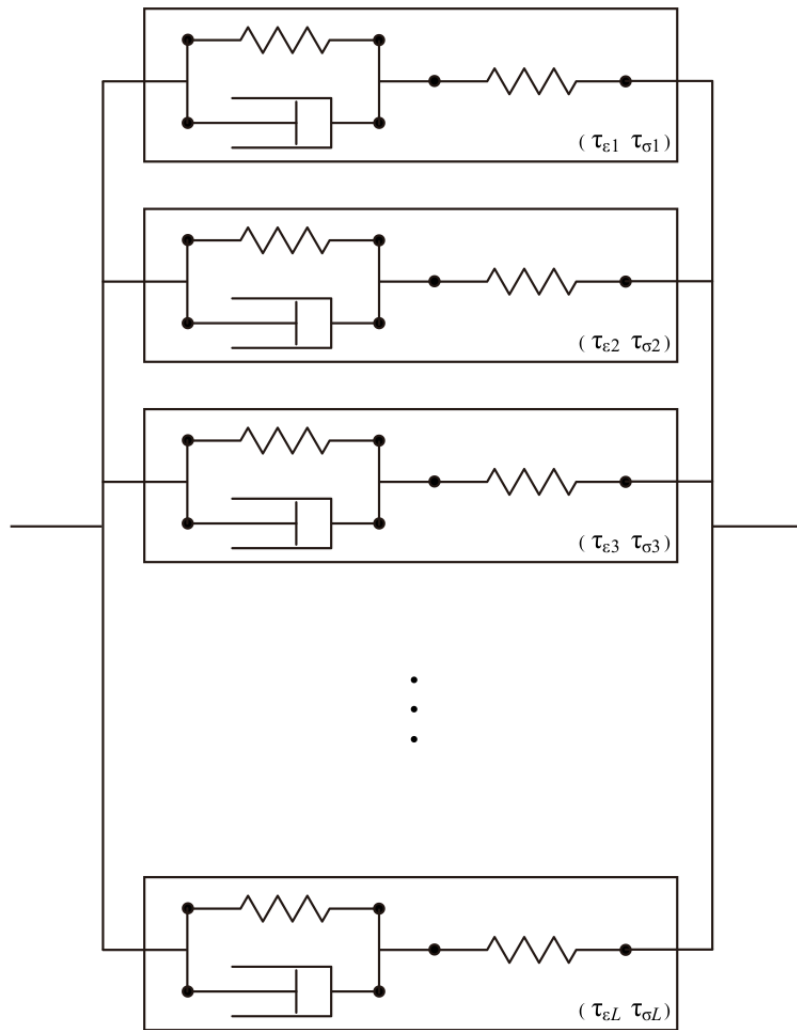


Figure 6.1: Implementation of parallel connection of Zener bodies (from Maeda et al., 2017)

all Zener bodies

$$\begin{aligned}\tau^P &= \frac{\tau_m^{\epsilon P}}{\tau_m^{\sigma}} - 1 \\ \tau^S &= \frac{\tau_m^{\epsilon S}}{\tau_m^{\sigma}} - 1\end{aligned}\tag{6.3}$$

From a given set of relaxation times, the method gives optimized values for the parameters τ^P and τ^S using the least-squares method, so that the quality factors for P and S waves become approximately constant over a given frequency range. The adopted model can yield an approximately constant Q over a broad frequency range below 2 Hz

using three Zener bodies ($N_m = 3$). Besides, the intrinsic attenuation of the P- and S-waves (Q_P and Q_S) can be defined independently and this will result in different creep times between the two elastic moduli.

Based on the τ method, the constitutive equation of the viscoelastic body can be written

$$\begin{aligned}
\sigma_{ij} &= [\dot{\psi}_\pi(t) - 2\dot{\psi}_\mu(t)] * \delta_{ij}\epsilon_{kk} + 2\dot{\psi}_\mu(t) * \epsilon_{ij} \\
\frac{\partial \sigma_{ii}}{\partial t} &= [(\lambda_R + 2\mu_R)(1 + \tau^P) - 2\mu_R(1 + \tau^S)] \\
&\quad \times \sum_{k=1}^3 \frac{\partial v_k}{\partial x_k} + 2\mu_R(1 + \tau^S) \frac{\partial v_i}{\partial x_i} + \sum_{m=1}^{N_M} r_{iim} \\
\frac{\partial \sigma_{ij}}{\partial t} &= \mu_R(1 + \tau^S) \left(\frac{\partial v_i}{\partial x_j} + \frac{\partial v_j}{\partial x_i} \right) + \sum_{m=1}^{N_M} r_{ijm}
\end{aligned} \tag{6.4}$$

where r_{ijm} is the memory variable of the (i, j)th component of the stress tensor and $\dot{\psi}$ is the derivative of the relaxation function (Eq. 6.2).

As a consequence of introducing the viscoelasticity, the phase velocity of the body waves become a function of the frequency due to the physical dispersion effect (Aki and Richards, 2002). Therefore, they follow the given velocity structure at a given reference frequency f_R .

6.2 Staggered-grid and stability conditions

The equation of motion and the derivative of the constitutive equations are solved numerically based on a staggered-grid FDM with fourth-order accuracy in space and second-order accuracy in time. The code adopts the Cartesian coordinate system with x and y as the horizontal directions and the vertical axis z was taken to be positive downward with average sea level height at $z = 0$. The unit volume illustrated in Fig.6.2 is defined as a ‘‘voxel’’ at the grid indices (I,J,K) and is equal to

$$\begin{aligned}
x_{beg} + (I - 1)\Delta x &< x \leq x_{beg} + I\Delta x \\
y_{beg} + (J - 1)\Delta y &< y \leq y_{beg} + J\Delta y \\
z_{beg} + (K - 1)\Delta z &< z \leq z_{beg} + K\Delta z
\end{aligned} \tag{6.5}$$

Figure 6.2 illustrates the staggered grid layout in the 3D case. The normal stress tensor components are defined at the center of the voxel, the shear stress is defined on the edge, and the velocity vector components are defined on its surface. All medium properties and parameters (λ_R , μ_R , ρ , τ_P , τ_S) are defined on the same grid as the normal stress components, at the center of the voxel at

$$\begin{aligned} x_{beg} + (I - 1/2)\Delta x \\ y_{beg} + (J - 1/2)\Delta y \\ z_{beg} + (K - 1/2)\Delta z \end{aligned} \quad (6.6)$$

The evaluation of the medium properties defined in the staggered-grid system requires appropriate averaging of the medium parameters defined on the neighbouring grids. Averaging the density on neighbouring grids is necessary when evaluating the velocity. Averaging the relaxed rigidity modulus is necessary when evaluating the shear stress components and the accompanying memory variables. The spatial grid width, Δx , Δy , Δz , and the time step width, Δt , must satisfy the stability condition, which is given in N_D dimensional space by

$$\Delta t < \frac{1}{V_{max}} \left(\sum_{i=1}^{N_D} \frac{1}{\Delta x_i^2} \right)^{-1/2} \left(\sum_{p=1}^{P/2} C_p \right)^{-1} \quad (6.7)$$

where V_{max} is the maximum velocity of the medium, C_p are the coefficients of the finite difference formula for the order of the finite difference method P, and Δx_i is the spatial grid width in the i-th direction. The code uses a fourth-order formula of the finite difference method with coefficients $C_1 = 9/8$ and $C_2 = 1/24$. For the fourth-order finite difference with isotropic grid sizes ($\Delta x = \Delta y = \Delta z = h$) in three-dimensional space, the stability condition becomes

$$\Delta t < \frac{6/7}{V_{max} \sqrt{\frac{1}{\Delta x^2} + \frac{1}{\Delta y^2} + \frac{1}{\Delta z^2}}} \simeq 0.495 \frac{h}{V_{max}} \quad (6.8)$$

The stability condition ensures that the distance that the seismic wave propagates within a single time step is much smaller than the spatial grid width. The numerical simulation will diverge if this condition is not satisfied. In addition, according to Carcione (2007), the maximum source frequency and minimum velocity should verify the following con-

straint on the grid spacing

$$h \simeq \frac{c_{min}}{2f_{max}} \quad (6.9)$$

i.e., the minimum wavelength of the simulated seismic waves should be much longer than the spatial grid width. If the wavelength becomes relatively small compared to this condition, a fictitious numerical dispersion will appear giving inaccurate later phases. The actual grid spacing depends on the FD scheme. An FD scheme for a fourth-order approximation in space and a second-order in time requires 5–8 grid points per minimum wavelength. To satisfy this condition, OpenSWPC takes the wavelength longer than 5–10 times the spatial grid width. Therefore, the minimum velocity (usually the S-wave velocity) in the velocity model should be selected carefully or a smaller spatial grid size can be selected. In this case, the time-step size must also be shortened to satisfy the stability condition.

The spatial grid size h controls the highest frequency allowed for the FDM simulation considering the minimum wave speed, v_{min} . The condition is

$$f_{max} = \frac{v_{min}}{7h} \quad (6.10)$$

namely, at least seven grid points per minimum wavelength are necessary to restrict the numerical dispersion of the FDM calculation within the required level. The maximum frequency of the 3D FDM, f_{max} , can be estimated by the size of the simulation, the minimum wave speed and the memory size of the computer M_{max}

$$f_{max} = \frac{v_{min}}{7} \left(\frac{M_R}{m_g SD} \right)^{1/3} \simeq \frac{v_{min}}{7} \left(\frac{M_{max}}{m_g SD} \right)^{1/3} \quad (6.11)$$

where S is the area of a surface and D is the depth of the simulation model. The required memory is 188 bytes per grid when using mixed-precision arithmetic calculations. For instance, considering a simulation on a regional scale with horizontal dimensions and a depth of 200km and assuming a minimum S-wave speed of 1.5 km/s, OpenSWPC can simulate a high-frequency seismic wavefield up to 2 and 10 Hz using the EIC (Earthquake Information Center system of the Earthquake Research Institute at the University of Tokyo) and the ES (Earth Simulator supercomputer of the Japan Agency for Marine–Earth Science and Technology) high-performance.

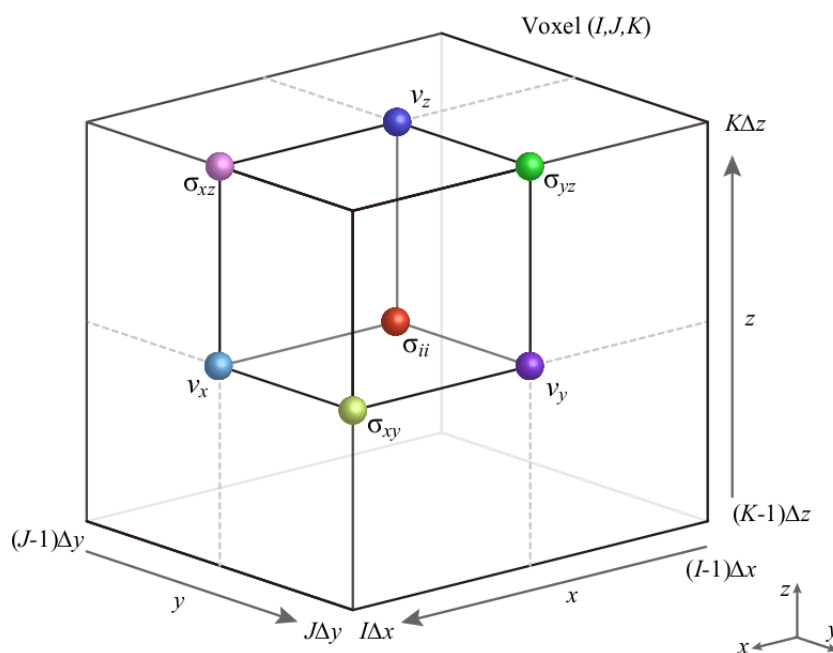


Figure 6.2: Staggered grid layout in 3D space.

6.3 Boundary condition

In OpenSWPC, the efficient Heterogeneity, Oceanic layer and Topography (HOT) FDM method (Nakamura et al., 2012) is used to implement the free surface and ocean bottom boundary conditions. It can correctly model seismic-wave propagation in media with a fluid–solid interface, including both land and ocean-bottom topographies. Placing the normal-stress components at the center of the voxel and the particle velocity and shear-stress components at the sides allows satisfying the boundary condition of vanishing shear stress on the fluid–solid interface by applying zero rigidity (ν) to the grid points of the shear-stress components. The boundary conditions have to balance the continuity of the normal components of particle velocities and stresses on the fluid–solid interface and the discontinuity of other components. Calculating Hooke’s law for an off-diagonal shear-stress component using a high-order finite-difference approximation across the interface in the staggered grid shows unsatisfactory differentiation across the fluid–solid interface. Applying the second-order approximation of Hooke’s law allows us to express the equations for each fluid and solid side separately. Nakamura et al. (2012) apply the second-order approximation for the equations around the fluid–solid

interface and the fourth-order in the fluid and the solid media except around the interface in the computational domain.

HOT-FDM is applied in regional-scale modelling of seismic wave propagation in coastal areas (e.g., Nakamura et al., 2012; Maeda and Furumura, 2013; Maeda et al., 2013), in high-frequency seismic wave simulations of topographic scattering (Takemura et al., 2015), and in samples (Yoshimitsu et al., 2016), demonstrating the ability of the HOT-FDM to include irregular topography and curved surfaces in FDM.

The air column is treated as a medium with a very small density and zero wave speeds for the P- and S-waves. It is treated as a vacuum where no seismic wave can propagate due to zero wave speeds. The ocean column is treated as an elastic medium having density $1.0[g/cm^3]$, P-wave speed $1.5[km/s]$ and S-wave speed $0.0[km/s]$. On the free surface and seafloor, a reduced, second-order FDM scheme is applied instead of the fourth-order FDM.

OpenSWPC develops absorbing boundary conditions surrounding the bounded model to avoid artificial reflections from the boundaries of the computational model. The developers implemented the Perfectly Matched Layer (PML) boundary condition (Zhang and Shen, 2010) and Cerjan's sponge (Cerjan et al., 1985) to minimize artificial reflections. This PML method solves the auxiliary differential equations in addition to the equations of motion and the constitutive equations in the absorbing zone with complex and frequency-shifted absorbing functions. The material in the PML zone is assumed to be perfectly elastic and the memory variables for the inelasticity are not calculated. The PML efficiently absorbs outgoing waves from the model, but it occasionally causes instabilities during the calculation, in particular when the seismic waves propagate in highly heterogeneous structures with very large velocity contrasts. The stable sponge boundary condition of Cerjan et al. (1985) is also implemented. It simply attenuates the waves in the absorbing layer by multiplying the stress and velocity components by small values in the absorbing zone at each time step. The sponge condition is perfectly stable but less efficient when absorbing outgoing waves.

6.4 Source implementation

The moment tensor, the body forces or the incidence of a plane wave are implemented in the code to simulate the seismic source depending on the environment (i.e., faults, volcanoes). The source description, based on the moment tensor, can be imple-

mented by couples of body forces or the stress discontinuity representation (Coutant et al., 1995). OpenSWPC adopts the stress discontinuity representation computing stress increments to implement the moment tensor. The seismic source can be implemented in OpenSWPC with a single point source or the user can implement a finite-fault source using multiple point sources (Graves and Wald, 2001; Takenaka and Fujii, 2008). The source mechanisms of the faulting are given by a six-component moment tensor or by three parameters of a double couple source (strike, dip, rake). The moment tensor is placed on the nearest grid point of the normal stress component. When updating the shear stress and velocity components, the source grid point is averaged with the neighbouring source grid points.

Instead of a moment tensor source, users can set the body forces to describe the source. The three-component force vector (f_x, f_y, f_z) should be specified. The body forces implementation has the same source time functions settings as in the case of the moment tensor source.

The moment rate function can be chosen among the given six bell-like functions such as boxcar, triangle and cosine functions, Herrmann's quadratic function (Herrmann, 1979) and Küpper's wavelet (Mavroeidis and Papageorgiou, 2003). The required parameters are the functions starting time T_0 , duration T_R and total moment M_0 . The functions have a common cutoff frequency, which is a reciprocal of the source duration time, but have different roll-offs above the cutoff frequency.

A plane wave of plane P- or S-waves incident from the bottom is also implemented as an input source instead of the moment tensor or body force sources. The plane-wave incidence uses a solution of the up-going wave of the 1D wave equation in a homogeneous medium as an initial condition of the velocity and stress components at the bottom of the model. The specification of the initial conditions includes the depth of the initial plane wave and its characteristic wavelength, the strike and dip angle of the plane wave and the polarization direction in the case of an S-wave. The depth dependence of the wave amplitude is determined by the source time functions used in the moment rate function as a function of space. Via the definition of the source time function, the integration of the initial plane wave along the propagation direction will be normalized to 1. A bell-like-shaped spatial distribution corresponding to the source time function is assumed as initial conditions.

6.5 Velocity model and small-scale random inhomogeneity

The velocity model can be set as a uniform or a layered homogeneous medium, or curved interfaces can be implemented. Neither a depth nor lateral velocity gradient is implemented but users can set as many interfaces as it needs. The velocity structure input model is given by implementing interfaces depth via NetCDF files (Network Common Data Form). The bathymetry and topography include the effects of free surface and oceanic layer. Each layer is defined by density, P-wave velocity, S-wave velocity, Q_P , Q_S . If the depth of the ground surface is deeper than zero, the depth range from $z = 0$ to the surface is assumed to be an ocean layer. The grid above the free surface is treated as an air column.

In addition, for each layer, a different randomly inhomogeneous medium can be overlaid into the model. Small-scale velocity inhomogeneities can be specified with power-law spectra on the background velocity models. The small-scale velocity inhomogeneity ξ is defined by external files. From the average velocities V_{P_0} , V_{S_0} , and ρ_0 , the fluctuated velocities and density are defined as follows

$$\begin{aligned} V_P &= V_{P_0}(1 + \xi) \\ V_S &= V_{S_0}(1 + \xi) \\ \rho &= \rho_0(1 + \nu\xi) \end{aligned} \tag{6.12}$$

where $\nu = 0.8$ is a scaling parameter based on a laboratory experiment (Sato et al., 2012). At each grid location, the velocity fluctuation $\xi(I, J, K)$ is defined. The code automatically reads the corresponding volume from the file. If the computational size (Nx,Ny,Nz) is larger than the random media file size, the media is used repeatedly by applying a circular boundary condition. The simulation codes do not care if the grid sizes of the simulation and the input random media file are identical.

Chapter 7

Earthquake characteristics and structural properties of the Southern Tyrrhenian basin from full seismic wave simulations

In seismic tomography, the response of seismic wavefields to sharp lateral variations in medium properties, especially crustal discontinuity, is a relevant aspect as discussed in Chap. 4. Back-arc basins, characterized by mixed continental-oceanic crust and high-absorption magmatic systems linked to subduction, like the Southern Tyrrhenian basin (Sartori, 2003), are challenging environments for full-waveform and adjoint tomography techniques (Blom et al., 2020; Magnoni et al., 2022). These settings distort seismic wavefields significantly, dispersing high-frequency information; as a consequence, standard inversions of phases and amplitudes measured on the recorded wavefield produce inconsistent results (Cormier and Sanborn, 2019). Only low-frequency (< 3 Hz) waveforms are consistently recorded across oceanic basins at the regional scale. However, these waves show resonant scattering properties caused by their strong interactions with large-scale velocity discontinuities of sizes comparable with seismic wavelengths (Cormier and Sanborn, 2019). In this case, strong reverberations (dominated by surface-wave) and scattering due to larger-scale structures (Gabrielli et al., 2020) become primary controllers of the seismic wavefield, and especially of coda waves (i.e., wave-trains following a crustal phase). At the regional scale, the effects of crustal structural variations (e.g., the presence of a thin crustal pinch) turn out to be crucial in imaging the Earth subsurface at ~ 1 Hz (Morozov and Safarshahi, 2020). Close to this frequency, strong scattering from the Moho (Sanborn et al., 2017; Sanborn and Cormier, 2018) and loss of energy due to leakage into the mantle (Wegler, 2005; Margerin, 2017) trade-off with the standard description of wave attenuation as a combination of scattering

and absorption (Morozov and Safarshahi, 2020), as demonstrated by modelling of seismic envelopes (Nardoni et al., 2021, - Chap. 4). Discriminating stochastic signatures produced by highly scattering and absorption media from coherent reverberations due to shallow Moho is thus key for full-waveform reconstructions (Fichtner et al., 2009), which have the potential of increasing resolution exponentially in oceanic settings.

Several works developed in both lithospheric and magmatic settings demonstrate the feasibility of describing wavefields with joint RTT and wave-equation based modelling. Joint coherent and radiative-transfer forward modelling focuses on seismic amplitudes (Przybilla et al., 2006; Obermann et al., 2013; Gabrielli et al., 2020). It provides ideal constraints to wave-equation modelling on the quantities with the highest trade-offs across 3D basins: P-wave, S-wave, and early S-coda amplitudes (Sanborn et al., 2017; Sanborn and Cormier, 2018; Cormier and Sanborn, 2019; Nardoni et al., 2021). Recent advances in modelling implement the interaction between Rayleigh and body waves during scattering by including the contribution of the fundamental mode surface wave (Xu et al., 2022). Solving the major drawback of previous radiative-transfer simulations makes them a credible stand-alone alternative to wave-equation modelling. However, wave-equation simulations remain the primary modelling strategy in seismology. Full-waveform-based forward and inverse methods can account for the full physics of 3-D wave propagation (Chen et al., 2007; Fichtner et al., 2009; Romanowicz et al., 2020). Seismic tomography generally focuses on travel times of a limited number of seismic phases: this approach speeds up the forward computation. Seismic phases such as surface waves or teleseismic P and S waves are easy to isolate on seismograms and are the most considered phases in global tomography applications. This approach leaves a large part of the information contained in seismic records unexploited. Full waveform inversions enable the investigation of every phase in the seismogram. Methods based on seismic full-waveform inversion aim at characterizing the properties of the Earth's subsurface by exploiting information throughout the whole recorded seismic waveforms. Applications were made possible from regional (Chen et al., 2007; Fichtner et al., 2009) to global scale (French and Romanowicz, 2014; Bozdağ et al., 2016). Recent advances in parallel computing and numerical methods enable large-scale 3D numerical simulations of the seismic wavefield by taking advantage of fast computing codes that are adaptable to the studied area (Komatitsch et al., 2010; Maeda et al., 2017; Magnoni et al., 2022). These simulations can tackle fundamental mode surface waves and the topography effects directly (Takemura et al., 2015), accounting for the complete physics

of 3D wave propagation (Chen et al., 2007; Fichtner et al., 2009; Romanowicz et al., 2020).

The Italian peninsula and the back-arc Tyrrhenian basin are ideal for testing and discriminating the potential of full-waveform modelling across basins. This basin is the result of multi-stage extension following the Ionian slab rollback (Malinverno and Ryan, 1986; Doglioni et al., 1999; Faccenna et al., 2001; Lo Bue et al., 2021). Its irregular extension has supposedly entrapped the Issel Bridge (Sartori, 2003; Cocchi et al., 2009) (a portion of thinned continental crust) within the Vavilov and Marsili volcanic centres. Extended seismic networks (Fig. 7.1) have already enabled the use of state-of-the-art full-waveform codes to image the lithosphere across the Mediterranean (Blom et al., 2020). In this region, the Moho has been studied primarily using receiver functions (Piana Agostinetti and Amato, 2009; Di Stefano et al., 2011), while more recent estimations of Moho depth come from noise-based surface-wave imaging (Manu-Marfo et al., 2019). The station coverage in the region remains too scarce to discriminate the Moho variations across the bridge and at the interface between the basin and continental crust (Manu-Marfo et al., 2019; Nardoni et al., 2021; Magrini et al., 2022).

Previous coda-attenuation imaging and radiative-transport-based forward modelling across this area (Nardoni et al., 2021, see Chap. 4) can inform wave-equation modelling, reducing uncertainties on most structural features. OpenSWPC (Maeda et al., 2017, see also Chap. 6), a wave-equation finite-difference code, is the ideal tool to include the radiative transfer models as a-priori information. Developed by the *heterogeneous Earth community* (Sato et al., 2012) and tailored to work in high-attenuation and high-contrast lithospheric media, OpenSWPC includes statistical fluctuations in velocity and heterogeneous topography, typical of a mixed oceanic and continental crust. This approach can estimate earthquake source characteristics, sediment thickness and Moho depths using regional earthquakes, offering an alternative to techniques that use single phases and wave packets (Piana Agostinetti and Amato, 2009; Di Stefano et al., 2011; Tinti et al., 2016).

Furumura and Kennett (1997) investigated the propagation of regional seismic phases and assessed their sensitivity to crustal structures. Alvarado et al. (2007) performed forward waveform modelling to sample the crust, finding out that synthetic regional seismograms (epicentral distances from 100 to 350 km) are sensitive to crustal parameters, especially crustal thickness. In the frequency band 0-2 Hz, Fu et al. (2002) investigated the energy attenuation of regional phases across a randomly rough topography via

numerical modelling, showing that topographic scattering attenuates regional waves. Irregular topography and its stochastic fluctuations disperse reverberating phases, biasing Moho depth estimates Takemura et al. (2015). After topography has been included in the modelling, reverberating phases like Lg-wave present in the S-coda (Sens-Schönfelder et al., 2009) become an additional tool for the estimation of Moho depths across basins using regional earthquakes. Being able to develop source and crustal models, the full-waveform-based technique has the potential to better couple with geodynamic models of the evolution of the Tyrrhenian basin, allowing to connect seismic models to what leads to such Moho variations.

The high-velocity contrast at the Moho and the interference of other phases, such as lower crustal (Pg) and upper mantle (Pn) phases, with the critically reflected Moho rays (PmP) can generate dramatic changes in the amplitude and phase of reflected waves, requiring a non-linear description, especially for wide-aperture acquisitions (Guo et al., 2021). Different misfit functions for full-waveform inversion, as correlation analyses, can assess non-linearity associated with mixing phase and amplitude information (Bozdağ et al., 2011). Inversion procedures can then explore different techniques from linearized (Fichtner et al., 2008) to non-linear approaches (Fichtner et al., 2009; Guo et al., 2021) depending on the observed waves and phases. Before using full-waveform inversions, we thus need to establish the sensitivity of direct and coda waveforms to the complexity of basins. In Section 7.2, we present the simulation tool employed for the finite-difference solution to the wave propagation and the simulation setup. The sensitivity of the full-wavefield can be assessed on a limited number of models available in literature through qualitative comparisons with single source-station data (Secs. 7.2.2-7.2.3) and broader correlation analysis (Lee et al., 2014; Schwardt et al., 2020) (Sec. 7.3.2) on the spatial array surrounding the basin (Fig. 7.1) by using wave-equation modelling.

7.1 Methods for retrieving Moho depth: previous applications across the Tyrrhenian basin

The central part of the Mediterranean region has been studied mainly using the receiver function method (Piana Agostinetti and Amato, 2009; Di Stefano et al., 2011). Previous CROP studies provided a limited view of the Moho interface due to the few crustal profiles obtained from reflected/refracted data across the Italian peninsula and

the Tyrrhenian basin (Scrocca et al., 2003; Finetti, 2003). Mapping the Moho interface is a key point for geodynamic modelling to understand the evolution and state of the lithosphere. Imaging this depth range allows to gain resolution for the upper mantle structure models. The link with the rheology is also significant as it outlines the presence of relevant structures affecting the wave propagation (e.g volcanism, thermal gradient).

The receiver-function technique uses teleseismic data. Teleseismic receiver function methods use P to SV waves converted at sharp seismic discontinuities beneath the seismic receiver. The target phases are better isolated and observed at epicentral distances between 35° and 95° in the coda of P waves. A time-domain deconvolution of the horizontal components (radial and transverse) by the vertical one (Langston, 1979) is applied to the broadband seismograms. The procedure aims to isolate P to SV mode conversions at the velocity contrast interface that is associated with crust and mantle seismic discontinuities near the receivers. Teleseismic receiver functions (RF) are used to locally determine the depth and dip of crustal and upper mantle discontinuities (Piana Agostinetti and Amato, 2009). RF demonstrate to be an excellent method to constrain depth and dip of first-order seismic discontinuities beneath three-component seismic stations (Langston, 1979; Van Der Meijde et al., 2003; Piana Agostinetti and Amato, 2009; Di Stefano et al., 2011). The accuracy of the estimations may be of the order of 5 km and depends on the quality of the waveforms, the coverage of the data set (azimuth and distance distribution), and the complexity of the lithosphere structure beneath the receiver (Di Stefano et al., 2011). This uncertainty is significant, especially if we need high resolution in complex regions and in the absence of receivers such as ocean-bottom seismometers.

Other estimations of Moho depth come from surface waves studies. Surface waves dispersion measurement is sensitive to absolute shear wave velocities, while it yields low resolution in constraining discontinuities. For this reason, when dealing with surface waves, the Moho interface is taken as the values of the bottom depth of the lower crustal layers (Manu-Marfo et al., 2019). Based on the complex tectonic and evolution of the lithospheric structure underneath the Tyrrhenian basin, using the 4.2 km/s velocity contour to define the Moho interface could bias the estimation and yield inconsistent results. Manu-Marfo et al. (2019) determined the Moho depth by picking where the probability of a strong discontinuity occurs at a certain shear velocity on the 1-D velocity depth profile. They estimated S-wave velocity from the dispersion data using a

fully non-linear Bayesian approach to compute the 1D shear velocity profiles and their uncertainties. From posterior probability density for the position of discontinuities, they selected the velocity value for the most feasible Moho depth.

This thesis addresses the feasibility of using full regional seismograms to map the Moho discontinuity valuating firstly the sensitivity of head wave and crustal reverberating waves to the depth variations. On a regional scale, the seismic phases are influenced by crustal thickness. Performing simulations of the waves propagation, Furumura and Kennett (1997) investigated the propagation of regional seismic phases in different crustal settings. One of the phases showing high sensitivity to crustal structures is the Lg wave, which consists of multiple S-wave reverberations propagating with a velocity of 3.5km/s in the crust. The authors found that the decrease of the Lg energy is reinforced by anelastic attenuation across sediments as well as the presence of a gradually thinning crustal waveguide, i.e. a shallow Moho interface. Besides, the Pg phase (i.e., multiple P-wave reverberations inside the crust) is considerably weakened by propagating across a thinning crust, and Lg is reduced in amplitude due to energy leaked into the uppermost mantle from the Moho pinch. Pg conversions are also produced from the slope as the Moho returns deeper. Several studies (Shapiro et al., 1996; Furumura and Kennett, 1997; Baumgardt, 2001) assessed that a major contribution to the blockage of Lg waves comes from thick sediments and the crustal thinning reinforces Lg attenuation by reflecting S energy from the crystalline crust into the sediments. The Lg wavefield emerging on the far side of the crustal pinch is thus distorted by scattering processes and the loss of energy due to attenuation or by leakage into the upper mantle. The wavefield modelling of regional seismograms could thus discriminate the change in the shape of the crustal waveguide.

7.2 Simulation Method

We use the Open-source Seismic Wave Propagation Code (OpenSWPC, Maeda et al., 2017) to model seismic waves in a 3D isotropic viscoelastic medium at the regional scale. The numerical simulation based on parallel computing solves the equations of motion described by the velocity and stress components in the 3D Cartesian coordinate system with viscoelastic constitutive equations, using a finite difference method (as

introduced in Chap. 6)

$$\rho \frac{\partial v_i}{\partial t} = \sum_{j=1}^{N_D} \frac{\partial \sigma_{ij}}{\partial x_j} + f_i \quad (7.1)$$

$$\sigma_{ij} = [\dot{\psi}_\pi(t) - 2\dot{\psi}_\mu(t)] * \delta_{ij} \epsilon_{kk} + 2\dot{\psi}_\mu(t) * \epsilon_{ij}.$$

The code is equipped with a frequency-independent attenuation model based on the generalized Zener body and an efficient perfectly matched layer for absorbing boundary conditions. A heterogeneous velocity model can be introduced as the code already includes the statistical fluctuations that affect seismic wave propagation at the regional scale. The code allows users to conduct seismic wave propagation simulations that explicitly target media with mixed oceanic and continental crust: a crucial advantage over other codes for these specific settings.

7.2.1 Set up

The model covers the area of the Tyrrhenian basin and the Italian peninsula (Fig. 7.1). The volume used for the 3D simulation is 600 km by 750 km in the horizontal plane and 130 km in depth. It is discretized with a grid spacing of 0.5 km in the horizontal and vertical directions. Due to the simulation grid and the cluster memory, the maximum frequency of the synthetic wavefield is 0.33Hz.

The initial layered model is built using the data available for the topography (Amante and Eakins, 2009), sediments and Moho discontinuity (Manu-Marfo et al., 2019). We set the initial crustal model based on the Moho values obtained by Manu-Marfo et al. (2019). The radiative transfer envelope modelling across the Southern Tyrrhenian basin (Nardoni et al., 2021) confirms the inference of Manu-Marfo et al. (2019), who highlighted a thinner oceanic crust across this area. The radiative transfer simulations also provide the best model velocities, intrinsic attenuation, velocity fluctuations ε and scale lengths a (Tab. 7.1). We used ε , a and a Von Kármán distribution function to implement stochastic random heterogeneities in the crustal structure. The heterogeneities are kept fixed, while the velocity of each layer has been varied to fit phases arrivals and amplitudes (Tab. 7.2). We locate the seismic receivers using the INGV network coordinates (Fig.7.1). To test the sensitivity of the full-wavefield to velocity and source variations (see Secs. 7.2.2- 7.2.3), we consider the station located in Sicily across the north-south profile, shown in Fig.7.1.

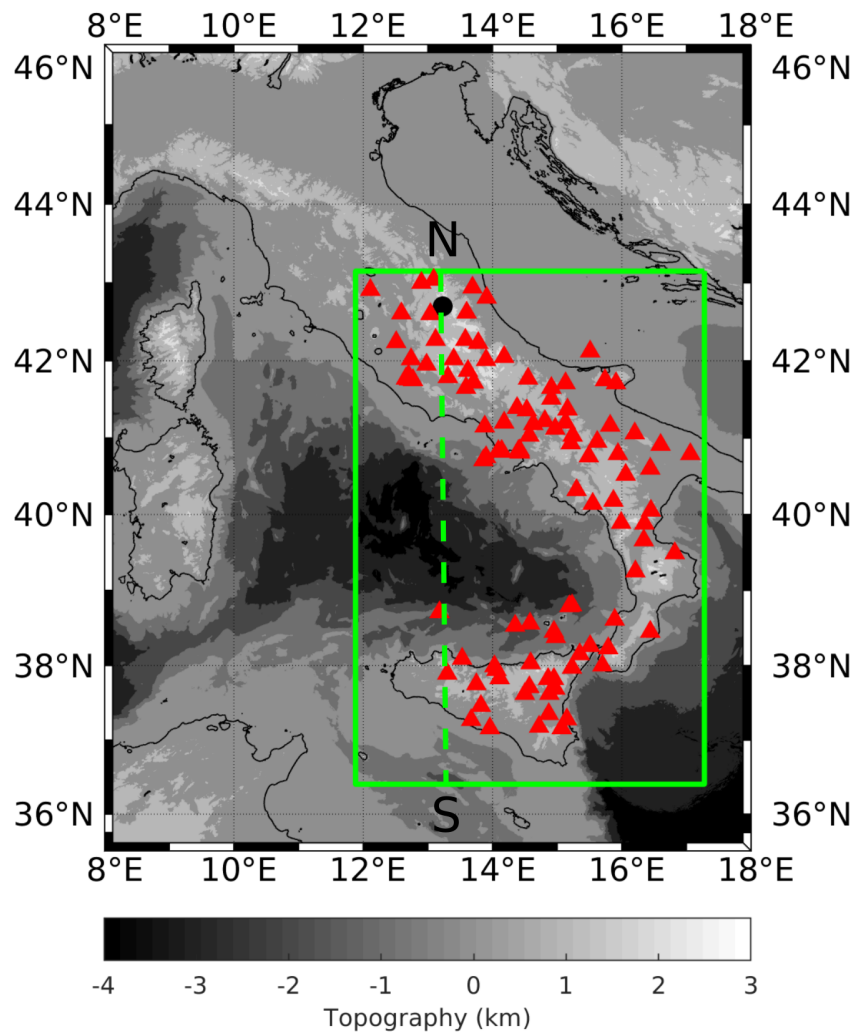


Figure 7.1: The input 3D medium covers the area highlighted in green. The black dot is the modelled source, and the red triangles indicate the locations of the receiver in the simulation. The dashed green line represents the north-south profile (AA' in Fig. 4.9) taken as a reference to characterize the seismic source and velocity profiles and visualize the correlation between the data and the synthetic data corresponding to different Moho depths.

7.2.2 Source Implementation and Starting Models

We implement a seismic source corresponding to the earthquake that occurred in Accumoli (central Italy, 2016) and characterized by a constant magnitude M_w 6.1 (Tinti

| Starting Earth Model | V_P [km/s] | V_S [km/s] | ρ [g/cm ³] | Q_P | Q_S | ε | k | a |
|------------------------|--------------------------------------|--------------|--|------------------|------------------|---------------|-----|-----|
| Air | 0.0 | 0.0 | 0.001 | 10 ¹⁰ | 10 ¹⁰ | | | |
| Seawater | 1.5 | 0.0 | 1.0 | 10 ⁶ | 10 ⁶ | | | |
| Sediments | 5.22 | 2.9 | 2.2 | 1000 | 500 | 0.07 | 0.2 | 0.2 |
| Crust | 6.0 | 3.9 | 2.8 | 2000 | 1500 | 0.07 | 0.3 | 0.2 |
| Moho Transition | 7.0 | 4.0 | 3.4 | 1000 | 500 | 0.01 | 0.4 | 0.2 |
| Mantle | 7.7 | 4.5 | 3.5 | 1000 | 500 | 0.01 | 0.5 | 0.2 |
| Starting Source Models | Depth [km] | | Strike, Dip, Rake | | MRF | Rise Time [s] | | |
| | 6.45 (Tinti et al., 2016) | | | | | | | |
| Source A | 7.3 (Tinti et al., 2016) 8 (INGV) | | 155, 49, -87 (INGV) | | boxcar | 4 | | |
| Source B | 7.3 | | 155, 49, -87 (INGV) 165, 49, -78 (USGS) 145, 38, -101 (GCMT) | | boxcar | 4 | | |
| Source C | 7.3 | | 155, 49, -87 (INGV) | | boxcar | 4 8 | | |
| Source D | 7.3 | | 155, 49, -87 (INGV) | | triangle | 4 8 | | |

Table 7.1: Starting models. Starting model for P-wave velocity (V_P), S-wave velocity (V_S), density (ρ) and inelastic attenuation (Q_P and Q_S) are listed for each layer. The values of ε , k and a are used to describe the velocity perturbation field in OpenSWPC. This starting model is derived from the results of Nardoni et al. (2021): the Moho depth is set according to Manu-Marfo et al. (2019) and the sediments are 2km thick across the continental region. The implemented starting source models are obtained by varying the depth, the focal mechanism, the moment rate function (MRF) and the rise time.

et al., 2016). The moment tensor is computed from the strike, dip, and rake values, describing the focal mechanism. The earthquake source is assumed point-like, as the wavelengths are longer than the fault dimensions and much shorter than the source-receiver distance (Aki and Richards, 2002).

Several studies estimated the source parameters assuming different moment rate functions (MRFs, Tinti et al., 2005; Cirella et al., 2018; Supino et al., 2019) to describe the fault displacement duration (rise time) and velocity. Tinti et al. (2016) modelled the fault slip velocity by imposing a boxcar source-time function (7.2a). Nevertheless, several choices can be made to model the source kinematics assuming a triangle, Kupper or t-exp type functions (Tinti et al., 2005; Cirella et al., 2018; Supino et al., 2019). The MRFs duration and shape affect the synthetic seismogram envelope (Takemura et al., 2020; Krischer et al., 2017). We test the source kinematics assuming both a boxcar and

triangle functions and explore different source parameters (i.e., hypocentral depth, focal mechanism and rise time), keeping fixed the magnitude M_w at 6.1 according to Tinti et al. (2016). The OpenSWPC forward simulations allow the evaluation of the source properties from the fit with real data recorded across a source-receiver path (Takemura et al., 2020). This fit is performed both qualitatively, by looking at recordings and synthetics, and quantitatively, by single-waveform and 2D spatial correlation analysis (Lee et al., 2014; Schwardt et al., 2020).

We define different source models (Tab. 7.1) by varying the focal depth, the focal mechanism, the moment rate function and the rise time separately in each model. This analysis is performed for the station located in Sicily across the profile north-south shown in Fig.7.1 (dashed green line) and for the vertical component. Tinti et al. (2016) and Cirella et al. (2018) obtained an average rise time smaller than 2 s for each sub-faults of the modelled fault of the Accumuli earthquake. As the majority of the seismic moment is released between 2 and 6 s, we set the boxcar function with rise time $T_R = 4$ s (Tinti et al., 2016). We vary the hypocentral depth (relative to the sea level), strike, dip, and rake separately, based on previous studies (Tinti et al., 2016, INGV Istituto Nazionale di Geofisica e Vulcanologia, GCMT Global Centroid Moment Tensor Catalog, USGS Earthquake Hazards Program) (Source A and B, Table 7.1). The changes in earthquake depths are primarily observed on S-wave phases, with minimal changes in P- and coda arrivals (Fig. 7.3). We select a depth of 7.3 km as it best fits the peak ground S-wave velocity (computed using the phase envelope, Fig. 7.3c). Among the three proposed radiation patterns, the USGS estimation appears most inconsistent with the synthetic waveforms and is excluded from further analyses (Fig. 7.4). Again, we select the INGV estimate, which shows the best fit to the S-wave peak ground velocity.

The wavefield primarily depends on the source time function shape (Takemura et al., 2020). Synthetic seismograms were thus obtained using both the boxcar (Fig. 7.5 - Source C in Tab. 7.1) and the triangle (Fig. 7.6 - Source D) functions for different rise times. To keep constant the function integral corresponding to the seismic moment M_0 , the height of the triangle is double the height of the boxcar function. Source duration effects (Matsuzawa et al., 2009; Krischer et al., 2017) produce a decrease in seismogram amplitudes and smoothing with time as the duration of the source increases. Only direct waves are usually considered in the estimation of source characteristics. Therefore, we set as the source model a boxcar function with an initial duration of $T_R = 4$ s (Fig. 7.5).

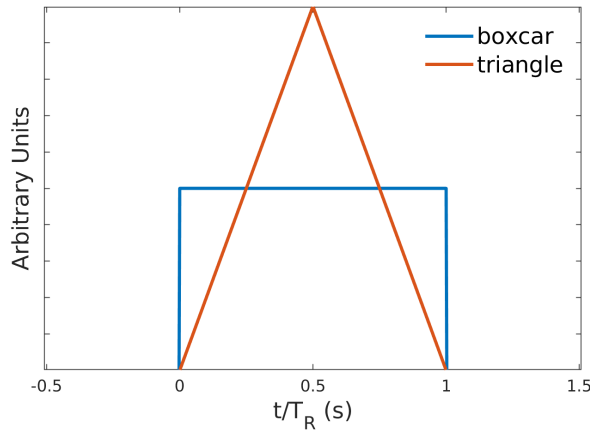


Figure 7.2: Boxcar and triangle moment rate functions used to describe the seismic source and to compare the synthetic wavefields.

7.2.3 Starting velocity and sediments models

After setting the starting source parameters fitting at best compressional and regional phases amplitude, we investigate how the larger-scale variability in crustal structure affects the seismic wavefield (Furumura and Kennett, 2019). We explore the effects of structural models differing from the starting model (compare Tables 7.1 and 7.2)) performing a sensitivity analysis focused on velocity variations and interfaces. These structural models were proposed by Nardoni et al. (2021) (see Chap. 4) based on radiative-transfer simulations. The source-station geometry (north-south) allows the discrimination of radial (north-south) from transverse (west-east) components easily.

7.3 Results

Based on the comparison between different velocity models, Fig. 7.7a shows the best agreements between the synthetic and recorded phases (see Fig. 7.8 for the other models). As expected, the P-phase (head wave) on the north-south and vertical components shows sensitivity exclusively to the P-wave velocity (V_P) variations for the crust and mantle. The vertically-polarized S wave (SV) is more difficult to detect on radial and vertical components as reverberations between the free surface and the Moho increase P coda. This is the likely explanation of the difference in phase and amplitude on north-south and vertical components between data and synthetics around 150s (Fig. 7.7a). Instead, we can satisfactorily reproduce the arrival of the east-west component,

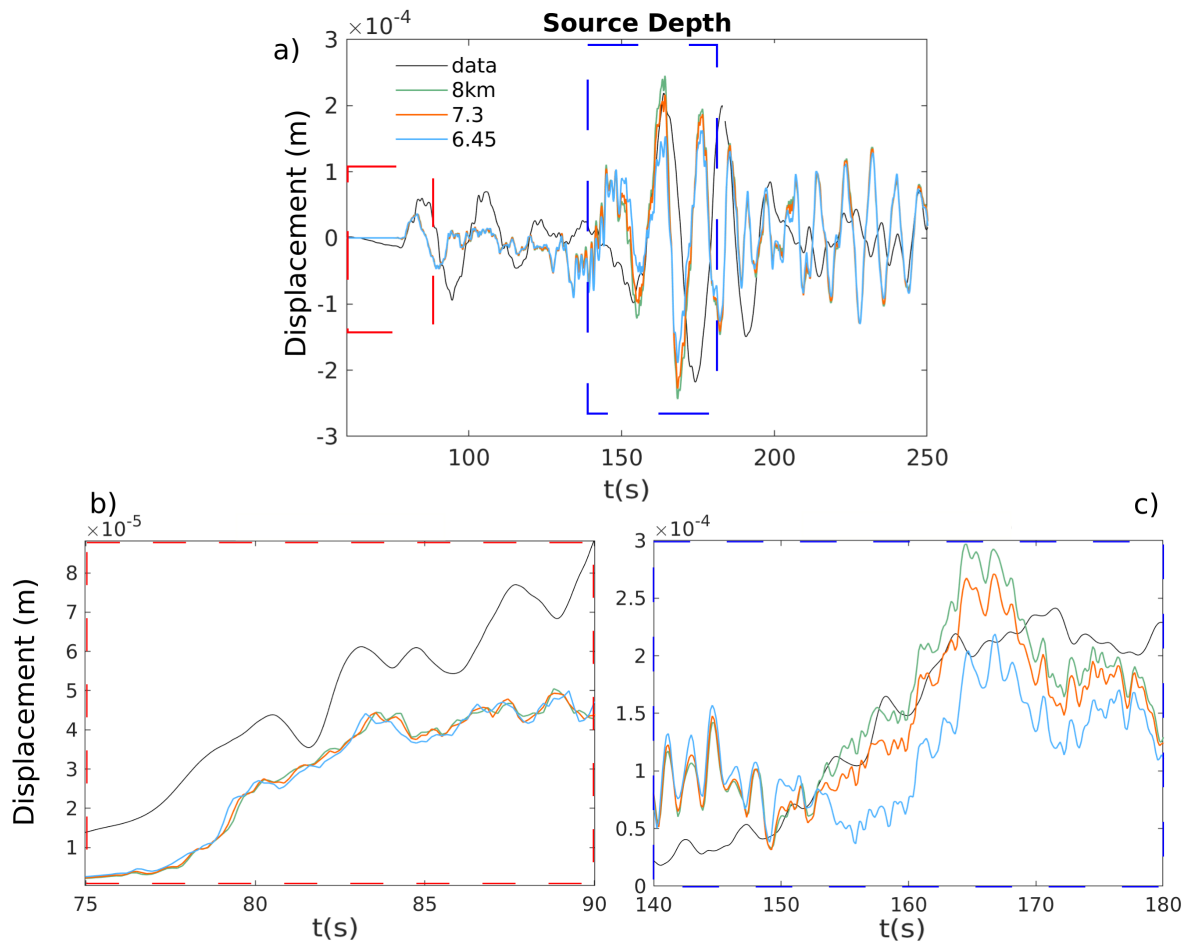


Figure 7.3: Source A (Tab. 7.1). (a): comparison between the station recording and the synthetic waveforms that are obtained using different focal depths. The boxcar is set with a rise time of 4s. (b)-(c): enlargement of the two insets in panel (a). They show the comparison between envelopes in the two time windows corresponding to compressional waves arrival and from S-wave arrival, respectively (dashed red and blue lines).

which best describes the horizontally-polarized S wave (SH). The primary controller of the east-west waveforms is thus the S-wave velocity V_S in the crust and the mantle. Velocity model 1.3 (Fig. 7.7), corresponding to higher V_P and lower V_S velocity in the crust, yields the best fit between the recordings and the synthetic seismograms for both P- and S-waves.

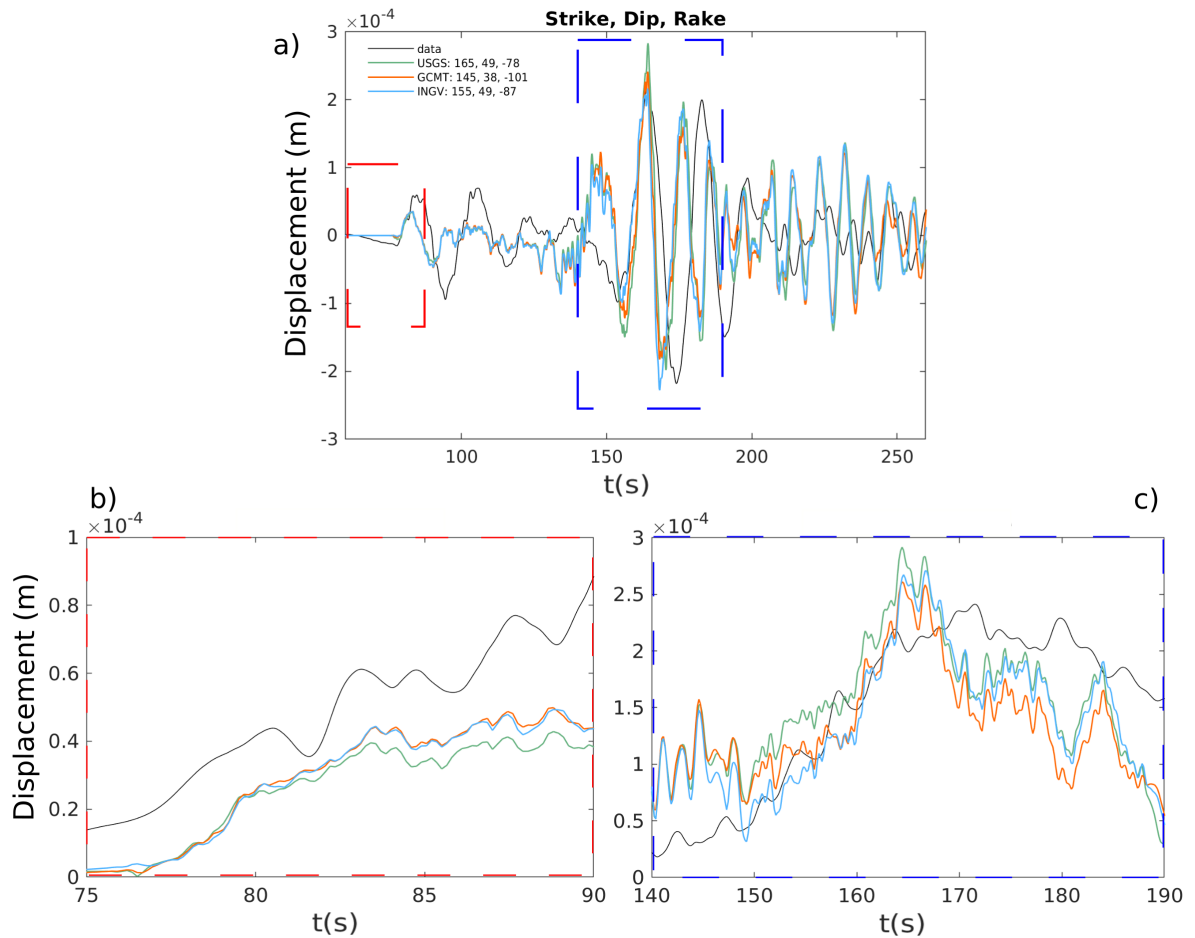


Figure 7.4: Source B (Tab. 7.1). (a): comparison between the station recording and the synthetic waveforms that are obtained using different focal mechanisms. The boxcar is set with a rise time of 4s and the focal depth is 7.3 km. (b)-(c): enlargement of the two insets in panel (a). They show the comparison between envelopes in the two time windows corresponding to compressional waves arrival and from S-wave arrival, respectively (dashed red and blue lines).

7.3.1 Sensitivity of the coda to sediments and adjustment of rise-time variations

Model 1.3 does not reproduce coda amplitudes, which have shown greater sensitivity to sediments (Nardoni et al., 2021) and are also affected by changes in source rise times (Fig. 7.5). We thus model the effects of sediments thickness variations on the full-waveform (Fig. 7.7b-c). A thick sedimentary layer primarily affects the S-coda wave-packet propagating and reverberating inside the crust by delaying the amplitude

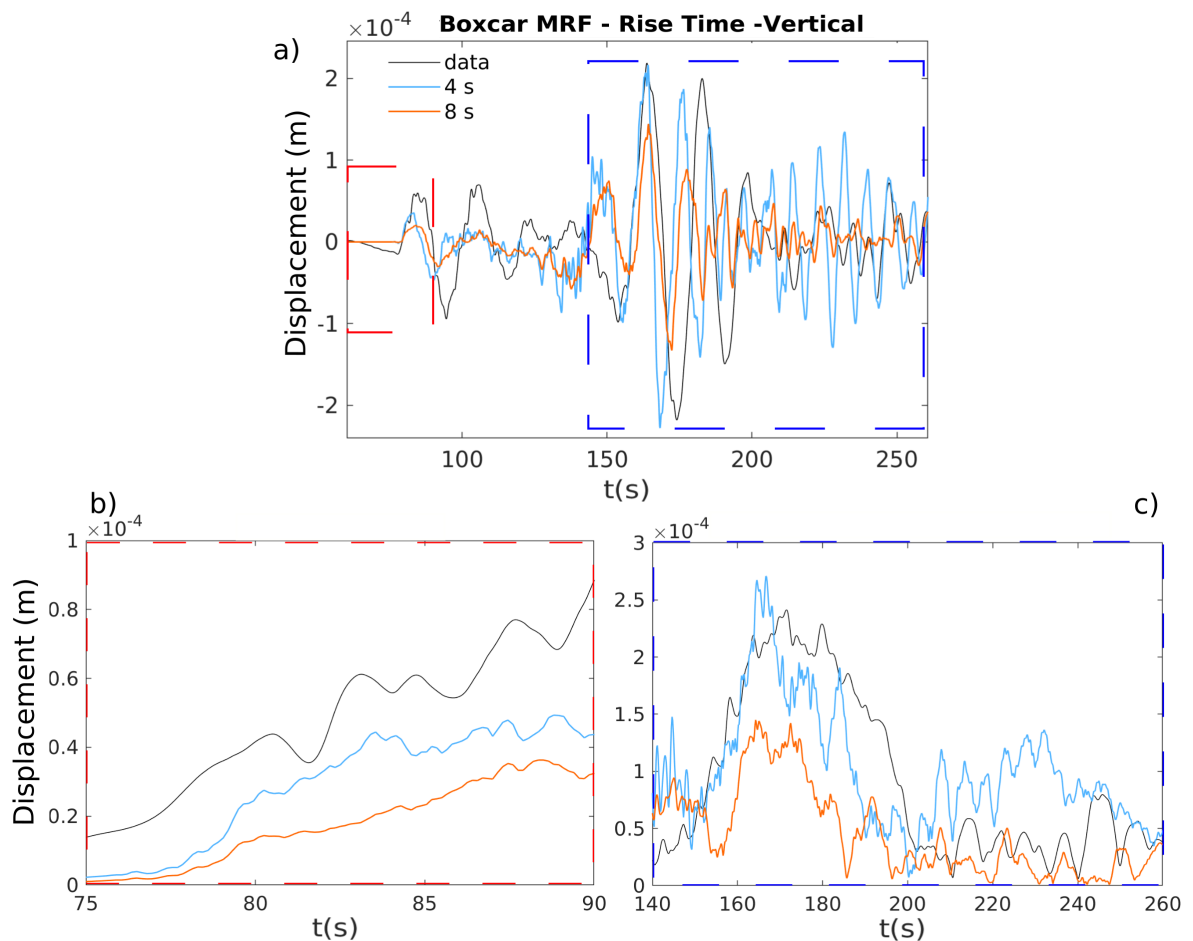


Figure 7.5: Source C (Tab. 7.1). (a): comparison between the station recording and the synthetic waveforms that are obtained using different rise times for the boxcar source time function. The depth is set to 7.3 km. (b)-(c): enlargement of the two insets in panel (a). They show the comparison between envelopes in the two time windows corresponding to compressional waves arrival and from S-wave arrival, respectively (dashed red and blue lines).

peak (Borleanu et al., 2017). Thinner sediments instead dampen coda reverberations (Fig. 7.7b), with the east-west component most sensitive to small sediments thickness variations. For a thicker sedimentary cover (Molinari and Morelli, 2011) and low P and S velocities, a mixture of Lg and crustal phases dominate the later part of the seismogram (Fig. 7.7c) (Sens-Schönfelder et al., 2009). Given the effects of the sediments thickness and velocity and the previous indication for the region (Moskalenko, 1992; Pepe et al., 2005; Pontevivo and Panza, 2006), thinner sediments (velocity Model 1.3 - Tab. 7.2) appear to characterize the continental areas. At the same time, there is no

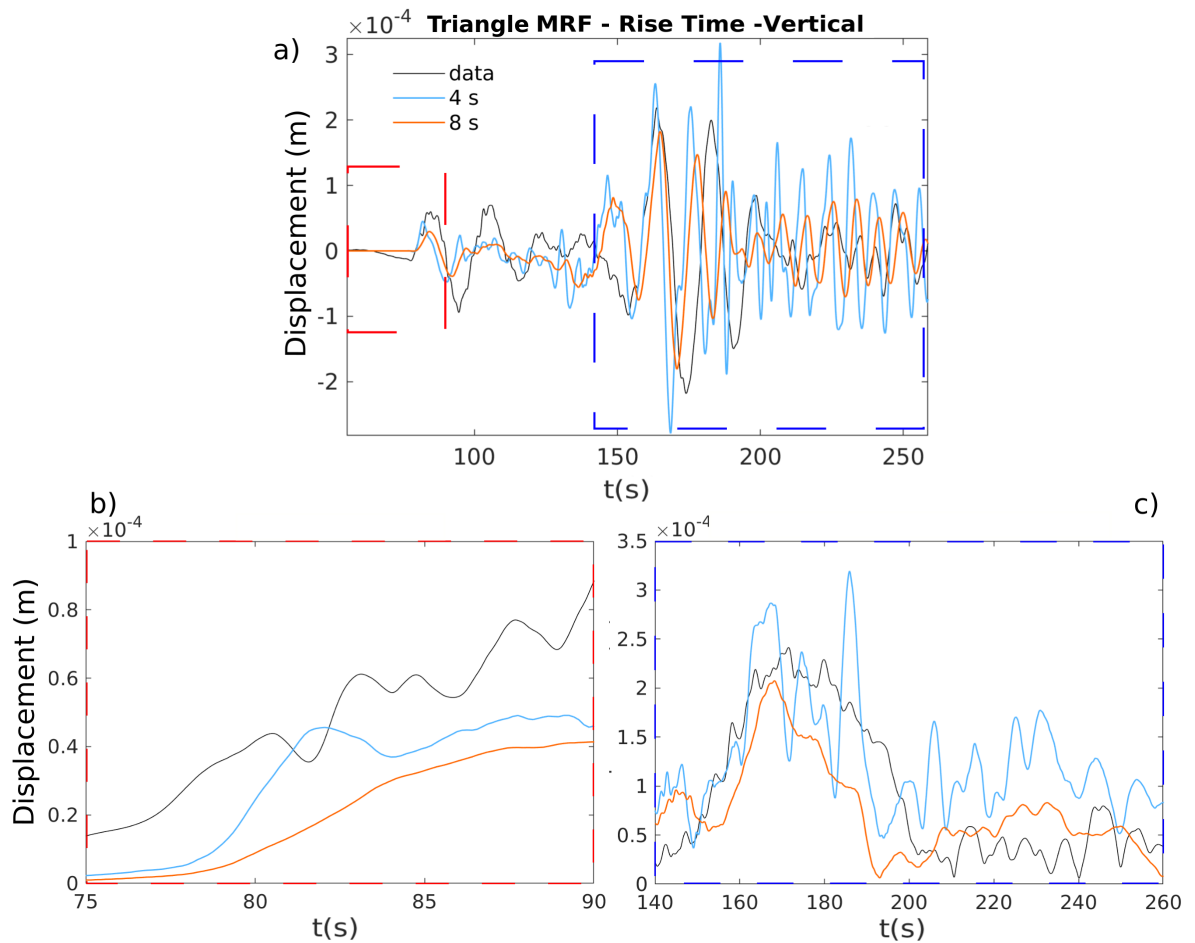


Figure 7.6: Source D (Tab. 7.1). (a): comparison between the station recording and the synthetic waveforms that are obtained using different rise times for the triangle source time function. The depth is set to 7.3 km. (b)-(c): enlargement of the two insets in panel (a). They show the comparison between envelopes in the two time windows corresponding to compressional waves arrival and from S-wave arrival, respectively (dashed red and blue lines).

sedimentary cover detectable under the sea at these frequencies. However, two km of sediments for the continental crust do not give a good fit for the coda amplitude (Fig. 7.7c). We thus decreased their quality factor and thickness (from 2 to 1 km) across the continental crust according to the results of Nardoni et al. (2021) (Fig. 7.9).

These variations do not change the P- and S-wavefields as much as the rise time of the source time function (compare Figs. 7.5 - 7.10) but drastically improve coda-wave reconstructions. So far, we selected the best rise time in the starting source model by looking at direct phases without considering the coda as a relevant observable. In

| Velocity Models | Model 1 | | Model 1.1 | | Model 1.2 | | Model 1.3 | |
|-----------------|---------|-------|-----------|-------|-----------|-------|-----------|-------|
| | V_P | V_S | V_P | V_S | V_P | V_S | V_P | V_S |
| Sediments | 5.2 | 2.9 | 4.9 | 2.9 | 5.0 | 2.8 | 5.0 | 2.8 |
| Crust | 6.0 | 3.9 | 6.0 | 3.8 | 6.4 | 3.9 | 6.4 | 3.5 |
| Moho Transition | 7.0 | 4.0 | 7.0 | 4.0 | 7.5 | 4.3 | 7.5 | 4.3 |
| Mantle | 7.7 | 4.5 | 7.7 | 4.5 | 7.7 | 4.5 | 7.7 | 4.5 |

| Final model | | | | |
|-------------|------------|-------------------|--------|---------------|
| Source | Depth [km] | Strike, Dip, Rake | MRF | Rise Time [s] |
| | 7.3 | 155, 49, -87 | boxcar | 6 |

| | Velocity | Q_P | Q_S |
|-----------------|-----------|-------|-------|
| Sediments | Model 1.3 | 600 | 250 |
| Crust | | 700 | 400 |
| Moho Transition | | 800 | 500 |
| Mantle | | 800 | 500 |

Table 7.2: Different velocity (km/s) models that are implemented in the initial structural model, keeping fixed the quality factor, velocity fluctuations, Moho and sediments thickness (Tab. 7.1). Below, the final Earth and Source model obtained from the source and velocity sensitivity analysis.

Fig. 7.10, we used velocity model 1.3, thinner sediments and lower quality factor while changing the moment rate function duration. Setting the best velocity model for the phase arrivals, we show that the coda is very sensitive to the duration of the moment rate function. In the final model (Tab. 7.2) used to estimate Moho variations, the rise time is thus set to 6 s for Model 1.3 (Tab. 7.2). This source model allows a good fit for both direct phase arrivals and coda amplitudes.

7.3.2 Sensitivity to the Moho

As the lateral heterogeneity of the Moho is the other relevant factor affecting wave propagation, different crustal models are also implemented. The results are compared by varying the thickness of the crust. We implement different Moho models, including those estimated by Manu-Marfo et al. (2019) and Molinari and Morelli (2011) (EPcrust) (Figure 7.11). Across the oceanic basin, the models revealed a thinner crust across the Tyrrhenian sea, giving values of about 10 km of Moho depth. However, a region separating the two oceanic sub-basins, the Marsili basin in the East and the Vavilov basin in the West, has been geologically identified as a portion of continental crust (Issel bridge - Sartori (2003)). Assuming that the Vavilov and Marsili Plains are separated by

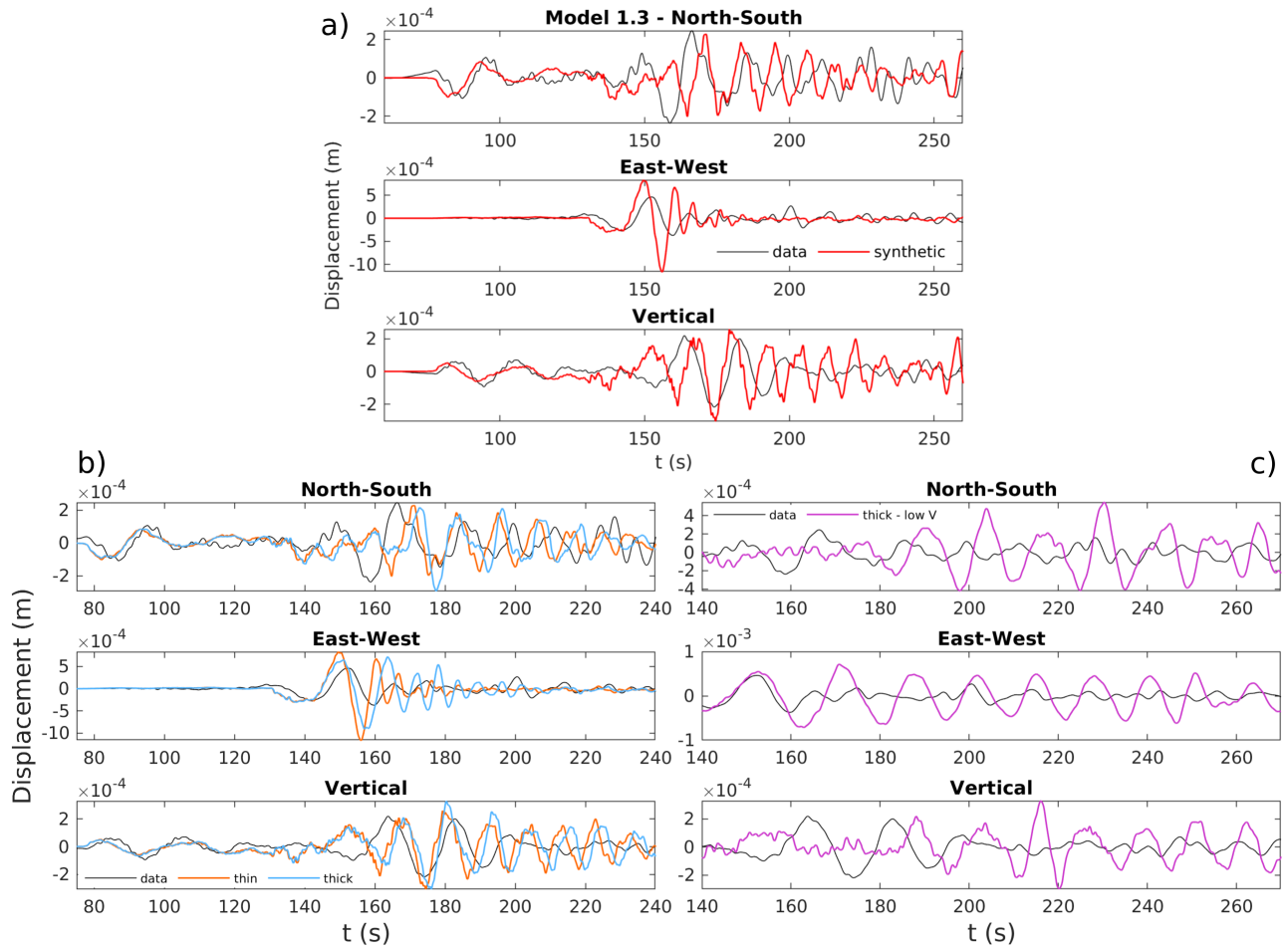


Figure 7.7: (a) Comparison of the three seismogram components with the synthetic waveforms obtained implementing velocity Model 1.3. Layers velocity is shown in Tab. 7.2. The crust thickness is set according to Manu-Marfo et al. (2019), the sediments are 2 km thick below the continental regions and there are no sediments below the sea (as explained in section 7.2.1). (b) Comparison between synthetic seismograms obtained for 2km of sediments (red) and thicker sedimentary cover (4-5km - blue) set according to Molinari and Morelli (2011) (Model 2), assuming velocity Model 1.3. (c) Comparison between synthetic seismograms obtained for sediments thickness as in Model 2, where the sediment layer is characterized by low velocities, $V_P = 2.9$ km/s and $V_S = 1.5$ km/s. The black waveforms are the receiver recordings.

a thicker continental crustal, we implement two other crustal models by deepening the depth of the Moho of the EPcrust model across the southern Tyrrhenian Sea. Figure 7.11 shows the cross-section of the crust for the four Moho models along the north-south profile in Fig. 7.1.

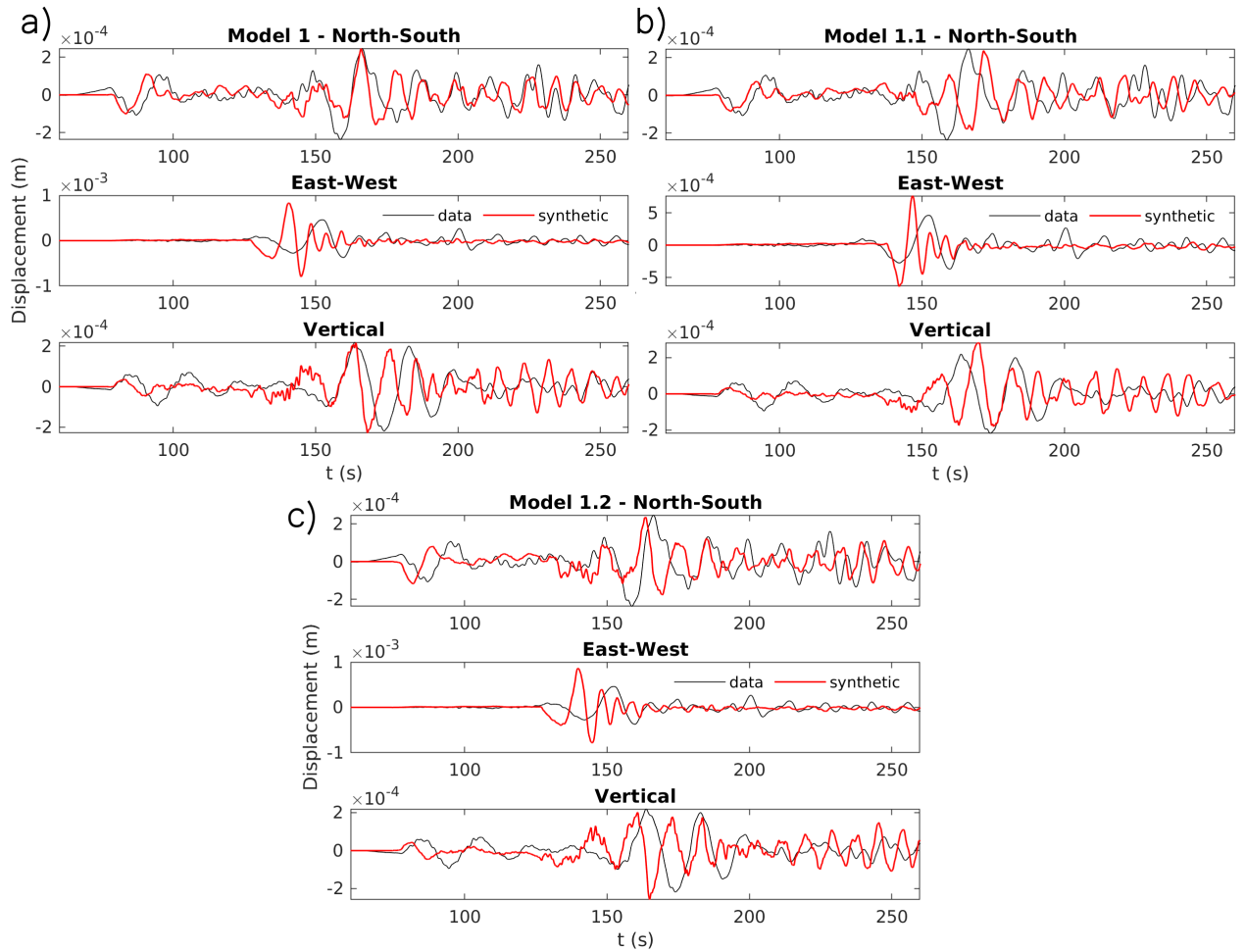


Figure 7.8: Comparison of the three seismogram components with the synthetic waveforms obtained implementing different velocity models. Layers velocity is shown in Tab. 7.1. The crust thickness is set according to Manu-Marfo et al. (2019), the sediments are 2 km thick below the continental regions and there are no sediments below the sea (as explained in section 7.2.1).

Figure 7.12 reports a comparison between synthetic seismograms obtained for the thicker and thinner crustal models at the station in Sicily with the model including an 18-km deep Moho in the centre of the basin (MohoEP18). The comparison is performed in the P- and S-coda time windows, comprised between the origin time and a lapse time of up to 200 s. The corresponding correlation coefficients discriminate the effects of the crustal depth variations, identifying the 18-km-deep Moho as best. An increase in the oceanic crust thickness leads to delayed arrivals on the three components (Fig. 7.12). As the propagation is mainly north-south (Fig. 7.1), the east-west component isolates

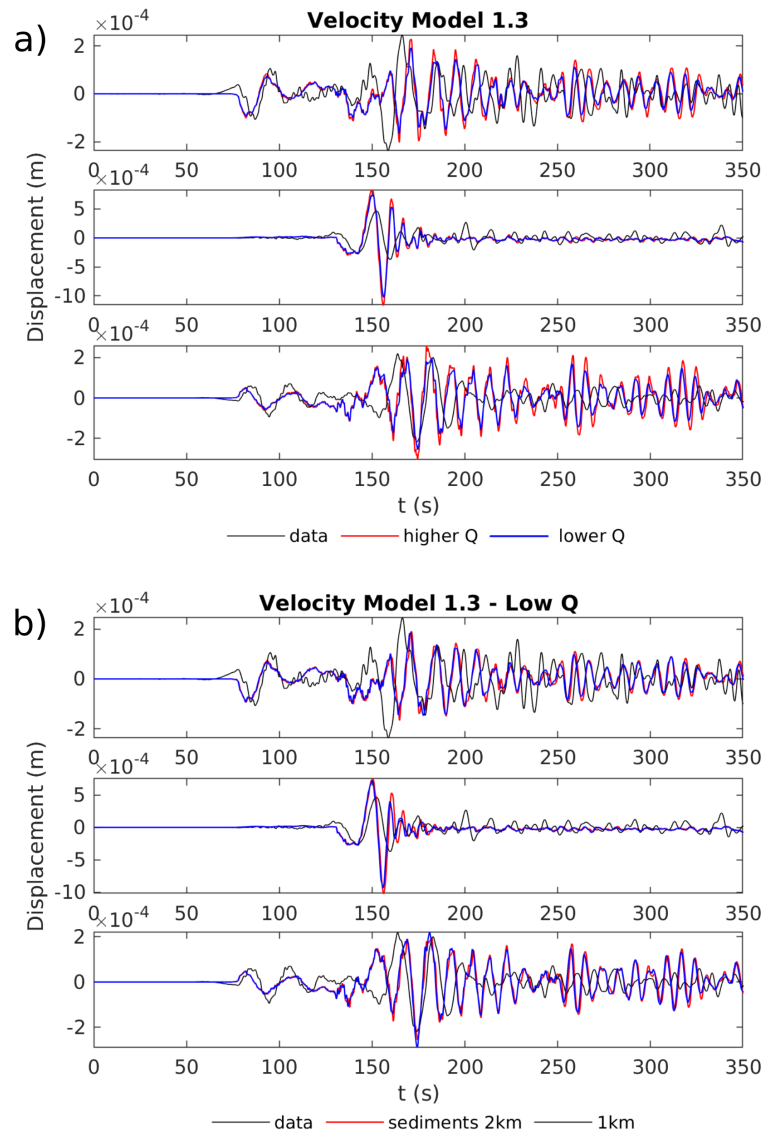


Figure 7.9: Effects of the variations of the P and S waves quality factors (a) and the thickness of the sediments (b) on the waveforms amplitude. From the top below, the seismograms correspond to north-south, east-west and vertical components, respectively.

the SH waves and is reproduced effectively (Fig. 7.7).

Wave polarization helps discriminate the effects of a horizontal interface such as the Moho for the peculiar geometry of the chosen north-south propagation. To perform a similar correlation analysis at the INGV network, we rotate all WE and SN seismic components, obtaining radial and transverse components for each source-station path (Fig. 7.12). For each station in Fig. 7.1, the synthetic seismogram is then compared to data

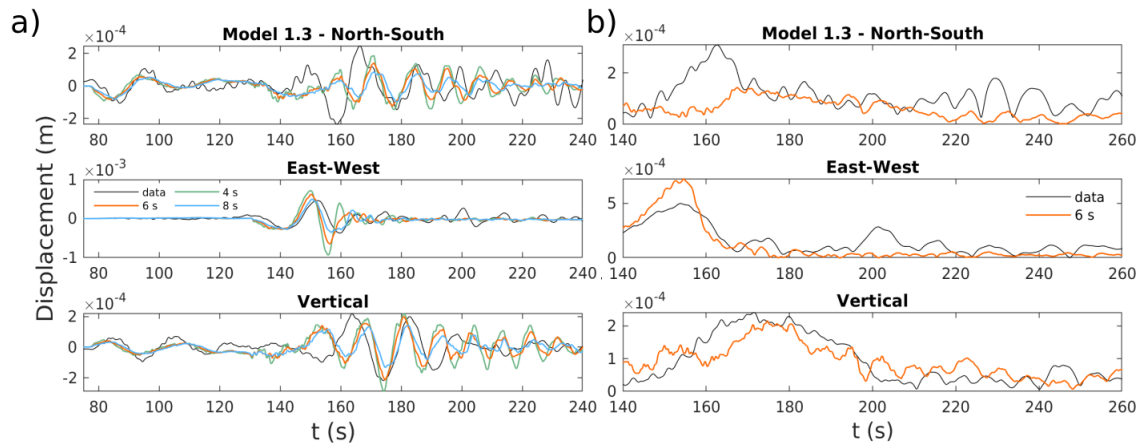


Figure 7.10: (a) Effects of different rise times assuming velocity Model 1.3. (b) Comparison between envelopes of the recordings and the synthetic seismograms for a rise time of 6s. From the top below, the seismograms correspond to north-south, east-west and vertical components, respectively.

(Figs. 7.12 and 7.13). We estimate the correlation coefficients in the time window 0-200s after filtering the seismograms in the frequency band 0.05-0.33Hz and compare the results with the other two available Moho models for the basin (Molinari and Morelli, 2011; Manu-Marfo et al., 2019). The correlation is mapped in the space with a regionalization approach, averaging the coefficients corresponding to different ray paths and crossing each cell (Fig. 7.14).

7.3.3 Comparison between flat and realistic interfaces: topography and correlation analysis.

Because the free surface plays a relevant role in the propagation of regional phases as Lg and Rg, we created three two-layered crustal models by varying the flat-Moho depth and modelled the wavefield in the case of a flat free-surface and the topography (ETOPO1 - Amante and Eakins, 2009). Figure 7.15 shows the results of the wavefield simulations for the radial, transverse and vertical components. The topography has marginal effects on the transverse component and all direct phase arrivals and amplitudes; however, it substantially changes the early coda of radial and vertical components, damping and dispersing Moho reverberations increasing late coda amplitudes. Topography is thus included in the final models.

The qualitative and quantitative comparison between different, realistic Moho models is necessary for defining a quantitative procedure to constrain the depth of the dis-

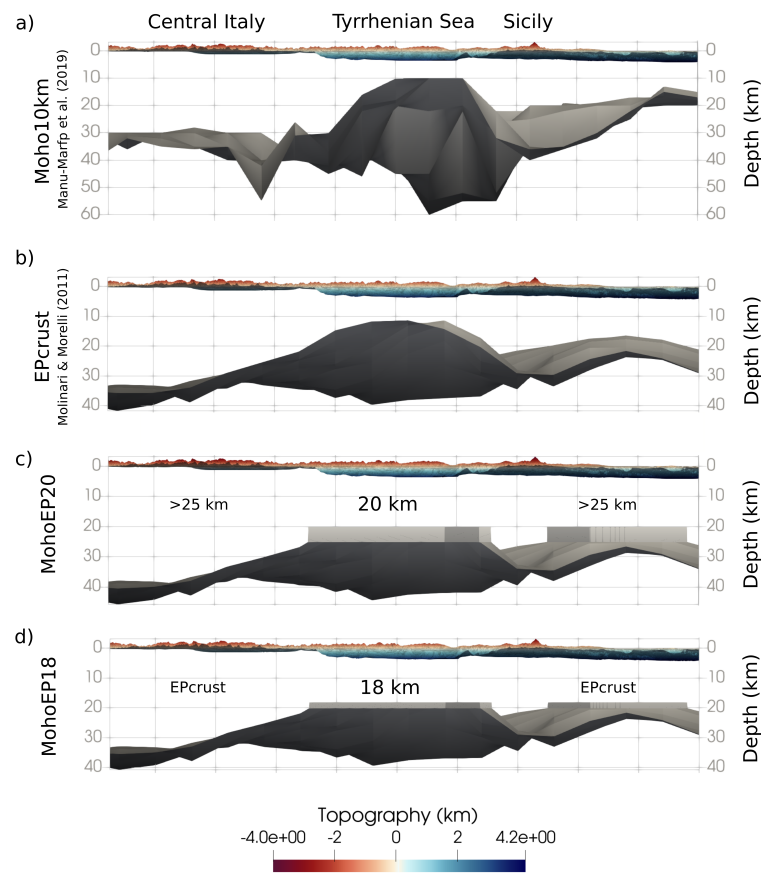


Figure 7.11: The crustal sections correspond to the NS profile in Fig. 7.1, showing the topography and the Moho models that are implemented in the simulations. (a) Moho10km (Manu-Marfo et al., 2019); (b) EPcrust (Molinari and Morelli, 2011); (c) MohoEP20km: depth values taken from EPcrust model are increased across both the oceanic and continental crust; (d) MohoEP18: depth values taken from EPcrust model are increased across the oceanic crust.

continuity through the inversion of a single source-station receiver. Then, we performed additional simulations using flat Moho models and estimated the correlation coefficient between the synthetic seismograms (those obtained for the flat interfaces and the MohoEP18 cases) and the recordings. The three components are divided into two time-windows (Fig. 7.12). The first window comprises the compressional arrival (i.e., the P head wave), while the second includes the S-wave and the following crustal, reverberating and converted waves. Figure 7.12 also shows the correlation coefficients obtained by comparing the data with synthetic models obtained embedding a crustal pinch between the basin and Sicily (Fig. 7.12a) and two flat Moho depths at 10 km and 30 km (Fig.

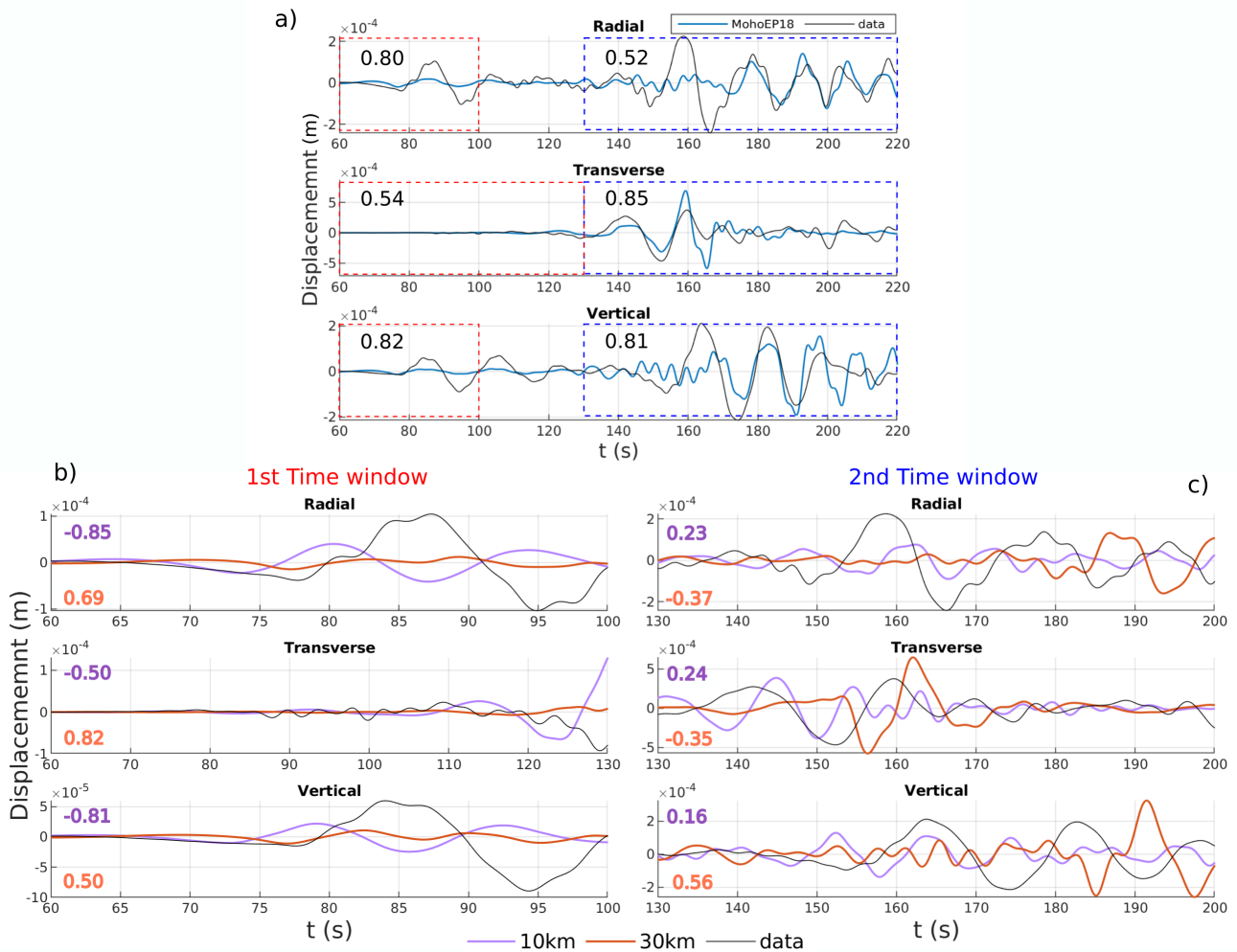


Figure 7.12: (a): Comparison between the recordings and the best Moho model, MohoEP18 (Fig. 7.11), for each seismogram component recorded at the station in Sicily. (b)-(c): comparison between the synthetic seismograms obtained for a crustal model with/without the pinch and the recordings in two time-windows corresponding to compressional arrivals and crustal phases, respectively. The data are filtered in the frequency band 0.05-0.33Hz. The numbers indicate the correlation coefficients between the data and the three synthetic seismograms corresponding to the pinch model (blu waveform in panel (a)), the flat 10km and 30km Moho (violet and red waveforms in panels (b)-(c)).

7.12b,c). These tests are initially computed only for the station directly south of the earthquake source in Sicily. The correlation coefficients computed in the two time windows clarify how a pinch is necessary to fit low-frequency data for this source-station path (Fig. 7.12a).

We performed the final correlation analysis at all the array stations using a single

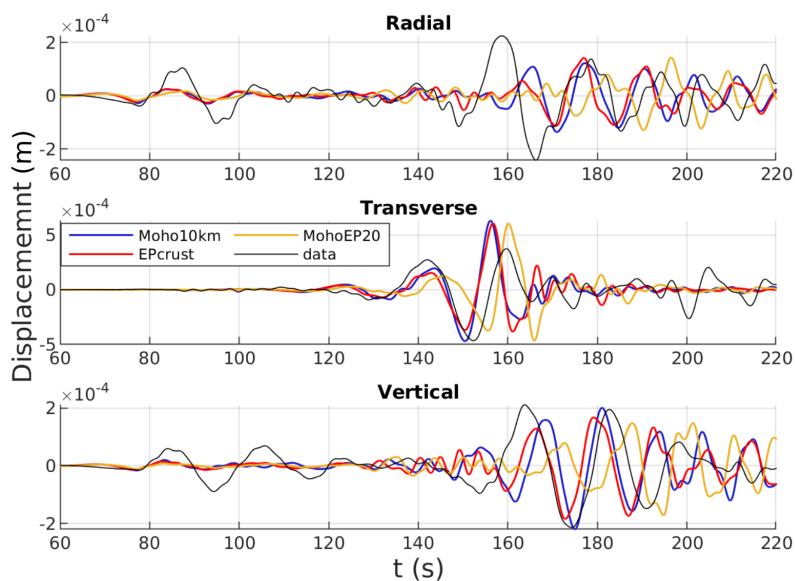


Figure 7.13: Comparison between the different Moho models (Tab. 3) for each seismogram components, recorded at the station in Sicily.

time window of 200 seconds that comprises P-, S-, and early-coda windows. We estimate the correlation coefficient between the synthetic and the recorded waveforms for each of the crustal models available (Fig. 7.14). By regionalizing the correlation coefficients in space, we constrain the validity of the crustal models for the basin. The MohoEP18 model, presenting a crustal pinch, is the one that best explains data when considering all three components in the Issel Bridge, the region between Vavilov and Marsili.

7.4 Discussion

The mixed continental-oceanic crust in basins produces wave reverberations due to sediments, crustal waveguides and topography in the early coda wavefield (Fig. 7.16). Source parameter estimations are thus generally based on near-source data (Tinti et al., 2016) as modelling these phases is challenging. Our study demonstrates that once full-wavefield simulations are available regional-scale recordings can discriminate between different models of source characteristics (Fig. 7.5 and Supplementary) after including crustal velocities and thicknesses derived from previous amplitude-dependent modelling (Nardoni et al., 2021). The full wavefield simulations and use of later coda waves enable

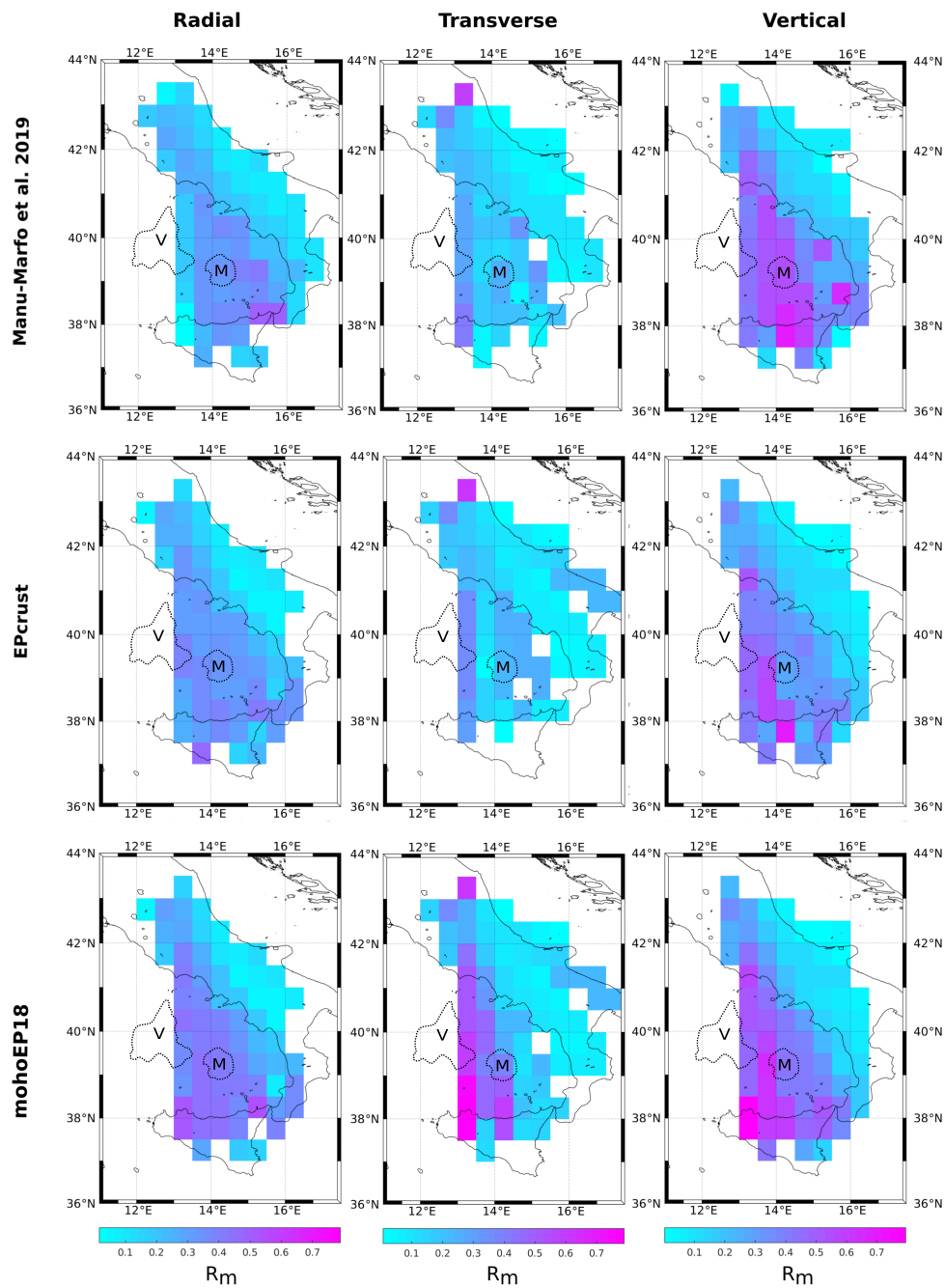


Figure 7.14: Regionalization of the positive correlation coefficients (> 0) between synthetic waveform and recordings at the stations located across Italy (Fig 7.1) in the frequency band 0.05-0.33Hz. The coefficients are evaluated in the time window 0-200s for each component and for three Moho models: from the top to the bottom, Manu-Marfo et al. (2019)(thinner), EPcrust (Molinari and Morelli, 2011), MohoEP18 (see Fig. 7.11). In the figure, the Marsili (M) and Vavilov (V) sub-basins are shown by the dotted lines.

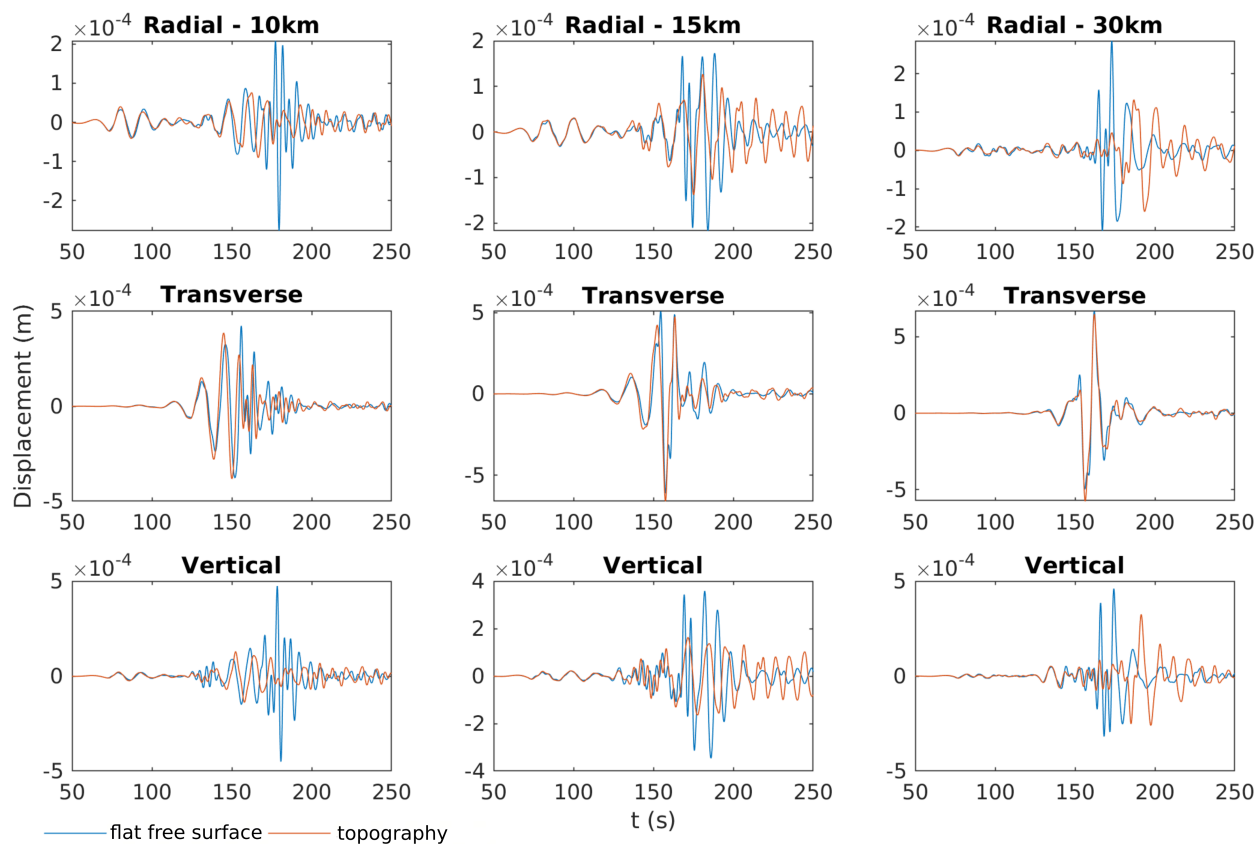


Figure 7.15: Comparison between flat free surface and topography for 3 different layered models by varying the Moho interface depth: 10km (left panels), 15km (center panels), 30km (right panels).

the assessment that the optimal source function for the Accumoli earthquake is a boxcar with a rise time of 6 s, a depth of 7.3 km, and the radiation pattern previously defined by INGV (Tab. 7.2).

All regional seismic phases show high sensitivity to crustal structures Furumura and Kennett (1997). The Moho depth changes the arrivals and amplitudes of complex crustal phases, especially Lg and P/SV conversions and surface waves (Sens-Schönfelder et al., 2009). Figs. 7.12 and 7.13 show data fit across the full seismogram recorded at a single receiver located in Sicily: this source-station path crosses the region characterized by the largest difference between the three available Moho models. The first Moho (Moho10km - Manu-Marfo et al., 2019) is very shallow (approximately 10–12 km thick) below the southern Tyrrhenian basin and offshore the Calabria coast, reflecting the effect of the eastward retreat of the Ionian slab, which resulted in the opening of the Southern Tyrrhenian basin (Malinverno and Ryan, 1986; Faccenna et al., 2001; Doglioni et al.,

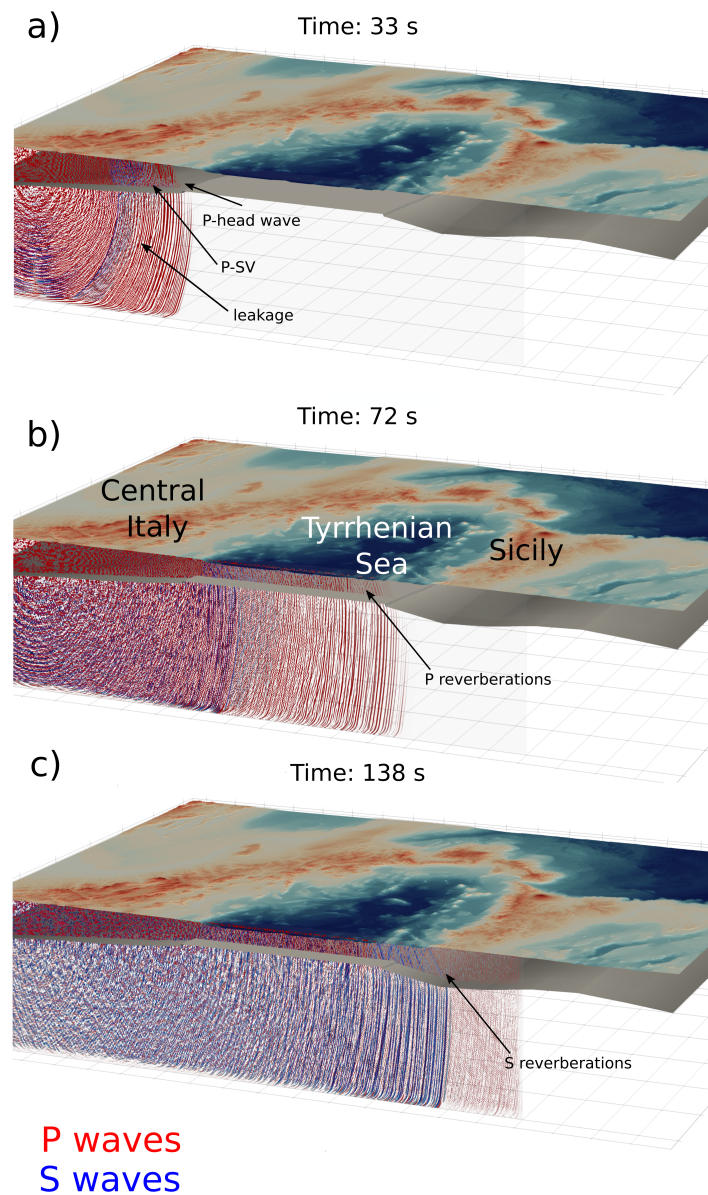


Figure 7.16: P-, S-, and reverberating wavefield modelled across the lithospheric model defined by MohoEP18 (Tab. 7.1). a): P head wave is produced, and the interfaces generate P-SV conversions. b): After 72 s, the P-wavefront travels unperturbed through the flat Moho. Coda waves diffuse under central Italy while reverberating P-waves hinder the detection of S-wave phases on vertical and radial components. c): reverberating P- and S-waves propagate through the flat Moho, while the pinch north of Sicily focuses shear waves in a waveguide. The lack of strong heterogeneity in the mantle produces recognizable P- and S-wave fields and relatively small coda.

1999; Lo Bue et al., 2021). The EPcrust model, similarly to Di Stefano et al. (2011), is characterized by Moho depths varying from an average of 12 km to 20 km in Sicily and the volcanic area of the Eolian Islands. By investigating a single-phase primarily dependent on the vertical component of motion, Moho10 only offers excellent vertical correlation. EPCrust is derived from the integration of larger-scale models (Molinari and Morelli, 2011) and produces average correlations across the entire basin, marginally, better than Moho10 when using the transverse component. Only MohoEP18 (Fig. 7.12) offers satisfactory correlations with data across the three components and especially between Vavilov and Marsili (Fig. 7.12).

MohoEP18 has been established using the full wavefield: its best fit to data is a consequence of considering a wider time window and information discarded by analytical techniques. A thin crustal pinch is necessary to fit data across the Marsili plain. The results imply the need for a deep oceanic Moho across the basin, and specifically between Vavilov and Marsili, to produce the highest, statistically-valuable correlations for radial, transverse, and vertical components. The best fit across the Issel Bridge (Sartori, 2003; Cocchi et al., 2009) is evidence of the need for thinned continental crust between the volcanic centres. Detecting the Bridge confirms that thinned continental crust is still present between the two volcanic centres associated with two different extension episodes: Vavilov, during Tortonian to Pliocene WE migration and Marsilii, formed by Pleistocene NW-SE migration (Sartori, 2003; Cocchi et al., 2009). We are still unable to recover the east structure of the basin satisfactorily due to the more complex continental structures (i.e., faults, thicker sediments - Owens et al. (1984)) that are not implemented in the modelling.

Figure 7.7a shows that reverberations in thicker sediments dominate the transverse component in the early coda time window, producing the primary difference in the very late coda for the vertical and radial components. Transverse components appear most sensitive to the low-velocity sedimentary layers, making them ideal markers of mid-crustal boundaries induced by volcanism across the Aeolian Islands, which is not implemented in the model. Schneider et al. (2013) demonstrate that the transverse component is dominated by dipping structures such as slabs or anisotropy and not by horizontal discontinuities. Instead, horizontal interfaces significantly influence the north-south and vertical plane, i.e., on the P and SV polarizations having a component on the z-direction.

Figure 7.15 demonstrates how relevant topography and bathymetry are for the radial and vertical components. According to the results of Maeda et al. (2011), the compari-

son shown in Fig. S8 suggests that the sea column is the main responsible for the attenuation of these components. Low P-wave velocity in the sea relative to the surrounding bedrock causes wave energy trapped within the basin and decreased amplitude at the receiver. Water acts primarily on the Rayleigh modes (i.e., radial and vertical components Petukhin et al., 2010)), while the effects are weaker for Love waves and due to conversions of Rayleigh into Love waves (e.g. due to transversely inclined shallow interface of oceanic sediments). Instead, the water does not affect the propagation of direct P/S or converted waves. Implementing the topography in the full-waveform modelling is thus a necessary step to obtain feasible models of the Moho discontinuity using full-wavefield information (Takemura et al., 2015).

The results demonstrate that the thinning of the crust and the pinch slope are responsible for reverberations, energy leaked into the mantle and converted waves (Furumura and Kennett, 1997). The evolution of the wavefield in Fig. 7.16 clarifies the strong interaction of P and S waves with the topography and Moho. As shown in Figure 7.16a, the interfaces generate P head waves and P-SV conversion and a loss of energy into the mantle. Once the P waves propagate and reverberate across the crustal waveguide, there are still several conversions between P and S waves due to the topography and presence of a solid-liquid interface (Fig. 7.16b). After 130s (Fig. 7.16c), coherent S waves packet is still propagating under Sicily, while the wavefield has reached diffusion across the continental Moho of Central Italy. Figure 7.16c confirms that the time window 130-200s can be used to estimate the location and shape of the crustal pinch, where shear waves are guided, producing uniquely-recognized waveforms. We can thus best map the Moho depth across mixed continental-oceanic settings from regional observations using two attributes: the first-wave arrival, sensitive to the continental Moho depth (Fig. 7.16a), and the crustal coda waveguide associated with an oceanic Moho (Fig. 7.16b).

7.5 Concluding remarks

We perform low-frequency wave-equation modelling to explore the effects of the 3D structural variations on the propagation of the full wavefield across the Southern Tyrrhenian Sea. The forward modelling shows waveforms affected by topography and sediment and crustal thicknesses, velocities, and velocity fluctuations. We concentrate on phases and amplitudes of P- and S-waves (widely-used parameters for imaging the lithosphere and characterizing earthquake sources) and waves reverberating through

the early S-wave coda, which have shown high sensitivity to Moho depths. Phases and amplitudes modelled for the Accumoli earthquake in Central Italy were compared to those observed at the regional INGV network both qualitatively and quantitatively. The sensitivity of the seismic wavefield to source properties and crustal discontinuities at depth (i.e., crustal and sediment thicknesses and velocities) in the frequency band 0.05 – 0.33Hz provides refined propagation corrections to estimate earthquake source properties. The optimal earthquake source model is a boxcar source time function with a rise time of 6 seconds, depth of 7.3 km, and normal faulting with a strike, dip and rake of 155, 49 and -87 degrees, respectively.

A thin sedimentary layer is necessary to reproduce the data avoiding reverberations from trapped waves. The simulations highlight the existence of crustal waveguides in the early S-coda due to a laterally-varying Moho interface. Its detection trades off with topography, which can disperse and scatter the waves later in the seismogram. The best Moho fit is assessed using correlation analysis with the whole INGV array data. The results confirm the existence of thinned continental crust between the Vavilov and Marsili volcanic centres, the Issel Bridge, a product of the changes in the back-arc extension caused by the Ionian slab. We still cannot recover the full wavefield propagating through the Italian continental crust as we neglect broader structures as extended faults or sediments. However, the simulations also show that the central portion of regional seismograms is sensitive to crustal thinning. This sensitivity proves the need for that crustal pinching between the basin and the Sicilian crust. The modelled regional phases and amplitudes are an ideal forward model for future inversions of Moho depths, especially across mixed continental-oceanic regions, which can be obtained using recordings from a single high-magnitude earthquake with dense arrays. The reconstructed features are essential for assessing past back-arc extension following subduction: similar modelling can be implemented through any interpreted geodynamic model after transformation to seismic velocities, allowing their assessment of present-day data.

Conclusions and outlooks

From local to continental scale, seismic attenuation imaging is one of the most efficient tools to characterize crust heterogeneities. Coda wave attenuation can capture detailed features of highly heterogeneous media, allowing the separation between scattering and absorption contributions. Especially at low frequency (~ 1 Hz) and regional scale, sharp variations in the Earth's structure can bias this separation, in contrast with the hypothesis that coda waves are the results of only scattering and absorption processes. Crustal thinning across a mixed continental-oceanic crust is the primary factor hindering correct imaging of absorption anomalies, primarily due to energy leakage and waves reverberation. Several studies estimated the coda quality factor across continental crust based on the assumption that multiple scattering controls propagation and approaches diffusion at late lapse times (depending on the epicentral distances) frequency (Calvet et al., 2013; Mayor et al., 2016). These studies obtained absorption maps at frequencies of 1.5 Hz. However, they do not tackle oceanic settings.

I have analysed seismic data recorded by the INGV and French networks retrieving coda attenuation values. Then, I have tested coda attenuation imaging based on diffusive kernels in a mixed continental-oceanic setting at 1 Hz across the Italian peninsula and the Tyrrhenian Sea. Relying on the diffusive approximation, a single-layer approximation is assumed without energy loss outside the crust. Where the assumption is invalid, the results show negative Q_c anomalies. These values, especially across the oceanic basin, can thus indicate the breakdown of the diffusive regime due to structural effects (Margerin, 2017). In conclusion, coda attenuation imaging at low frequency (1 Hz) and regional scale is able to detect reverberating waves and energy leakage due to crustal thinning across the oceanic basins. As these effects are related to the Moho variations, the imaging results suggest the possibility of mapping Moho with regional seismicity.

In this framework, forward modelling allows estimating the influence of these effects on waves propagation. By modelling the energy propagation through a combination of ray theory and scattering theory (Sanborn and Cormier, 2018), radiative transfer simu-

lations confirm the sensitivity of regional phases (i.e. Lg, Pg) to Moho depth variations. Crustal reverberations due to crustal waveguides across the basin turn out to control intermediate and late-lapse-time coda-wave energies (> 220 s). Besides, I explored the trade-off between the scale length and the velocity fluctuations parameters finding that the Mie scattering with respect to the high-scattering regime is more appropriate to fit the behaviour of the whole envelope in this setting at 1Hz. Therefore radiative-transfer-based modelling shows the potential to resolve variations of Moho depths and sediments in oceanic settings, regions of crustal reverberations, and volcanism.

Discriminating the stochastic signature and the coherent wave propagation for improving the imaging of oceanic basins is the main focus of the thesis. In these challenging settings and at frequencies where a standard description in terms of single scattering or diffusive processes is infeasible, the tomographic approach can map the effects of large-scale structural variations. The modelling of both the coherent and the stochastic wavefields provides a tool to constrain the heterogeneity spectrum and crustal interface. Full-wavefield modelling allows investigating the effects of the 3D structures on waves propagation and phases arrival and amplitude. I thus have combined the imaging and radiative transfer results with wave equation forward modelling based on the finite difference method across the Southern Tyrrhenian Sea. I have tested the sensitivity of regional seismograms to structure variations of the crust. The results confirm that it is feasible to perform regional full-waveform inversion to map Moho across oceanic basins. By performing synthetic tests in crustal models with and without the crustal pinch, it is possible to constrain the time window and observable (i.e., phase and amplitude), correlate with the data, and define a proper cost function in the inversion process. The final result is a model that provides refined Moho depths, average velocities and their statistical variations using a single regional earthquake.

Combing seismic attenuation tomography with radiative transfer and wave-equation modelling has improved the resolution on the oceanic crust the Tyrrhenian basing, paving the way for characterizing crustal thinning using regional seismograms.

Future projects

Within seismology, full-waveform seismic inversions have revolutionized our ability to image the Earth crust and mantle (Gung and Romanowicz, 2004; French and Romanowicz, 2014; Blom et al., 2020). However, as shown by the sensitivity analysis,

full-waveform inversions are challenging due to the response of seismic wavefields to sharp lateral variations in Earth properties, especially across oceanic basins.

The future perspective of the project is to build a novel full-waveform inversion framework (FIAT - Full-waveform Inversions Across the Tyrrhenian Sea) for mixed continental-oceanic settings, able to image these challenging crustal environments from sparse seismic coverage. The sensitivity tests aim at defining the appropriate misfit function to constrain the Moho depth from the full wavefield. So far, the tests I performed for a single station (Section 7.4) suggest that the correlation coefficient in two different time windows is efficient in discriminating the presence of a pinch. The final result must be a full-waveform inversion scheme especially targeting Moho depths, but also comprising velocity, scattering parameters, and crustal variations, whose forward is based on wave-equation modelling. This implementation and the solution of the wave equation will allow achieving an improved reconstruction of the 3D medium via full-waveform tomography (Chen et al., 2007; Fichtner et al., 2009).

Within **FIAT**: (1) I will define an improved parallelized framework to adapt this forward modelling to the massive datasets necessary for tomography and I will consider effective topography and hypothesized rheology of the target area; (2) I will develop full-waveform inversions of data recovered across the Tyrrhenian basin. These steps require the computation of a consistent amount of synthetic seismograms in a 3D Earth model, and the definition of more advanced inversion schemes. Having more efficient computer resources and memory, I will be able to simulate wavefields at higher frequencies. The full-waveform inversion scheme will employ computational methods that are developed expressively to characterize seismic wave propagation in challenging environments such as the Italian peninsula and the Tyrrhenian sea. This implementation and the solution of the wave-equation will allow achieving an improved reconstruction of the 3D medium via full-waveform tomography (Chen et al., 2007).

Bibliography

- W. G. Akande, L. De Siena, and Q. Gan. Three-dimensional kernel-based coda attenuation imaging of caldera structures controlling the 1982-84 campi flegrei unrest. *Journal of Volcanology and Geothermal Research*, 381:273–283, 2019.
- K. Aki. Analysis of the seismic coda of local earthquakes as scattered waves. *Journal of geophysical research*, 74(2):615–631, 1969.
- K. Aki and B. Chouet. Origin of coda waves: source, attenuation, and scattering effects. *Journal of geophysical research*, 80(23):3322–3342, 1975.
- K. Aki and W. Lee. Determination of three-dimensional velocity anomalies under a seismic array using first P arrival times from local earthquakes: 1. A homogeneous initial model. *Journal of Geophysical research*, 81(23):4381–4399, 1976.
- K. Aki and P. G. Richards. *Quantitative seismology*. University Science Books, 2002.
- K. Aki, A. Christoffersson, and E. S. Husebye. Determination of the three-dimensional seismic structure of the lithosphere. *Journal of Geophysical Research*, 82(2):277–296, 1977.
- P. Alvarado, S. Beck, and G. Zandt. Crustal structure of the south-central Andes Cordillera and backarc region from regional waveform modelling. *Geophysical Journal International*, 170(2):858–875, 2007.
- C. Amante and B. Eakins. ETOPO1 1 Arc-minute Global Relief Model: procedures, data sources and analysis. NOAA Technical Memorandum NESDIS NGDC-24. *National Geophysical Data Center, NOAA*, 2009. doi: 10.7289/V5C8276M.
- R. C. Aster, B. Borchers, and C. H. Thurber. *Parameter estimation and inverse problems*, volume 90. Academic Press, 2011.

- D. R. Baumgardt. Sedimentary basins and the blockage of Lg wave propagation in the continents. *Pure and Applied Geophysics*, 158(7):1207–1250, 2001.
- F. Bianco, E. Del Pezzo, M. Castellano, J. Ibanez, and F. Di Luccio. Separation of intrinsic and scattering seismic attenuation in the Southern Apennine zone, Italy. *Geophysical Journal International*, 150(1):10–22, 2002.
- J. Blanch, J. Robertsson, and W. Symes. Modeling of a constant. *Q*, 60(1):176–184, 1995.
- N. Blom, A. Gokhberg, and A. Fichtner. Seismic waveform tomography of the central and eastern Mediterranean upper mantle. *Solid Earth*, 11(2):669–690, 2020.
- F. Borleanu, L. De Siena, C. Thomas, M. Popa, and M. Radulian. Seismic scattering and absorption mapping from intermediate-depth earthquakes reveals complex tectonic interactions acting in the Vrancea region and surroundings (Romania). *Tectonophysics*, 706:129–142, 2017.
- M. Bostock and B. Kennett. The effect of 3-D structure on Lg propagation patterns. *Geophysical Journal International*, 101(2):355–365, 1990.
- E. Bozdağ, J. Trampert, and J. Tromp. Misfit functions for full waveform inversion based on instantaneous phase and envelope measurements. *Geophysical Journal International*, 185(2):845–870, 2011.
- E. Bozdağ, D. Peter, M. Lefebvre, D. Komatitsch, J. Tromp, J. Hill, N. Podhorszki, and D. Pugmire. Global adjoint tomography: first-generation model. *Geophysical Journal International*, 207(3):1739–1766, 2016.
- F. Brich. The velocity of compressional waves in rocks to 10 kbars: part 1. *Journal of Geophysical Research*, 65:1083–1102, 1960.
- M. Calvet and L. Margerin. Lapse-time dependence of coda Q: Anisotropic multiple-scattering models and application to the Pyrenees. *Bulletin of the Seismological Society of America*, 103(3):1993–2010, 2013.
- M. Calvet, M. Sylvander, L. Margerin, and A. Villaseñor. Spatial variations of seismic attenuation and heterogeneity in the Pyrenees: Coda Q and peak delay time analysis. *Tectonophysics*, 608:428–439, 2013.

- M. Campillo, J.-L. Plantet, and M. Bouchon. Frequency-dependent attenuation in the crust beneath central France from Lg waves: data analysis and numerical modeling. *Bulletin of the Seismological Society of America*, 75(5):1395–1411, 1985.
- J. M. Carcione. *Wave fields in real media: Wave propagation in anisotropic, anelastic, porous and electromagnetic media*. Elsevier, 2007.
- C. Cerjan, D. Kosloff, R. Kosloff, and M. Reshef. A nonreflecting boundary condition for discrete acoustic and elastic wave equations. *Geophysics*, 50(4):705–708, 1985.
- V. Červený. *Seismic ray theory*, volume 110. Cambridge university press Cambridge, 2001.
- S. Chandrasekhar. *Radiative transfer*. Courier Corporation, 2013.
- P. Chen, L. Zhao, and T. H. Jordan. Full 3D tomography for the crustal structure of the Los Angeles region. *Bulletin of the Seismological Society of America*, 97(4):1094–1120, 2007.
- A. Cirella, G. Pezzo, and A. Piatanesi. Rupture kinematics and structural-rheological control of the 2016 Mw 6. 1 Amatrice (Central Italy) earthquake from joint inversion of seismic and geodetic data. *Geophysical Research Letters*, 45(22):12–302, 2018.
- L. Cocchi, F. Caratori Tontini, F. Muccini, M. Marani, G. Bortoluzzi, and C. Carmisciano. Chronology of the transition from a spreading ridge to an accretional seamount in the marsili backarc basin (tyrrhenian sea). *Terra Nova*, 21(5):369–374, 2009.
- V. F. Cormier and C. J. Sanborn. Trade-Offs in Parameters Describing Crustal Heterogeneity and Intrinsic Attenuation from Radiative Transport Modeling of High-Frequency Regional Seismograms Trade-Offs in Parameters Describing Crustal Heterogeneity and Intrinsic Attenuation. *Bulletin of the Seismological Society of America*, 109(1):312–321, 2019.
- O. Coutant, J. Virieux, and A. Zollo. Numerical source implementation in a 2D finite difference scheme for wave propagation. *Bulletin of the Seismological Society of America*, 85(5):1507–1512, 1995.
- F. Dahlen and A. M. Baig. Fréchet kernels for body-wave amplitudes. *Geophysical Journal International*, 150(2):440–466, 2002.

- L. De Siena, M. Calvet, K. J. Watson, A. Jonkers, and C. Thomas. Seismic scattering and absorption mapping of debris flows, feeding paths, and tectonic units at Mount St. Helens volcano. *Earth and Planetary Science Letters*, 442:21–31, 2016.
- L. De Siena, A. Amoruso, E. D. Pezzo, Z. Wakeford, M. Castellano, and L. Crescentini. Space-weighted seismic attenuation mapping of the aseismic source of Campi Flegrei 1983–1984 unrest. *Geophysical Research Letters*, 44(4):1740–1748, 2017.
- J. De Souza and B. Mitchell. Lg coda Q variations across South America and their relation to crustal evolution. *Pure and Applied Geophysics*, 153(2-4):587–612, 1998.
- E. Del Pezzo, F. Bianco, S. Marzorati, P. Augliera, E. D’Alema, and M. Massa. Depth-dependent intrinsic and scattering seismic attenuation in north central Italy. *Geophysical Journal International*, 186(1):373–381, 2011.
- E. Del Pezzo, J. Ibanez, J. Prudencio, F. Bianco, and L. De Siena. Absorption and scattering 2-D volcano images from numerically calculated space-weighting functions. *Geophysical Journal International*, 206(2):742–756, 2016.
- E. Del Pezzo, A. De La Torre, F. Bianco, J. Ibanez, S. Gabrielli, and L. De Siena. Numerically calculated 3D space-weighting functions to image crustal volcanic structures using diffuse coda waves. *Geosciences*, 8(5):175, 2018.
- M. D. P. Di Martino, L. De Siena, D. Healy, and S. Vialle. Petro-mineralogical controls on coda attenuation in volcanic rock samples. *Geophysical Journal International*, 226(3):1858–1872, 2021.
- R. Di Stefano, C. Chiarabba, F. Lucente, and A. Amato. Crustal and uppermost mantle structure in Italy from the inversion of P-wave arrival times: geodynamic implications. *Geophysical Journal International*, 139(2):483–498, 1999.
- R. Di Stefano, E. Kissling, C. Chiarabba, A. Amato, and D. Giardini. Shallow subduction beneath Italy: Three-dimensional images of the Adriatic-European-Tyrrhenian lithosphere system based on high-quality P wave arrival times. *Journal of Geophysical Research: Solid Earth*, 114(B5), 2009.
- R. Di Stefano, I. Bianchi, M. G. Ciaccio, G. Carrara, and E. Kissling. Three-dimensional Moho topography in Italy: New constraints from receiver functions and controlled source seismology. *Geochemistry, Geophysics, Geosystems*, 12(9), 2011.

- C. Doglioni, M. Fernandez, E. Gueguen, and F. Sabat. On the interference between the early Apennines-Maghrebides backarc extension and the Alps-Betics orogen in the Neogene Geodynamics of the Western Mediterranean. *BOLLETTINO-SOCIETA GEOLOGICA ITALIANA*, 118:75–90, 1999.
- J. Duschenes, M. Sinha, and K. Louden. A seismic refraction experiment in the Tyrrhenian Sea. *Geophysical Journal International*, 85(1):139–160, 1986.
- C. Faccenna, T. W. Becker, F. P. Lucente, L. Jolivet, and F. Rossetti. History of subduction and back arc extension in the Central Mediterranean. *Geophysical Journal International*, 145(3):809–820, 2001.
- M. Fehler, M. Hoshiya, H. Sato, and K. Obara. Separation of scattering and intrinsic attenuation for the Kanto-Tokai region, Japan, using measurements of S-wave energy versus hypocentral distance. *Geophysical Journal International*, 108(3):787–800, 1992.
- A. Fichtner, B. L. Kennett, H. Igel, and H.-P. Bunge. Theoretical background for continental-and global-scale full-waveform inversion in the time–frequency domain. *Geophysical Journal International*, 175(2):665–685, 2008.
- A. Fichtner, B. L. Kennett, H. Igel, and H.-P. Bunge. Full seismic waveform tomography for upper-mantle structure in the Australasian region using adjoint methods. *Geophysical Journal International*, 179(3):1703–1725, 2009.
- I. Finetti. The CROP profiles across the Mediterranean Sea (CROP MARE I and II). *Memorie descrittive della Carta Geologica d’Italia*, 62:171–184, 2003.
- S. French and B. Romanowicz. Whole-mantle radially anisotropic shear velocity structure from spectral-element waveform tomography. *Geophysical Journal International*, 199(3):1303–1327, 2014.
- L.-Y. Fu, R.-S. Wu, and M. Campillo. Energy partition and attenuation of regional phases by random free surface. *Bulletin of the Seismological Society of America*, 92(5):1992–2007, 2002.
- T. Furumura and B. Kennett. On the nature of regional seismic phases—II. On the influence of structural barriers. *Geophysical Journal International*, 129(2):221–234, 1997.

- T. Furumura and B. Kennett. The Significance of Long-Period Ground Motion at Regional to Teleseismic Distances From the 610-km Deep Mw 8.3 Sea of Okhotsk Earthquake of 24 May 2013. *Journal of Geophysical Research: Solid Earth*, 124(8):9075–9094, 2019.
- S. Gabrielli, L. De Siena, F. Napolitano, and E. Del Pezzo. Understanding seismic path biases and magmatic activity at Mount St Helens volcano before its 2004 eruption. *Geophysical Journal International*, 222(1):169–188, 2020.
- S. Gabrielli, A. Akinci, G. Ventura, F. Napolitano, E. Del Pezzo, and L. De Siena. Changes in seismic attenuation due to fracturing and fluid migration during the 2016–2017 Central Italy seismic sequence. *Earth and Space Science Open Archive ESSOAr*, 2021.
- R. W. Graves and D. J. Wald. Resolution analysis of finite fault source inversion using one- and three-dimensional Green’s functions: 1. Strong motions. *Journal of Geophysical Research: Solid Earth*, 106(B5):8745–8766, 2001.
- Y. Gung and B. Romanowicz. Q tomography of the upper mantle using three-component long-period waveforms. *Geophysical Journal International*, 157(2):813–830, 2004.
- P. Guo, S. C. Singh, V. A. Vaddineni, G. Visser, I. Grevemeyer, and E. Saygin. Non-linear full waveform inversion of wide-aperture OBS data for Moho structure using a trans-dimensional Bayesian method. *Geophysical Journal International*, 224(2):1056–1078, 2021.
- R. B. Herrmann. SH-wave generation by dislocation sources—a numerical study. *Bulletin of the Seismological Society of America*, 69(1):1–15, 1979.
- M. Hoshiwa. Simulation of multiple-scattered coda wave excitation based on the energy conservation law. *Physics of the Earth and Planetary Interiors*, 67(1-2):123–136, 1991.
- M. Hoshiwa. Simulation of coda wave envelope in depth dependent scattering and absorption structure. *Geophysical research letters*, 21(25):2853–2856, 1994.
- H. Igel. *Computational seismology: a practical introduction*. Oxford University Press, 2017.

- L. Improta, G. Iannaccone, P. Capuano, A. Zollo, and P. Scandone. Inferences on the upper crustal structure of Southern Apennines (Italy) from seismic refraction investigations and subsurface data. *Tectonophysics*, 317(3-4):273–298, 2000.
- H. Karaoğlu and B. Romanowicz. Global seismic attenuation imaging using full-waveform inversion: a comparative assessment of different choices of misfit functionals. *Geophysical Journal International*, 212(2):807–826, 2018.
- S. L. Klemperer, T. Hauge, E. Hauser, J. Oliver, and C. Potter. The Moho in the northern Basin and Range province, Nevada, along the COCORP 40 N seismic-reflection transect. *Geological Society of America Bulletin*, 97(5):603–618, 1986.
- D. Komatitsch, G. Erlebacher, D. Göldeke, and D. Michéa. High-order finite-element seismic wave propagation modeling with MPI on a large GPU cluster. *Journal of Computational Physics*, 229(20):7692–7714, 2010.
- M. Korn. Determination of site-dependent scattering Q from P-wave coda analysis with an energy-flux model. *Geophysical Journal International*, 113(1):54–72, 1993.
- L. Krischer, A. R. Hutko, M. van Driel, S. Stähler, M. Bahavar, C. Trabant, and T. Nissen-Meyer. On-demand custom broadband synthetic seismograms. *Seismological Research Letters*, 88(4):1127–1140, 2017.
- C. A. Langston. Structure under Mount Rainier, Washington, inferred from teleseismic body waves. *Journal of Geophysical Research: Solid Earth*, 84(B9):4749–4762, 1979.
- T. Lay and T. C. Wallace. *Modern Global Seismology, Volume 58 (International Geophysics)*, 1995.
- E.-J. Lee, P. Chen, T. H. Jordan, P. B. Maechling, M. A. Denolle, and G. C. Beroza. Full-3-D tomography for crustal structure in southern California based on the scattering-integral and the adjoint-wavefield methods. *Journal of Geophysical Research: Solid Earth*, 119(8):6421–6451, 2014.
- W. S. Lee, S. Yun, and J.-Y. Do. Scattering and intrinsic attenuation of short-period S waves in the Gyeongsang Basin, South Korea, revealed from S-wave seismogram envelopes based on the radiative transfer theory. *Bulletin of the Seismological Society of America*, 100(2):833–840, 2010.

- J. M. Lees. Seismic tomography of magmatic systems. *Journal of Volcanology and Geothermal Research*, 167(1-4):37–56, 2007.
- A. Levander, R. England, S. Smith, R. Hobbs, J. Goff, and K. Holliger. Stochastic characterization and seismic response of upper and middle crustal rocks based on the Lewisian gneiss complex, Scotland. *Geophysical Journal International*, 119(1): 243–259, 1994.
- R. Lo Bue, M. Faccenda, and J. Yang. The role of adria plate lithospheric structures on the recent dynamics of the central mediterranean region. *Journal of Geophysical Research: Solid Earth*, 126(10):e2021JB022377, 2021.
- T. Maeda and T. Furumura. FDM simulation of seismic waves, ocean acoustic waves, and tsunamis based on tsunami-coupled equations of motion. *Pure and Applied Geophysics*, 170(1):109–127, 2013.
- T. Maeda, H. Sato, and M. Ohtake. Synthesis of Rayleigh-wave envelope on the spherical Earth: Analytic solution of the single isotropic-scattering model for a circular source radiation. *Geophysical research letters*, 30(6), 2003.
- T. Maeda, T. Furumura, S. Sakai, and M. Shinohara. Significant tsunami observed at ocean-bottom pressure gauges during the 2011 off the Pacific coast of Tohoku Earthquake. *Earth, Planets and Space*, 63(7):803–808, 2011.
- T. Maeda, T. Furumura, S. Noguchi, S. Takemura, S. Sakai, M. Shinohara, K. Iwai, and S.-J. Lee. Seismic-and tsunami-wave propagation of the 2011 Off the Pacific Coast of Tohoku Earthquake as inferred from the tsunami-coupled finite-difference simulation. *Bulletin of the Seismological Society of America*, 103(2B):1456–1472, 2013.
- T. Maeda, S. Takemura, and T. Furumura. OpenSWPC: an open-source integrated parallel simulation code for modeling seismic wave propagation in 3D heterogeneous viscoelastic media. *Earth, Planets and Space*, 69(1):102, 2017.
- F. Magnoni, E. Casarotti, D. Komatitsch, R. Di Stefano, M. G. Ciaccio, C. Tape, D. Melini, A. Michelini, A. Piersanti, and J. Tromp. Adjoint tomography of the italian lithosphere. *Communications Earth & Environment*, page 69, 2022.

- F. Magrini, G. Diaferia, A. El-Sharkawy, F. Cammarano, M. van der Meijde, T. Meier, and L. Boschi. Surface-wave tomography of the central-western mediterranean: new insights into the liguro-provençal and tyrrhenian basins. *Journal of Geophysical Research: Solid Earth*, page e2021JB023267, 2022.
- A. Malinverno and W. B. Ryan. Extension in the Tyrrhenian Sea and shortening in the Apennines as result of arc migration driven by sinking of the lithosphere. *Tectonics*, 5(2):227–245, 1986.
- D. Manu-Marfo, A. Aoudia, S. Pachhai, and R. Kherchouche. 3D shear wave velocity model of the crust and uppermost mantle beneath the Tyrrhenian basin and margins. *Scientific reports*, 9(1):3609, 2019.
- L. Margerin. Breakdown of equipartition in diffuse fields caused by energy leakage. *The European Physical Journal Special Topics*, 226(7):1353–1370, 2017.
- L. Margerin, M. Campillo, N. Shapiro, and B. van Tiggelen. Residence time of diffuse waves in the crust as a physical interpretation of coda Q: application to seismograms recorded in Mexico. *Geophysical Journal International*, 138(2):343–352, 1999.
- L. Margerin, T. Planès, J. Mayor, and M. Calvet. Sensitivity kernels for coda-wave interferometry and scattering tomography: theory and numerical evaluation in two-dimensional anisotropically scattering media. *Geophysical Journal International*, 204(1):650–666, 2016.
- J. Mascle and J.-P. Rehault. A revised seismic stratigraphy of the Tyrrhenian Sea: Implications for the basin evolution. *Proc. Ocean Drill. Program Sci.Results*, 107, page 617–636, 1990.
- T. Matsuzawa, K. Obara, and T. Maeda. Source duration of deep very low frequency earthquakes in western Shikoku, Japan. *Journal of Geophysical Research: Solid Earth*, 114(B11), 2009.
- G. P. Mavroeidis and A. S. Papageorgiou. A mathematical representation of near-fault ground motions. *Bulletin of the seismological society of America*, 93(3):1099–1131, 2003.

- J. Mayor, L. Margerin, and M. Calvet. Sensitivity of coda waves to spatial variations of absorption and scattering: radiative transfer theory and 2-D examples. *Geophysical Journal International*, 197(2):1117–1137, 2014.
- J. Mayor, M. Calvet, L. Margerin, O. Vanderhaeghe, and P. Traversa. Crustal structure of the Alps as seen by attenuation tomography. *Earth and Planetary Science Letters*, 439:71–80, 2016.
- G. Mele, A. Rovelli, D. Seber, and M. Barazangi. Shear wave attenuation in the lithosphere beneath Italy and surrounding regions: tectonic implications. *Journal of Geophysical Research: Solid Earth*, 102(B6):11863–11875, 1997.
- W. Menke. Case studies of seismic tomography and earthquake location in a regional context. *GEOPHYSICAL MONOGRAPH-AMERICAN GEOPHYSICAL UNION*, 157:7, 2005.
- M. I. Mishchenko, L. D. Travis, and A. A. Lacis. *Multiple scattering of light by particles: radiative transfer and coherent backscattering*. Cambridge University Press, 2006.
- B. Mitchel, S. Baqer, A. Akinci, and L. Cong. Lg coda Q in Australia and its relation to crustal structure and evolution. In *Q of the Earth: Global, Regional, and Laboratory Studies*, pages 639–653. Springer, 1998.
- B. Mitchell, L. Cong, and G. Ekström. A continent-wide map of 1-Hz Lg coda Q variation across Eurasia and its relation to lithospheric evolution. *Journal of Geophysical Research: Solid Earth*, 113(B4), 2008.
- B. Mitchell, L. Cong, and A. L. Jemberie. Continent-wide maps of Lg coda Q for North America and their relationship to crustal structure and evolution. *Bulletin of the Seismological Society of America*, 105(1):409–419, 2015.
- P. Moczo, J. Kristek, and M. Gális. *The finite-difference modelling of earthquake motions: Waves and ruptures*. Cambridge University Press, 2014.
- S. Moeller, I. Grevemeyer, C. R. Ranero, C. Berndt, D. Klaeschen, V. Sallarès, N. Zitellini, and R. de Franco. Early-stage rifting of the northern Tyrrhenian Sea Basin: Results from a combined wide-angle and multichannel seismic study. *Geochemistry, Geophysics, Geosystems*, 14(8):3032–3052, 2013.

- I. Molinari and A. Morelli. EPcrust: A reference crustal model for the European plate. *Geophys. J. Int.*, 185(1):352–364, 2011. doi: 10.1111/j.1365-246X.2011.04940.x.
- I. Molinari, A. Argnani, A. Morelli, and P. Basini. Development and testing of a 3D seismic velocity model of the Po Plain sedimentary basin, Italy. *Bulletin of the Seismological Society of America*, 105(2A):753–764, 2015a.
- I. Molinari, J. Verbeke, L. Boschi, E. Kissling, and A. Morelli. Italian and Alpine three-dimensional crustal structure imaged by ambient-noise surface-wave dispersion. *Geochemistry, Geophysics, Geosystems*, 16(12):4405–4421, 2015b.
- I. B. Morozov and M. Safarshahi. Elastic Character of Seismic Coda Envelopes Within East Indian Shield. *Pure and Applied Geophysics*, 177(12):5799–5818, 2020.
- V. Moskalenko. Volcanic-Sedimentary Deposits in the Tyrrhenian Abyssal Basin. *International Geology Review*, 34(2):178–186, 1992.
- T. Nakamura, H. Takenaka, T. Okamoto, and Y. Kaneda. FDM simulation of seismic-wave propagation for an aftershock of the 2009 Suruga Bay earthquake: effects of ocean-bottom topography and seawater layer. *Bulletin of the Seismological Society of America*, 102(6):2420–2435, 2012.
- F. Napolitano, L. De Siena, A. Gervasi, I. Guerra, R. Scarpa, and M. La Rocca. Scattering and absorption imaging of a highly fractured fluid-filled seismogenetic volume in a region of slow deformation. *Geoscience Frontiers*, 2019.
- F. Napolitano, L. De Siena, A. Gervasi, I. Guerra, R. Scarpa, and M. La Rocca. Scattering and absorption imaging of a highly fractured fluid-filled seismogenetic volume in a region of slow deformation. *Geoscience Frontiers*, 11(3):989–998, 2020.
- C. Nardoni, L. De Siena, F. Cammarano, F. Magrini, and E. Mattei. Modelling regional-scale attenuation across Italy and the Tyrrhenian Sea. *Physics of the Earth and Planetary Interiors*, 318:106764, 2021.
- A. Obermann, T. Planès, E. Larose, C. Sens-Schönfelder, and M. Campillo. Depth sensitivity of seismic coda waves to velocity perturbations in an elastic heterogeneous medium. *Geophysical Journal International*, 194(1):372–382, 2013.

- M. Ogiso. A method for mapping intrinsic attenuation factors and scattering coefficients of S waves in 3-D space and its application in southwestern Japan. *Geophysical Journal International*, 216(2):948–957, 2019.
- T. J. Owens, G. Zandt, and S. R. Taylor. Seismic evidence for an ancient rift beneath the Cumberland Plateau, Tennessee: A detailed analysis of broadband teleseismic P waveforms. *Journal of Geophysical Research: Solid Earth*, 89(B9):7783–7795, 1984.
- J. Paasschens. Solution of the time-dependent Boltzmann equation. *Physical Review E*, 56(1):1135, 1997.
- C. Pacheco and R. Snieder. Time-lapse travel time change of multiply scattered acoustic waves. *The Journal of the Acoustical Society of America*, 118(3):1300–1310, 2005.
- C. Pauselli, M. R. Barchi, C. Federico, M. B. Magnani, and G. Minelli. The crustal structure of the northern Apennines (central Italy): An insight by the CROP03 seismic line. *American Journal of Science*, 306(6):428–450, 2006.
- F. Pepe, A. Sulli, G. Bertotti, and R. Catalano. Structural highs formation and their relationship to sedimentary basins in the north Sicily continental margin (southern Tyrrhenian Sea): Implication for the Drepano Thrust Front. *Tectonophysics*, 409(1-4):1–18, 2005.
- A. Petukhin, T. Iwata, and T. Kagawa. Study on the effect of the oceanic water layer on strong ground motion simulations. *Earth, planets and space*, 62(8):621–630, 2010.
- N. Piana Agostinetti and A. Amato. Moho depth and Vp/Vs ratio in peninsular Italy from teleseismic receiver functions. *Journal of Geophysical Research: Solid Earth*, 114(B6), 2009.
- N. Piana Agostinetti, M. S. Steckler, and F. P. Lucente. Imaging the subducted slab under the Calabrian Arc, Italy, from receiver function analysis. *Lithosphere*, 1(3): 131–138, 2009.
- C. Piromallo and A. Morelli. P wave tomography of the mantle under the Alpine-Mediterranean area. *Journal of Geophysical Research: Solid Earth*, 108(B2), 2003.

- A. Pontevivo and G. F. Panza. The lithosphere-asthenosphere system in the Calabrian Arc and surrounding seas–Southern Italy. *Pure and Applied Geophysics*, 163(8): 1617–1659, 2006.
- J. Prudencio, E. Del Pezzo, A. García-Yeguas, and J. M. Ibáñez. Spatial distribution of intrinsic and scattering seismic attenuation in active volcanic islands–I: model and the case of Tenerife Island. *Geophysical Journal International*, 195(3):1942–1956, 2013a.
- J. Prudencio, J. M. Ibáñez, A. García-Yeguas, E. Del Pezzo, and A. M. Posadas. Spatial distribution of intrinsic and scattering seismic attenuation in active volcanic islands–II: Deception Island images. *Geophysical Journal International*, 195(3):1957–1969, 2013b.
- J. Prudencio, M. Manga, and T. Taira. Subsurface structure of Long Valley Caldera imaged with seismic scattering and intrinsic attenuation. *Journal of Geophysical Research: Solid Earth*, 123(7):5987–5999, 2018.
- J. Przybilla, M. Korn, and U. Wegler. Radiative transfer of elastic waves versus finite difference simulations in two-dimensional random media. *Journal of Geophysical Research: Solid Earth*, 111(B4), 2006.
- S. Pullammanappallil, A. Levander, and S. P. Larkin. Estimation of crustal stochastic parameters from seismic exploration data. *Journal of Geophysical Research: Solid Earth*, 102(B7):15269–15286, 1997.
- T. Rautian and V. Khalturin. The use of the coda for determination of the earthquake source spectrum. *Bulletin of the Seismological Society of America*, 68(4):923–948, 1978.
- N. Rawlinson and W. Spakman. On the use of sensitivity tests in seismic tomography. *Geophysical Journal International*, 205(2):1221–1243, 2016.
- N. Rawlinson, S. Pozgay, and S. Fishwick. Seismic tomography: a window into deep Earth. *Physics of the Earth and Planetary Interiors*, 178(3-4):101–135, 2010.
- N. Rawlinson, A. Fichtner, M. Sambridge, and M. K. Young. Seismic tomography and the assessment of uncertainty. *Advances in geophysics*, 55:1–76, 2014.

- J. O. Robertsson, J. O. Blanch, and W. W. Symes. Viscoelastic finite-difference modeling. *Geophysics*, 59(9):1444–1456, 1994.
- A. J. Rodgers, J. F. Ni, and T. M. Hearn. Propagation characteristics of short-period Sn and Lg in the Middle East. *Bulletin of the Seismological Society of America*, 87(2): 396–413, 1997.
- B. Romanowicz and B. Mitchell. Deep Earth structure Q of the Earth from crust to core. *Treatise on geophysics*, pages 731–774, 2007.
- B. Romanowicz, L.-W. Chen, and S. W. French. Accelerating full waveform inversion via source stacking and cross-correlations. *Geophysical Journal International*, 220(1):308–322, 2020.
- G. Rosenbaum, M. Gasparon, F. P. Lucente, A. Peccerillo, and M. S. Miller. Kinematics of slab tear faults during subduction segmentation and implications for Italian magmatism. *Tectonics*, 27(2), 2008.
- A. Ross, H. Thybo, and L. Solidilov. Reflection seismic profiles of the core-mantle boundary. *Journal of Geophysical Research: Solid Earth*, 109(B8), 2004.
- C. J. Sanborn. Simulations with Radiative3D: A software tool for radiative transport in 3-D Earth models. 2017.
- C. J. Sanborn and V. F. Cormier. Modelling the blockage of Lg waves from three-dimensional variations in crustal structure. *Geophysical Journal International*, 214(2):1426–1440, 2018.
- C. J. Sanborn, V. F. Cormier, and M. Fitzpatrick. Combined effects of deterministic and statistical structure on high-frequency regional seismograms. *Geophysical Journal International*, 210(2):1143–1159, 2017.
- R. Sartori. The Tyrrhenian back-arc basin and subduction of the Ionian lithosphere. *Episodes*, 26(3):217–221, 2003.
- H. Sato. Formulation of the multiple non-isotropic scattering process in 2-D space on the basis of energy-transport theory. *Geophysical Journal International*, 117(3):727–732, 1994.

- H. Sato, H. Nakahara, and M. Ohtake. Synthesis of scattered energy density for non-spherical radiation from a point shear-dislocation source based on the radiative transfer theory. *Physics of the earth and planetary interiors*, 104(1-3):1–13, 1997.
- H. Sato, M. Fehler, and T. Maeda. *Seismic wave propagation and scattering in the heterogeneous earth*, volume 496. Springer, 2012.
- F. Schneider, X. Yuan, B. Schurr, J. Mechie, C. Sippl, C. Haberland, V. Minaev, I. Oimahmadov, M. Gadoev, N. Radjabov, et al. Seismic imaging of subducting continental lower crust beneath the Pamir. *Earth and Planetary Science Letters*, 375: 101–112, 2013.
- M. Schwardt, D. Köhn, T. Wunderlich, D. Wilken, M. Seeliger, T. Schmidts, H. Brückner, S. Başaran, and W. Rabbel. Characterization of silty to fine-sandy sediments with SH waves: Full waveform inversion in comparison with other geophysical methods. *Near Surface Geophysics*, 18(3):217–248, 2020.
- D. Scrocca, C. Doglioni, and F. Innocenti. Constraints for an interpretation of the Italian geodynamics: a review. *Memorie Descrittive della Carta Geologica d’Italia*, 62:15–46, 2003.
- C. Sens-Schönfelder, L. Margerin, and M. Campillo. Laterally heterogeneous scattering explains Lg blockage in the Pyrenees. *Journal of Geophysical Research: Solid Earth*, 114(B7), 2009.
- N. Shapiro, N. Béthoux, M. Campillo, and A. Paul. Regional seismic phases across the Ligurian Sea: Lg blockage and oceanic propagation. *Physics of the earth and planetary interiors*, 93(3-4):257–268, 1996.
- P. M. Shearer and P. S. Earle. The global short-period wavefield modelled with a Monte Carlo seismic phonon method. *Geophysical Journal International*, 158(3): 1103–1117, 2004.
- A. Shito, S. Matsumoto, T. Ohkura, H. Shimizu, S. Sakai, Y. Iio, H. Takahashi, H. Yakiwara, T. Watanabe, M. Kosuga, et al. 3-D intrinsic and scattering seismic attenuation structures beneath Kyushu, Japan. *Journal of Geophysical Research: Solid Earth*, 2020.

- P. Sketsiou, F. Napolitano, A. Zenonos, and L. De Siena. New insights into seismic absorption imaging. *Physics of the Earth and Planetary Interiors*, 298:106337, 2020.
- D. Soergel, H. Pedersen, L. Stehly, L. Margerin, A. Paul, and A. W. Group. Coda-Q in the 2.5–20 s period band from seismic noise: application to the greater Alpine area. *Geophysical Journal International*, 220(1):202–217, 2020.
- W. Spakman and R. Wortel. A tomographic view on western mediterranean geodynamics. In *The TRANSMED atlas. The Mediterranean region from crust to mantle*, pages 31–52. Springer, 2004.
- S. Stein and M. Wysession. *An introduction to seismology, earthquakes, and earth structure*. John Wiley & Sons, 2009.
- M. Supino, G. Festa, and A. Zollo. A probabilistic method for the estimation of earthquake source parameters from spectral inversion: application to the 2016–2017 Central Italy seismic sequence. *Geophysical Journal International*, 218(2):988–1007, 2019.
- T. Takahashi, H. Sato, T. Nishimura, and K. Obara. Strong inhomogeneity beneath Quaternary volcanoes revealed from the peak delay analysis of S-wave seismograms of microearthquakes in northeastern Japan. *Geophysical Journal International*, 168(1):90–99, 2007.
- T. Takahashi, H. Sato, T. Nishimura, and K. Obara. Tomographic inversion of the peak delay times to reveal random velocity fluctuations in the lithosphere: method and application to northeastern Japan. *Geophysical Journal International*, 178(3):1437–1455, 2009.
- S. Takemura, T. Furumura, and T. Maeda. Scattering of high-frequency seismic waves caused by irregular surface topography and small-scale velocity inhomogeneity. *Geophysical Journal International*, 201(1):459–474, 2015.
- S. Takemura, S. Yabe, and K. Emoto. Modelling high-frequency seismograms at ocean bottom seismometers: effects of heterogeneous structures on source parameter estimation for small offshore earthquakes and shallow low-frequency tremors. *Geophysical Journal International*, 223(3):1708–1723, 2020.

- H. Takenaka and Y. Fujii. A compact representation of spatio-temporal slip distribution on a rupturing fault. *Journal of seismology*, 12(2):281–293, 2008.
- L. Thomsen. Reflection seismology over azimuthally anisotropic media. *Geophysics*, 53(3):304–313, 1988.
- C. Thurber, H. Zhang, T. Brocher, and V. Langenheim. Regional three-dimensional seismic velocity model of the crust and uppermost mantle of northern California. *Journal of Geophysical Research: Solid Earth*, 114(B1), 2009.
- E. Tinti, E. Fukuyama, A. Piatanesi, and M. Cocco. A kinematic source-time function compatible with earthquake dynamics. *Bulletin of the Seismological Society of America*, 95(4):1211–1223, 2005.
- E. Tinti, L. Scognamiglio, A. Michelini, and M. Cocco. Slip heterogeneity and directivity of the ML 6.0, 2016, Amatrice earthquake estimated with rapid finite-fault inversion. *Geophysical Research Letters*, 43(20):10–745, 2016.
- M. Van Der Meijde, S. Van Der Lee, and D. Giardini. Crustal structure beneath broadband seismic stations in the Mediterranean region. *Geophysical Journal International*, 152(3):729–739, 2003.
- A. Venkataraman and H. Kanamori. Effect of directivity on estimates of radiated seismic energy. *Journal of Geophysical Research: Solid Earth*, 109(B4), 2004.
- M. Warner. Basalts, water, or shear zones in the lower continental crust? *Tectonophysics*, 173(1-4):163–174, 1990.
- K. H. Waters and K. H. Waters. *Reflection seismology: A tool for energy resource exploration*. Wiley New York, 1981.
- U. Wegler. Diffusion of seismic waves in layered media: boundary conditions and analytical solutions. *Geophysical Journal International*, 163(3):1123–1135, 2005.
- U. Wegler and B. G. Lühr. Scattering behaviour at Merapi volcano (Java) revealed from an active seismic experiment. *Geophysical Journal International*, 145(3):579–592, 2001.

- U. Wegler, M. Korn, and J. Przybilla. Modeling full seismogram envelopes using radiative transfer theory with Born scattering coefficients. *Pure and Applied Geophysics*, 163(2):503–531, 2006.
- R.-S. Wu. Multiple scattering and energy transfer of seismic waves—separation of scattering effect from intrinsic attenuation—I. Theoretical modelling. *Geophysical Journal International*, 82(1):57–80, 1985.
- R.-S. Wu and K. Aki. Introduction: Seismic wave scattering in three-dimensionally heterogeneous earth. In *Scattering and Attenuations of Seismic Waves, Part I*, pages 1–6. Springer, 1988a.
- R.-S. Wu and K. Aki. Multiple scattering and energy transfer of seismic waves—Separation of scattering effect from intrinsic attenuation II. Application of the theory to Hindu Kush region. In *Scattering and Attenuations of Seismic Waves, Part I*, pages 49–80. Springer, 1988b.
- J. Xie and B. Mitchell. A back-projection method for imaging large-scale lateral variations of Lg coda Q with application to continental Africa. *Geophysical Journal International*, 100(2):161–181, 1990.
- P. Xu and D. Zhao. Upper-mantle velocity structure beneath the North China Craton: implications for lithospheric thinning. *Geophysical Journal International*, 177(3):1279–1283, 2009.
- Z. Xu, L. Margerin, and T. D. Mikesell. Monte Carlo simulations of coupled body- and Rayleigh-wave multiple scattering in elastic media. *Geophysical Journal International*, 228(2):1213–1236, 2022.
- W. Yang and Y. Ben-Zion. Corner frequency ratios of P and S waves and strain drops of earthquakes recorded by a tight network around the Karadere segment of the North Anatolian Fault Zone: evidence for non-classical source processes. *Geophysical Supplements to the Monthly Notices of the Royal Astronomical Society*, 205(1):220–235, 2016.
- N. Yoshimitsu, T. Furumura, and T. Maeda. Geometric effect on a laboratory-scale wavefield inferred from a three-dimensional numerical simulation. *Journal of Applied Geophysics*, 132:184–192, 2016.

BIBLIOGRAPHY

- H. Yuan and B. Romanowicz. Lithospheric layering in the North American craton. *Nature*, 466(7310):1063–1068, 2010.
- B. Zhang, S. Ni, and Y. Chen. Seismic attenuation in the lower mantle beneath Northeast China constrained from short-period reflected core phases at short epicentral distances. *Earth and Planetary Physics*, 3(6):537–546, 2019.
- T.-R. Zhang and T. Lay. Why the Lg phase does not traverse oceanic crust. *Bulletin of the Seismological Society of America*, 85(6):1665–1678, 1995.
- W. Zhang and Y. Shen. Unsplit complex frequency-shifted PML implementation using auxiliary differential equations for seismic wave modeling. *Geophysics*, 75(4):T141–T154, 2010.